TECHNICAL SPECIFICATION

ISO/TS 20459

First edition
2023-04

Road vehicles — Injury risk functions for advanced pedestrian legform impactor (aPLI)

Véhicules routiers — Critères lésionnels et courbes de risques pour l'impacteur en forme de jambe de piéton (aPLI).

Reference number
ISO/TS 20459:2023(E)

ISO copyright office
CP 401 • Ch. de Blandonnet 8
CH-1214 Vernier, Geneva
Phone: +41 22 749 01 11
Email: copyright@iso.org
Website: www.iso.org

Published in Switzerland

Contents

Page

Foreword

ISO (the International Organization for Standardization) is a worldwide federation of national standards bodies (ISO member bodies). The work of preparing International Standards is normally carried out through ISO technical committees. Each member body interested in a subject for which a technical committee has been established has the right to be represented on that committee. International organizations, governmental and non-governmental, in liaison with ISO, also take part in the work. ISO collaborates closely with the International Electrotechnical Commission (IEC) on all matters of electrotechnical standardization.

The procedures used to develop this document and those intended for its further maintenance are described in the ISO/IEC Directives, Part 1. In particular, the different approval criteria needed for the different types of ISO documents should be noted. This document was drafted in accordance with the editorial rules of the ISO/IEC Directives, Part 2 (see www.iso.org/directives).

Attention is drawn to the possibility that some of the elements of this document may be the subject of patent rights. ISO shall not be held responsible for identifying any or all such patent rights. Details of any patent rights identified during the development of the document will be in the Introduction and/or on the ISO list of patent declarations received (see www.iso.org/patents).

Any trade name used in this document is information given for the convenience of users and does not constitute an endorsement.

For an explanation of the voluntary nature of standards, the meaning of ISO specific terms and expressions related to conformity assessment, as well as information about ISO's adherence to the World Trade Organization (WTO) principles in the Technical Barriers to Trade (TBT), see www.iso.org/iso/foreword.html.

This document was prepared by Technical Committee ISO/TC 22, *Road vehicles*, Subcommittee SC 36, *Safety and impact testing.*

Any feedback or questions on this document should be directed to the user's national standards body. A complete listing of these bodies can be found at www.iso.org/members.html.

Introduction

This document has been prepared on the basis of the existing injury probability functions (IPFs) to be used with the advanced pedestrian legform impactor (aPLI) standard build level B (SBL-B). The purpose of this document is to document the IPFs for the aPLI in a form suitable and intended for worldwide harmonized use.

In 2014, development of the aPLI hardware and associated IPFs started, with the aim of defining a globally accepted next-generation pedestrian legform impactor with enhanced biofidelity and injury assessment capability, along with its IPFs, suitable for harmonized use. Participating in the development were research institutes, dummy and instrumentation manufacturers, governments, and car manufacturers from around the world.

IPFs for the aPLI specified in this document predict injury probability to specific regions of the lower limb of a pedestrian that corresponds to maximum values of injury metrics obtained by the aPLI in a subsystem test, as described in References [1] and [2]. As the IPFs do not provide any threshold values, users will need to determine target injury probability, based on their specific needs, to define injury assessment reference values to be used for their test protocol.

It is also important to note that the subsystem test procedure (STP) for pedestrian protection may not be representative of pedestrian accidents for specific injury metrics, depending on their sensitivity to pedestrian impact conditions such as lower-limb posture and muscle tone. The IPFs for the aPLI have been validated against accident data and some ideas to compensate for the discrepancy against accident data are presented in Annex B.

Road vehicles — Injury risk functions for advanced pedestrian legform impactor (aPLI)

1 Scope

This document provides definitions, symbols and injury probability functions (IPFs) for the thigh, leg and knee intended to be used with the advanced pedestrian legform impactor (aPLI), a standardized pedestrian legform impactor with an upper mass for pedestrian subsystem testing of road vehicles. They are applicable to impact tests using the aPLI at 11,1 m/s involving:

— vehicles of category M1, except vehicles with a maximum mass above 2 500 kg and which are derived from N1 category vehicles and where the driver's position, the R-point, is either forward of the front axle or longitudinally rearwards of the front axle transverse centreline by a maximum of 1 100 mm;

— vehicles of category N1, except where the driver's position, the R-point, is either forward of the front axle or longitudinally rearwards of the front axle transverse centreline by maximum of 1 100 mm;

— impacts to the bumper test area defined by References [1] and [2];

— pedestrian subsystem tests involving use of a legform for the purpose of evaluating compliance with vehicle safety standards.

2 Normative references

There are no normative references in this document.

3 Terms and definitions

For the purposes of this document, the following terms and definitions apply.

ISO and IEC maintain terminology databases for use in standardization at the following addresses:

— ISO Online browsing platform: available at https://www.iso.org/obp

— IEC Electropedia: available at https://www.electropedia.org/

3.1
adult
person who is sixteen years old or older

3.2
advanced pedestrian legform impactor
aPLI
modified pedestrian legform impactor which incorporates a mass representing the inertial effect of the upper part of a pedestrian body to enhance biofidelity and *injury assessment capability* (3.10) of conventional pedestrian legforms

3.3
biofidelity
aspect of the *advanced pedestrian legform impactor (aPLI)* (3.2) capability to represent the impact response of human subjects

3.4
BLE height
bonnet leading edge height
height of the geometric trace of the upper most points of contact between a straight edge and the front-end of the car

3.5
bumper test area
test area of the legform to bumper impact test

3.6
bumper system
component installed at the hip joint inside the upper mass composed of the bumper, the bumper mount and the compression surface, designed to apply a force on the upper part of the femur in adduction to enhance *injury assessment capability* (3.10) of the *advanced pedestrian legform impactor (aPLI)* (3.2)

3.7
EE method
energy-equivalent method
method of developing *injury probability functions (IPFs)* (3.11) for the *advanced pedestrian legform impactor (aPLI)* (3.2) by transferring human injury values to those of an aPLI using the absorbed energy

3.8
high-bumper car
car with a *lower bumper reference line height* (3.14) of 425 mm or more

3.9
hip joint
uniaxial joint that allows abduction and adduction and connects the upper mass with the lower limb

3.10
injury assessment capability
aspect of the *advanced pedestrian legform impactor (aPLI)* (3.2) capability to produce peak injury values that correlate with those obtained from human body model impact simulations

3.11
IPF
injury probability function
function which defines the relationship between a peak value of an injury metric and probability of injury for a specific load case

3.12
ISO metric
objective rating metric used in this document to verify time histories of sensor output against experimentally or computationally produced target time histories as detailed in ISO/TS 18571:2014

3.13
low-bumper car
car with a *lower bumper reference line height* (3.14) less than 425 mm

3.14
LBRL height
lower bumper reference line height
height of the geometric trace of the lowermost points of contact between a straight edge and the bumper, measured from the ground

3.15
low-pass filter
filter which permits only low-frequency (100 Hz or less) oscillations

3.16
paired test method
method of developing *injury probability functions (IPFs)* (3.11) by correlating human injury occurrence in a specific impact configuration with the injury value measured by an ATD subjected to the same impact as detailed in ISO/TR 12350:2013

3.17
subsystem test
test to evaluate safety performance of cars where subsystem impactors representing individual body regions of a pedestrian are propelled into a front end of a stationary car, in impact conditions representing specific load cases in car-pedestrian accidents

3.18
transfer function
TF
linear regression function between human injury values predicted by human body models and *advanced pedestrian legform impactor (aPLI)* (3.2) injury values

3.19
TF method
transfer-function method
method of developing *injury probability functions (IPFs)* (3.11) for the *advanced pedestrian legform impactor (aPLI)* (3.2) by converting human IPFs to those of the aPLI using corresponding *transfer functions* (3.18)

4 Symbols and abbreviated terms

4.1 Symbols

See Table 1.

Table 1 — Symbols and their meanings

Symbol	Meaning
C_{Scale}	Parameter determined for the Weibull distribution for human IPFs
C_{Shape}	Parameter determined for the Weibull distribution for human IPFs
C_{Slope}	Slope of the transfer function
C_{μ}	Parameter determined for the Log-Normal distribution for human IPFs
C_{σ}	Parameter determined for the Log-Normal distribution for human IPFs
C_{TA1}	Correction factor determined to adjust to the real-world accident data
C_{TA2}	Correction factor determined to adjust to the real-world accident data
F	IPF for human
G	Transfer function
I_{human}	Injury metric for human
I_{aPLI}	Injury metric for the aPLI
P	Injury probability of human
P_{adj}	Adjusted injury probability for the MCL
x_{aPLI}	Value of the injury metric for the aPLI
x_{human}	Value of the injury metric for human

4.2 Abbreviated terms

See Table 2.

Table 2 — Abbreviated terms and their meanings

Abbreviation	Meaning
ACL	Anterior Cruciate Ligament
aPLI	advanced Pedestrian Legform Impactor
ATD	Anthropometric Test Device
BLE	Bonnet Leading Edge
BM	Bending Moment
BP	Bumper
EE	Energy Equivalent
EEVC	European Enhanced Vehicle-safety Committee
FE	Finite Element
HBM	Human Body Model
IPF	Injury Probability Function
LBRL	Lower Bumper Reference Line
MCL	Medial Collateral Ligament
PCL	Posterior Cruciate Ligament
PMHS	Post Mortem Human Subjects
RCM	Real Car Model
SCM	Simplified Car Model
SP	Spoiler
STP	Subsystem Test Procedure
TF	Transfer Function
TG	Task Group

5 IPFs for the aPLI

5.1 General

The IPFs specified in this document are to be used with the aPLI for the thigh, leg and knee to predict the probability of injuries to pedestrians when involved in real-world car-pedestrian accidents. The IPFs provide a statistically derived relationship between the maximum values of injury metrics obtained from a test conducted using the aPLI by following the subsystem test procedure (STP), and the probability of injury to a corresponding body region of a pedestrian when subjected to load cases representative of the majority of real-world accidents.

The specific load case represented by the subsystem legform test is described below:

— pedestrian size and weight: 175,1 cm and 76,7 kg representing a 50th percentile adult male (Reference [3]);

— impact speed: 11,1 m/s;

— impact direction: lateral-to-medial direction to a pedestrian lower limb;

— lower-limb posture: upright (vertical to the ground) with the knee fully extended;

— impact height: sole of the foot positioned 25 mm above the ground to represent a shoe sole height.

First, human IPFs were determined using human biomechanical data available from the literature. Data obtained by the experiments conducted under the loading conditions equivalent to those specified in the STP were referred to. The statistical method used to derive human IPFs follows that recommended by ISO/TS 18506 with the covariates of pedestrian size, weight and age. The pedestrian size and weight were determined from those specified in STP. The age was set at 60 years old that corresponds to the average age of the subjects of the biomechanical data as this choice was found to provide the most reasonable set of assumptions when the IPFs were fitted to the accident data. The recommended method estimates parameters of any one of the Weibull, Log-Normal or Log-Logistic distribution (choose the one that best fits to data) with survival analysis method. In this document, one of the three distributions (Weibull distribution, Log-Normal distribution or Log-Logistic distribution) is used to define human IPFs for each of the injury metrics. The formulae of the aPLI IPFs for these distributions are presented below.

The injury probability when the Weibull distribution is applied following Formula (1):

$$P = 1 - \exp\left\{-\left(\frac{C_{\text{Slope}} \times x_{\text{aPLI}}}{C_{\text{Scale}}}\right)^{C_{\text{Shape}}}\right\} \tag{1}$$

where

P is the injury probability of human;

C_{Scale} is the parameter determined for the Weibull distribution for human IPFs;

C_{Shape} is the parameter determined for the Weibull distribution for human IPFs;

C_{Slope} is the slope of the transfer function (TF);

x_{aPLI} is the value of the injury metric for the aPLI.

The injury probability when the Log-Normal distribution is applied following Formula (2):

$$P = \frac{1}{C_\sigma \sqrt{2\pi}} \int_0^{C_{\text{Slope}} \times x_{\text{aPLI}}} \frac{1}{t} \exp\left\{\frac{-(\ln t - C_\mu)^2}{2{C_\sigma}^2}\right\} dt \tag{2}$$

where

P is the injury probability of human;

C_μ is the parameter determined for the Log-Normal distribution for human IPFs;

C_σ is the parameter determined for the Log-Normal distribution for human IPFs;

C_{Slope} is the slope of the TF;

x_{aPLI} is the value of the injury metric for the aPLI.

The injury probability when the Log-Logistic distribution is applied following Formula (3):

$$P = \frac{1}{1 + \left(\frac{C_{\text{Slope}} \times x_{\text{aPLI}}}{\exp(C_{\text{Scale}})}\right)^{\frac{-1}{C_{\text{Shape}}}}} \tag{3}$$

where

P is the injury probability of human;

C_{Scale} is the parameter determined for the Log-Logistic distribution for human IPFs;

C_{Shape} is the parameter determined for the Log-Logistic distribution for human IPFs;

C_{Slope} is the slope of the TF;

x_{aPLI} is the value of the injury metric for the aPLI.

For each of the thigh, leg and knee, IPFs for a human body are then transferred to those of the aPLI using a TF, which is a linear function between the maximum values of a human and aPLI injury metrics. Due to the lack of biomechanical data, the TFs were determined from the results of computational impact simulations using FE human body models (HBMs) and aPLI FE models in loading conditions specified in the STP. Details of the human IPFs from which IPFs for the aPLI are derived can be found in A.2.3. For the determination of TFs, see A.2.4 for more details.

As the IPFs converted from human IPFs using TFs are for the specific load case defined in the STP, the number of injuries calculated from each of the injury probabilities predicted by the IPFs were compared with that of real-world accidents. The IPFs for the knee and the leg were compensated for the real-world observations for the injury metrics showing a significant inconsistency with accident data. Details of the compensation to real-world accidents can be found in Annex B.

Supplemental information related to the TFs and IPFs for human is provided in Annex C and Annex D, respectively.

5.2 Thigh

The IPF for the thigh defines probability of femur shaft fracture to a pedestrian subjected to the load cases representative of the majority of real-world accidents as a function of maximum value of the femur bending moment measured by the aPLI.

Figure 1 presents the IPF for the thigh. The injury probability function is shown in a solid line, with the 95 % confidence interval shown in dotted lines. The horizontal axis represents the maximum value of the femur bending moment measured by the aPLI, and the vertical axis represents the probability of injury.

The IPF for the thigh is given by Formula (4):

$$P = 1 - \exp\left\{-\left(\frac{C_{Slope} \times x_{aPLI}}{C_{Scale}}\right)^{C_{Shape}}\right\} \quad (4)$$

where

P is the injury probability for the femur shaft of human;

C_{Scale} is the parameter determined for the Weibull distribution for the human IPF for the femur shaft as described in A.2.3.4.1;

C_{Shape} is the parameter determined for the Weibull distribution for the human IPF for the femur shaft as described in A.2.3.4.1;

C_{Slope} is the slope of the TF for the thigh as described in A.2.4.4.1;

x_{aPLI} is the femur BM measured by the aPLI in Nm.

The parameters needed to define the IPF (C_{Scale}, C_{Shape} and C_{Slope}) for the function are described in Table 3.

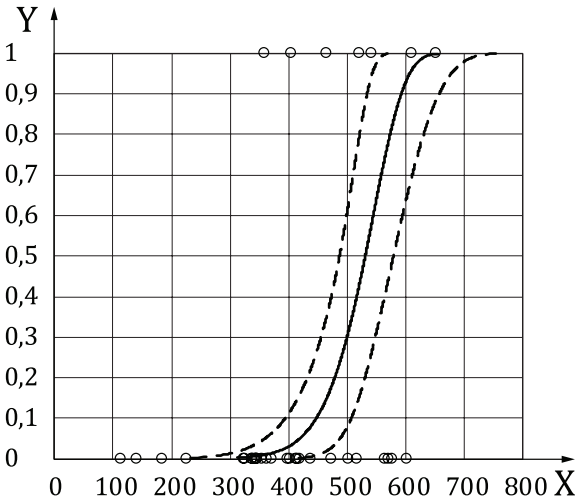

Key

X	aPLI femur BM [Nm]
Y	probability of femur shaft fracture
_____	aPLI IPF for femur shaft
= = =	95 % confidence interval
○	observed data

Figure 1 — IPF for the femur shaft

Table 3 — Parameters of IPF for the femur shaft

C_{Scale}	C_{Shape}	C_{Slope}
571	11,0	1,04

5.3 Leg

The IPF for the leg defines probability of tibia shaft fracture to a pedestrian subjected to the specific load cases representative of the majority of real-world accidents as a function of maximum value of the tibia bending moment measured by the aPLI.

Figure 2 presents the IPF for the leg. The injury probability function is shown in a solid line, with the 95 % confidence interval shown in dotted lines. The horizontal axis represents the maximum value of the tibia bending moment measured by the aPLI, and the vertical axis represents the probability of injury.

The IPF for the leg is given by the Formula (5):

$$P = 1 - \exp\left\{-\left(\frac{C_{Slope} \times x_{aPLI}}{C_{Scale}}\right)^{C_{Shape}}\right\} \quad (5)$$

where

P is the injury probability for the tibia shaft of human;

C_{Scale} is the parameter determined for the Weibull distribution for the human IPF for the tibia shaft as described in B.3.3;

C_{Shape} is the parameter determined for the Weibull distribution for the human IPF for the tibia shaft as described in B.3.3;

C_{Slope} is the slope of the TF for the leg as described in A.2.4.4.2;

x_{aPLI} is the tibia BM measured by the aPLI in Nm.

The parameters needed to define the IPF (C_{Scale}, C_{Shape} and C_{Slope}) for the function are described in Table 4.

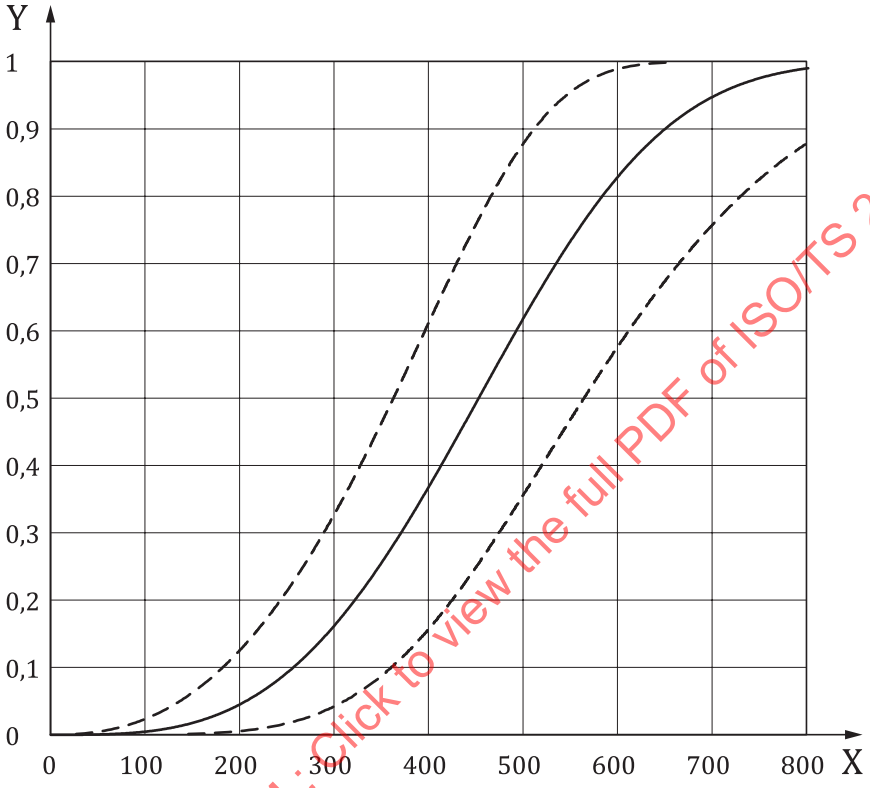

Key

X aPLI tibia BM [Nm]

Y probability of tibia shaft fracture

_____ aPLI IPF for tibia shaft

– – – 95 % confidence interval

Figure 2 — IPF for the tibia shaft

Table 4 — Parameters of IPF for the tibia shaft

C_{Scale}	C_{Shape}	C_{Slope}
446	3,32	0,881

5.4 Knee

The IPF for the knee defines probability of complete failure of the MCL to a pedestrian subjected to the specific load cases representative of the majority of real-world accidents as a function of maximum value of MCL elongation measured by the aPLI.

Figure 3 presents the IPF for the knee. The injury probability function is shown in a solid line, with the 95 % confidence interval shown in dotted lines. The horizontal axis represents the maximum value of the MCL elongation measured by the aPLI, and the vertical axis represents the probability of injury.

The IPF for the knee is given by Formula (6):

$$P = \frac{1}{C_\sigma \sqrt{2\pi}} \int_0^{C_{Slope} \times x_{aPLI} \times C_{TA1} \times C_{TA2}} \frac{1}{t} \exp\left\{ \frac{-\left(\ln t - C_\mu\right)^2}{2{C_\sigma}^2} \right\} dt \quad (6)$$

where

P is the injury probability for the MCL of human;

C_μ is the parameter determined for the Log-Normal distribution for human IPFs for the MCL as described in A.2.3.4.3;

C_σ is the parameter determined for the Log-Normal distribution for human IPFs for the MCL as described in A.2.3.4.3;

C_{Slope} is the slope of the TF for the knee as described in A.2.4.4.3;

C_{TA1} is the correction factor for lower-limb posture and impact angle determined to adjust to the real-world accident data as described in B.3.2.2.4;

C_{TA2} is the correction factor for muscle tone determined to adjust to the real-world accident data as described in B.3.2.3;

x_{aPLI} is the MCL elongation measured by the aPLI in mm.

The parameters needed to define the IPF (C_μ, C_σ, C_{Slope}, C_{TA1} and C_{TA2}) for the function are described in Table 5.

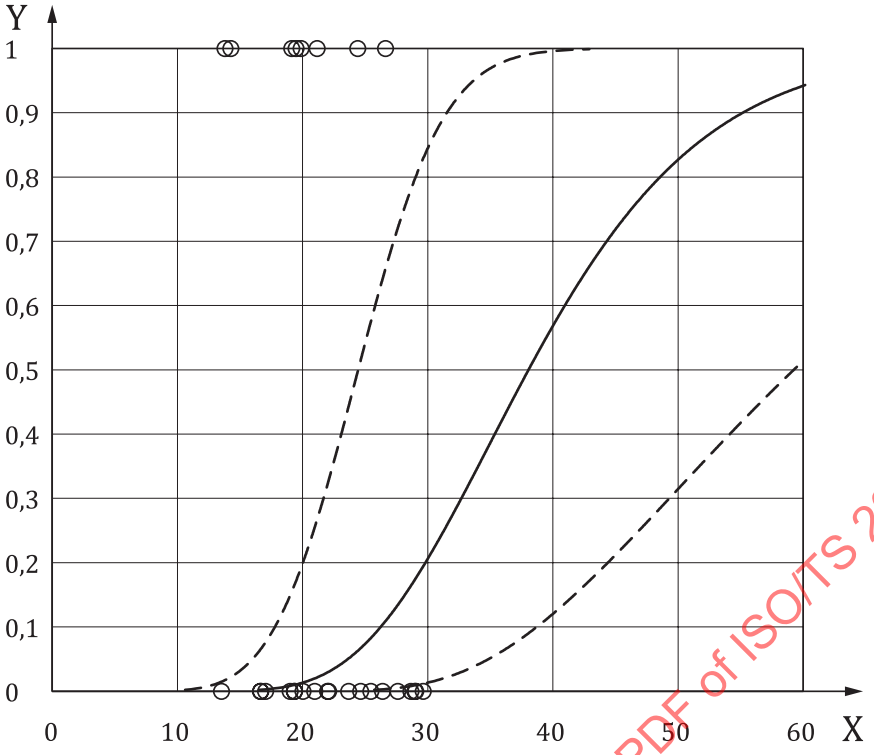

Key

X	aPLI MCL elongation [mm]
Y	probability of MCL complete rupture
_____	aPLI IPF for MCL complete rupture
⚌⚌⚌	95 % confidence interval
○	observed data

Figure 3 — IPF for the MCL complete rupture

Table 5 — Parameters of IPF for the MCL complete rupture

C_{μ}	C_{σ}	C_{Slope}	C_{TA1}	C_{TA2}
3,34	0,291	1,14	0,72	0,90

Annex A
(informative)

Rationale regarding background and methodology to develop IPFs for the aPLI

A.1 Historical background

A.1.1 General

Although lower extremity injuries are not life-threatening, they are frequent and potentially disabling, resulting in a substantial cost to the victims and society. The importance of preventing this type of injuries is illustrated by the United Nation (UN) regulations that aim to mitigate lower extremity injuries to pedestrians hit by the front-end of cars (See References [1] and [2]).

The UN regulations initially implemented the EEVC pedestrian legform impactor that simply consists of rigid long bones and a deformable knee joint. In order to improve injury assessment capability, a new impactor called the Flexible Pedestrian Legform Impactor (FlexPLI) has been developed and implemented in the phase-2 of Reference [1].

Despite a number of improvements of its capability relative to the EEVC impactor, the FlexPLI still lacks representation of the influence of the upper part of the body. To address technical issues with the FlexPLI, including but not limited to the lack of upper body representation, the aPLI with the upper mass attached to the top of the conventional pedestrian legform to compensate for the lack of the upper body has been developed. In November 2014, two ISO projects were initiated to develop Technical Specification (TSs) for "Road vehicles - Modified pedestrian legform impactor for tests of high bumper vehicles" and "Road vehicles - Injury criteria and risk curves for a modified pedestrian legform impactor for use with high bumper vehicles", and the aPLI task group (TG) was established by active participants from research institutes, dummy and instruments manufacturers, governments and car manufacturers. The aPLI TG has conducted extensive CAE studies to identify optimized specifications of the aPLI by utilizing HBMs, SCMs and aPLI prototype models. Based on the specifications identified, a physical version of aPLI SBL-A was fabricated and subjected to international round robin testing.

The aPLI TG also dedicated to their effort to discuss a methodology to develop IPFs. During the discussion, two different methods were proposed and it was difficult to choose one of the two proposed methods because both have pros and cons. A new idea taken to facilitate the discussion was to develop 'virtual IPFs' by using parametric human body models (HBMs) with the variability in the material property of a human body incorporated. The results of this analysis along with some other consideration resulted in a decision of applying a TF to convert IPFs for human to those for the aPLI.

Due to the lack of sufficient biomechanical data, it was necessary to determine TFs based on the results of computer simulations using HBMs to take various load cases into consideration. Multiple HBMs with extensive validation were used to avoid potential bias in case one single HBM is employed. The specifications of the latest version of the aPLI hardware with the bumper system installed at the hip joint as defined in ISO/TS 20458 were represented by FE models and used in the analyses. Real car models (RCMs) were also used to accurately represent geometric and stiffness characteristics of car front-end structures. The use of multiple different HBMs, RCMs and impact locations allowed determination of robust IPFs.

In the course of the discussion at the aPLI TG, a question was raised as to real-world relevance of the IPFs determined in this international effort. The most important decision made by the aPLI TG was that IPFs shall predict the probability of injury to a pedestrian involved in a real car accident, not necessarily to a pedestrian hit by a car in a load case specified in the STP. This approach would require adjustment of IPFs to match field observations, if the load case specified by the STP does not represent real-world

accidents. Among the three body regions (thigh, knee and leg) for which injury values are measured by the aPLI, a preliminary study done by the aPLI TG revealed that a significant discrepancy in the prediction of the probability of injury is seen specifically with the MCL elongation, due to the upright lower limb position and fully extended knee specified in the STP, and the lack of consideration of the influence of muscle tone. For this reason, the aPLI TG decided to adjust aPLI IPFs to match real-world observations in such a way that injury metrics obtained from an aPLI car test are converted to the probability of injury in real-world accidents.

IPFs for human that represent the load case specified in the STP were initially developed because the biomechanical data available in the literature are from experimental studies that used boundary conditions representing this load case. By applying the TFs, the IPFs for humans were transformed to the IPFs for the aPLI that predict the probability of injury in the load case specified in the STP. The number of injuries estimated from the probability of injury predicted by these IPFs was compared to that of the real-world accidents for each of the injury metrics for the aPLI. Whenever a significant inconsistency with the field observation was identified, factors responsible for the discrepancy were investigated using literature review, HBMs and multiple car models. Based on the results of the investigation, the IPFs for the knee and leg were adjusted to the real-world accident data as described in Annex B. The adjusted IPFs were further modified to better match the field observations as needed.

A.1.2 Need for standardized IPFs for the aPLI

Due to the lack of the upper body, the legform test in the pedestrian STP allows assessment of knee and leg regions only, necessitating a different test procedure for the thigh region with a different impactor and a test protocol. The lack of biofidelity of the upper legform requires a modified legform with upper body representation. In addition, a large approach angle of a high-bumper car results in significantly different kinematics of a legform, leading to a need for a different test procedure specifically defined for such cars and inconsistency of the bumper test.

For these reasons, new car assessment programs have been interested in introducing a modified legform test capable of replacing the upper legform tests and enhancing injury assessment. In order to avoid unreasonable increase of the cost to car manufacturer, and therefore to customers, of developing different car structures and/or protection systems to comply with different requirements, a globally accepted and harmonized test tool is crucial for future upgrade of a test procedure for consumer information and regulatory testing. Accurate prediction of injury probability in real-world accidents from the test results using such an advanced test tool is also vital to take the best advantage of the tool.

A.1.3 Benefits and economic impact of standardized IPFs for the aPLI

Robustness of IPFs is crucial to determine injury assessment reference values (IARVs) suitable for globally harmonized use. When investigating correlation between human and aPLI impact responses to develop IPFs based on biomechanical data, this requires consideration of various shapes and stiffness distributions of front ends of cars, along with multiple different HBMs that have been well validated against biomechanical data. An international effort provided by the experts of the aPLI TG has allowed incorporation of various impact configurations from a variety of combinations of cars in different markets and HBMs.

With regard to the benefits, globally harmonized and scientifically valid IPFs for the aPLI are essential to determine reasonable IARVs for future regulations and/or new car assessment programs. It is also crucial that the IPFs predict the probability of injury in a load case representative of real-world accidents, not necessarily the load case specified in a test procedure in case it is not representative. Determination of reasonable IARVs would ensure effectiveness of pedestrian safety measures of cars in real-world accidents, and eliminate potentially wasteful and misleading efforts of car manufacturers needed to develop cars to comply with the requirements imposed by unreasonable IARVs. This also reduces costs to consumers, along with the reduction of social costs due to injuries to pedestrian lower limbs.

A.1.4 Survey and general differences from previous IPFs

The IARVs for the FlexPLI have been determined for References [1] and [2] by the informal group on UN GTR No.9 Phase-2 under the UN working party on passive safety (GRSP). Due to the lack of globally accepted IPFs for the FlexPLI, the discussion to determine IARVs has been a big challenge, involving proposals from different rationale and concepts. In such a situation, both technical and political discussions were mixed up, making it difficult to clarify benefits in a consistent manner. This has led to a strong need for a globally accepted and scientifically valid IPFs for the aPLI, which is anticipated to be used in future regulatory and consumer information testing.

In the course of the discussion on the FlexPLI IARVs, IPFs for the FlexPLI have been developed using biomechanical data[6]. Although a similar methodology to that used to develop IPFs for the aPLI was used, there are some limitations due to the statistical method used and limited robustness of the TFs. A combination of geometric scaling of injury values and a univariate survival model was applied for the FlexPLI, while a multivariate survival model used for the aPLI defined injury probability as a function of the height, the weight and the age of a pedestrian to enhance accuracy of prediction models. When developing TFs for the FlexPLI, impact simulations were conducted using one single HBM and simplified car models (SCMs) representing geometric and stiffness characteristics of old sedans at one single impact location. The robustness of TFs for the aPLI has been significantly enhanced by using multiple HBMs and RCMs representing various types of cars in a global fleet along with impact simulations at multiple impact locations. In addition, the relevance of the IPFs for FlexPLI were not validated against accident data, while the IPFs for the aPLI were adjusted to real-world observations whenever needed. The enhancement in the statistical method and the robustness of TFs, along with the adjustment of the IPFs to real-world accident data, would lead to more accurate prediction of the probability of injury to a pedestrian lower limb when involved in a car-pedestrian accident, and consequently contribute to further improvement in pedestrian safety performance of cars in a global market.

A.1.5 Summary of development process of IPFs for the aPLI

The following summarizes some of the milestones in the aPLI project, in order to describe the international development and consensus process.

— June 2015: The aPLI TG was established by ISO TC 22/SC 36/WG 5 and WG 6.

— November 2017: At the 6th aPLI TG meeting, it was recognized by aPLI TG members that the paired test method (ISO/TR 12350:2013)[4] is not applicable to develop IPFs for the aPLI because of the lack of sufficient biomechanical data, and two alternatives, the TF method and the EE method as detailed in Annex A.2.2.2.2 and Annex A.2.2.2.3, respectively, were proposed by some of aPLI TG members.

— May 2018: The idea of a virtual paired test was proposed by some of aPLI TG members at the 7th aPLI TG meeting to evaluate the two methods to develop IPFs for the aPLI.

— June 2019: The aPLI TG decided at its 9th meeting in London to use the TF method based on the results of the virtual paired test and the comparison of the number of biomechanical data available for each of the two methods.

— June to December 2020: Due to the pandemic situation of COVID-19, aPLI TG activity was put on hold, and official discussions on the development of IPFs for human and TFs have been suspended.

— February 2021: The aPLI TG activity was restarted and it was endorsed to adjust the IPFs to real-world accident data. A draft version of ISO/TS 20459 was submitted to the aPLI TG for review.

— March to August 2021: Due to continued pandemic of COVID-19, aPLI TG activity was put on hold again.

— August 2021: The aPLI TG activity was officially restarted.

— March 2022: A modified draft version of ISO/TS 20459 incorporating the IPFs for the aPLI was accepted by the aPLI TG and submitted to ISO TC22/SC36/WG6 for their review.

— May 2022: The draft version of ISO/TS 20459 was further modified based on the comments from WG6 and was approved by WG6. The document was immediately subjected to a ballot of ISO TC22/SC36.

— July 2022: The proposed ISO/TS 20459 was approved by ISO TC22/SC36 with some requests for modification.

Organizationally, at every stage, the aPLI TG attempted to include all interested parties involved in the pedestrian safety field worldwide. In particular, 28 aPLI TG web meetings were held in between face-to-face meetings to facilitate discussions and consensus development by all participants. All the development activities were conducted at the expense of participating parties. Collaborative CAE studies to develop TFs were conducted by contributors from Germany, France, the United States and Japan.

A.2 Methodology to develop IPFs for the aPLI

A.2.1 General

Any assessment of car safety performance shall provide information relevant to the probability of injury sustained by the victims involved in real-world car accidents, not in laboratory car crash tests. In general, testing and assessment protocols are designed to provide such information. In the case of the assessment of safety performance against pedestrian lower limb injury, the aPLI TG recognized a large discrepancy between the two load cases, specifically with the MCL elongation. Once IPFs for the aPLI consistent with the STP are developed, the relevance of the IPFs against accident data shall be evaluated. The IPFs shall be adjusted to represent injury probability in real-world accidents when inconsistency is found to be significant.

IPFs for the aPLI were developed by the following steps. First, human biomechanical data were collected to develop IPFs for the aPLI. The results of the experiments performed under the conditions similar to the load case specified in the STP were used. The conditions included regions of the lower limb, specific injuries reproduced, relevant injury metrics to predict such injuries, and specific load cases such as the loading rate, loading direction and lower limb posture. Second, a methodology to develop IPFs for the aPLI in a load case specified in the STP was determined. This step was one of the most challenging one among all the steps employed. Due to the lack of sufficient biomechanical data available, it was impossible to use the method defined by ISO for the WorldSID dummy (paired test method described in ISO/TR 12350), and an alternative method needed to be defined. As a result of intensive discussion by aPLI TG members, it was eventually decided to use the TF method. Third, IPFs for the aPLI were developed by using the TF method. In the TF method, IPFs for human are initially developed, and then converted to those of the aPLI in the load case specified by the STP by applying TFs obtained from a regression analysis of maximum values of injury metrics between aPLI and human. Finally, the relevance of the IPFs was assessed against accident data and the IPFs were adjusted to better represent real-world accident data whenever needed.

More details with regard to the methodology to develop IPFs for the aPLI can be found in the following sections.

A.2.2 Determination of methodology to develop IPFs for the aPLI in a load case specified in the STP as functions of aPLI injury metrics

A.2.2.1 General

The paired test method used by ISO to derive IPFs for WorldSID (ISO/TR 12350) relates injury occurrence to human bodies to injury values from the dummy by performing paired (human and dummy) tests in the same impact configuration. In case of a pedestrian, however, full-scale impact test data using human subjects are scarce, and therefore an alternative methodology to develop IPFs for the aPLI needed to be determined. This resulted in proposals of two alternative methods at the aPLI TG (TF method and EE method), and an extensive study was conducted to make a final decision. As both methods involve pros and cons, a new idea of investigating virtual IPFs was proposed that virtually

generates biomechanical data using parametric HBMs that incorporate variability of material property of human tissues to allow comparison of IPFs from the two proposed methods against those determined by the paired test method. The results of this investigation along with the difference of the number of data that can be used in each of the two proposed methods resulted in the choice of the TF method at the aPLI TG.

A.2.2.2 Virtual IPF

A.2.2.2.1 Parametric HBM

Due to the lack of a sufficient number of full-scale pedestrian impact test data, full-scale impact test data using human subjects were virtually generated by incorporating variability of the material property of human tissues in a validated HBM (References [7], [8] and [9]) to create parametric HBMs with different material property. Since the material property of human tissue is generally characterized by a constitutive equation that describes the relationship between the stress and the strain, three levels (mean, upper and lower limits) were set for each, resulting in a total of nine parametric HBMs. Assuming that the major contributors to the lower limb injury metrics (femur and tibia bending moment (BM), MCL elongation) are the material property of the cortical bones of the femur, tibia and fibula, along with that of the four major knee ligaments (anterior cruciate ligament (ACL), posterior cruciate ligament (PCL), lateral collateral ligament (LCL) and MCL) and the knee joint capsule, the same material property was used for the flesh, skin and other bones and ligaments for all of the nine HBMs.

The nine parametric HBMs were determined by means of the following procedure. Initially, biomechanical data were investigated for each of the varied material parameters. Assuming that the material property is the same between the tibia and the fibula, and among the four knee ligaments, the following values were obtained from the literature for the cortical bones of the femur and the tibia as well as the four knee ligaments:

a) Young's modulus, ultimate stress and ultimate strain:
   - femur: mean and 90 % confidence interval[10];
   - tibia: mean and 90 % confidence interval[10];
   - knee ligament: mean[10];

b) Ratio of yield stress to ultimate stress:
   - tibia[11];
   - knee ligament: mean[10].

Using the values of the material parameters obtained above, nine stress-strain curves were determined by means of the following steps. First, for all the material parameters of the femur, the tibia and the fibula, except the yield stress, the mean and the upper and lower limits were determined from the mean and 90 % confidence interval obtained from the literature listed above. As a 90 % confidence interval was not available from the literature for the knee ligaments, a 90 % confidence interval normalized by mean obtained for the femur was applied to each of the Young's modulus, ultimate stress and ultimate strain to estimate the 90 % confidence interval of the corresponding material parameter. Second, nine failure points were determined from the mean and the upper and lower limbs of the ultimate stress and the ultimate strain. Since the data for the ultimate stress and the ultimate strain show bell-shaped distribution, it was assumed that the combinations of the maximum and the minimum values of the ultimate stress/strain are unrealistic. By eliminating these extreme combinations, the nine failure points were distributed on a diamond shape and its centroid, with the mean and the upper and lower limits of the ultimate stress/strain represented by its diagonal lines as shown in Figures A.1 through A.3. Third, the nine failure points were assigned to each of the mean and the upper and lower limits of the Young's modulus determined above. Reference [11] shows that a large Young's modulus for the tibia is associated with a large ultimate stress and a small ultimate strain due to trade-off between brittleness and ductility. This nature was assumed to apply to other tissues as well. For this reason, the nine failure points were grouped into three, each containing three points, in such a way that the

corresponding points from the three groups are aligned in a downward slope (groups of black, white and grey squares: see Figures A.1 through A.3). Each of the three groups of the three failure points was assigned to each of the three values of the Young's modulus by following the trend described above. Finally, the slope of the plastic region in the stress-strain curve was determined for each of the nine failure points. References [11] and [10] show that the ratio of the yield stress to the ultimate stress is constant for the cortical bone of the tibia as well as the knee ligaments (tibia: 0,82, knee ligaments: 0,82). The same ratio as that of the tibia was applied to the femur due to the lack of available information. In Reference [12] it is found that the stiffness of the toe region, up to 5 % strain, of the stress-strain curve of the knee ligaments is approximately half of that of the subsequent elastic region. This finding was reflected in the stress-strain curves determined for the knee ligaments (see Figure A.3).

The thigh, the leg and the knee of the nine parametric HBMs sufficiently represented the variability of the PMHS responses in a 3-point bending test of the thigh [13][14] and the leg [13][15][14], and 4-point bending test for the knee[16], as shown in Figure A.4 through Figure A.6, respectively. Biomechanical data needed for the TF method, EE method and paired test method were virtually generated using these HBMs, and each of the three methods was applied to calculate IPFs for the thigh, leg and knee.

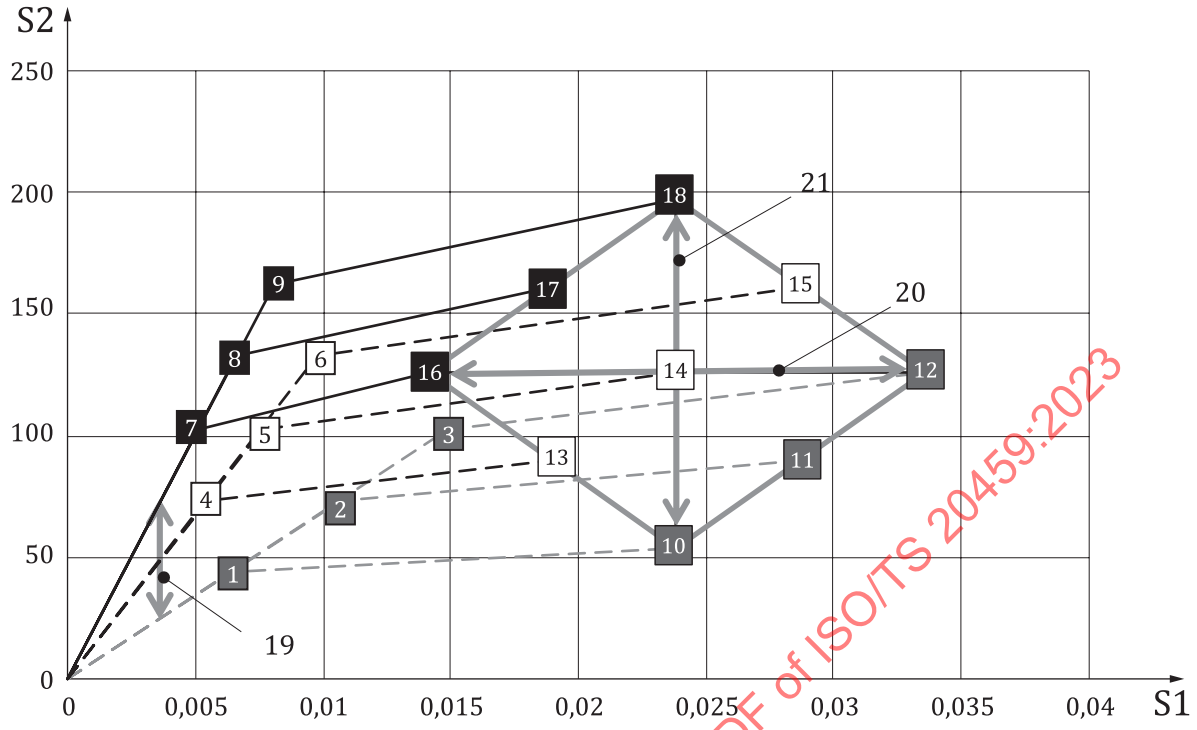

Key

1 yield stress/strain for HBM1
2 yield stress/strain for HBM2
3 yield stress/strain for HBM3
4 yield stress/strain for HBM4
5 yield stress/strain for HBM5
6 yield stress/strain for HBM6
7 yield stress/strain for HBM7
8 yield stress/strain for HBM8
9 yield stress/strain for HBM9
10 ultimate stress/strain for HBM1
11 ultimate stress/strain for HBM2
12 ultimate stress/strain for HBM3
13 ultimate stress/strain for HBM4
14 ultimate stress/strain for HBM5
15 ultimate stress/strain for HBM6
16 ultimate stress/strain for HBM7
17 ultimate stress/strain for HBM8
18 ultimate stress/strain for HBM9
19 90 % confidence interval (young's modulus)
20 90 % confidence interval (ultimate strain)
21 90 % confidence interval (ultimate stress)
S1 strain
S2 stress [MPa]

Figure A.1 — Stress-strain curves of the cortical bone of the femur for the nine parametric HBMs

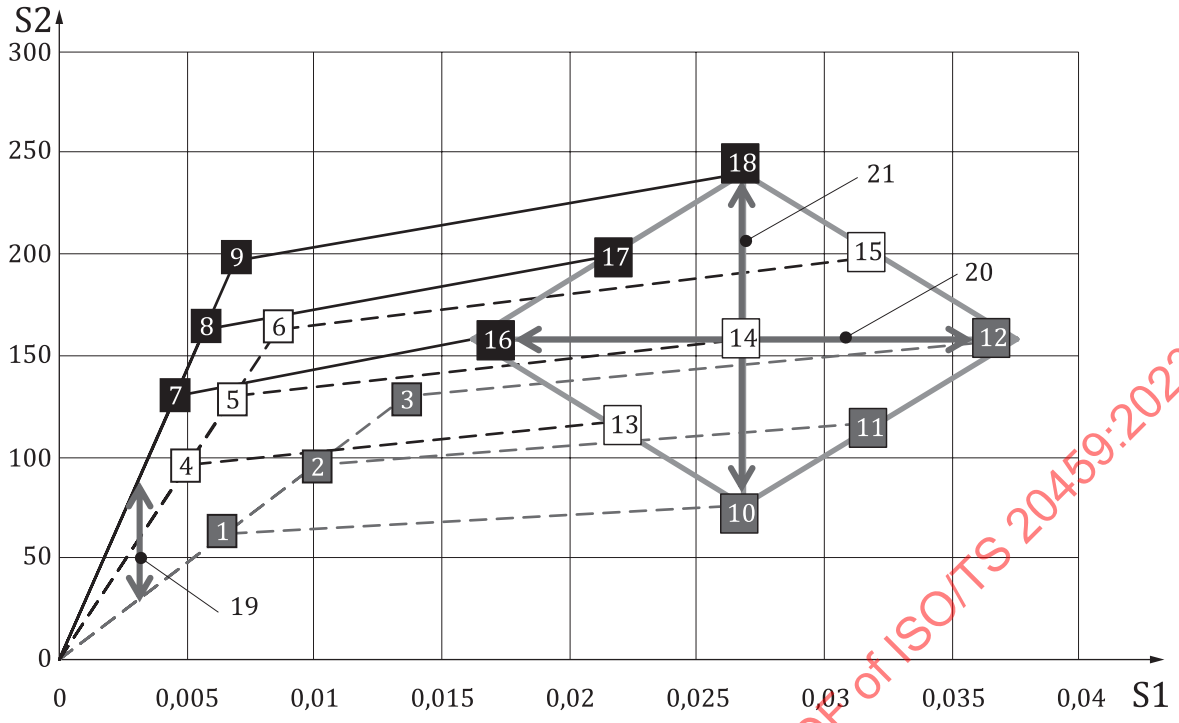

Key

1 yield stress/strain for HBM1
2 yield stress/strain for HBM2
3 yield stress/strain for HBM3
4 yield stress/strain for HBM4
5 yield stress/strain for HBM5
6 yield stress/strain for HBM6
7 yield stress/strain for HBM7
8 yield stress/strain for HBM8
9 yield stress/strain for HBM9
10 ultimate stress/strain for HBM1
11 ultimate stress/strain for HBM2
12 ultimate stress/strain for HBM3
13 ultimate stress/strain for HBM4
14 ultimate stress/strain for HBM5
15 ultimate stress/strain for HBM6
16 ultimate stress/strain for HBM7
17 ultimate stress/strain for HBM8
18 ultimate stress/strain for HBM9
19 90 % confidence interval (young's modulus)
20 90 % confidence interval (ultimate strain)
21 90 % confidence interval (ultimate stress)
S1 strain
S2 stress [MPa]

Figure A.2 — Stress-strain curves of the cortical bone of the tibia for the nine parametric HBMs

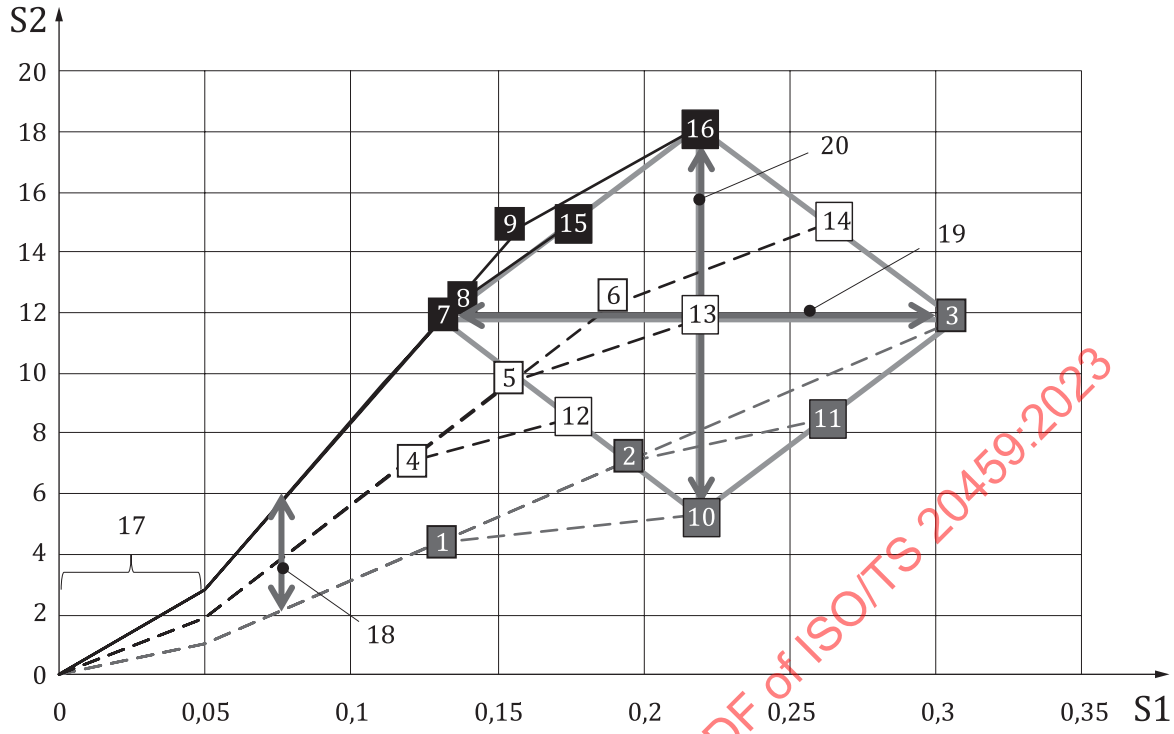

Key

1 yield stress/strain for HBM1
2 yield stress/strain for HBM2
3 yield/ultimate stress/strain for HBM3
4 yield stress/strain for HBM4
5 yield stress/strain for HBM5
6 yield stress/strain for HBM6
7 yield/ultimate stress/strain for HBM7
8 yield stress/strain for HBM8
9 yield stress/strain for HBM9
10 ultimate stress/strain for HBM1
11 ultimate stress/strain for HBM2
12 ultimate stress/strain for HBM4
13 ultimate stress/strain for HBM5
14 ultimate stress/strain for HBM6
15 ultimate stress/strain for HBM8
16 ultimate stress/strain for HBM9
17 half of young's modules region
18 90 % confidence interval (young's modulus)
19 90 % confidence interval (ultimate strain)
20 90 % confidence interval (ultimate stress)
S1 strain
S2 stress [MPa]

Figure A.3 — Stress-strain curves of the knee ligaments for the nine parametric HBMs

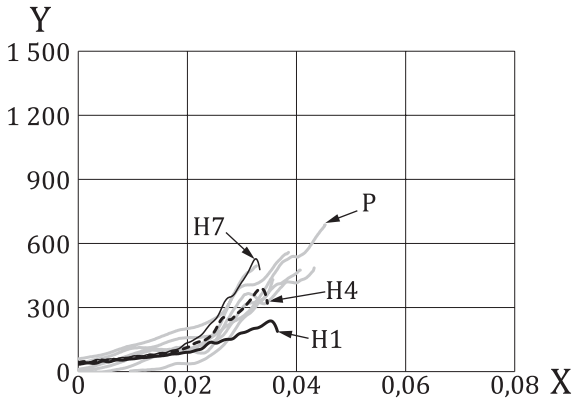

a) PMHSs and HBMs (H1, H4, H7)

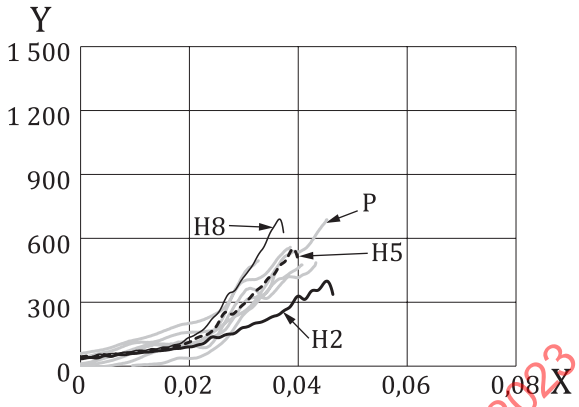

b) PMHSs and HBMs (H2, H5, H8)

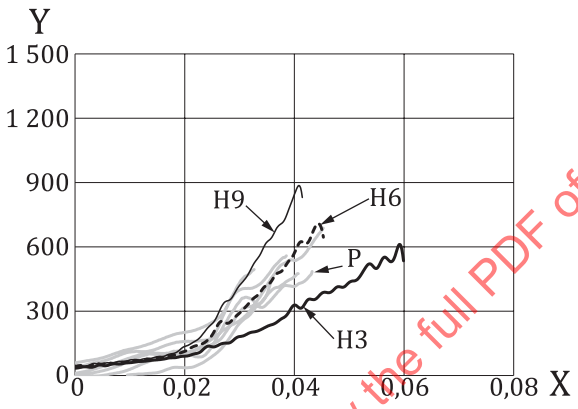

c) PMHSs and HBMs (H3, H6, H9)

Key

X deflection [m]
Y BM [Nm]
P PMHS test data
H1 computer simulation result of HBM-1
H2 computer simulation result of HBM-2
H3 computer simulation result of HBM-3
H4 computer simulation result of HBM-4
H5 computer simulation result of HBM-5
H6 computer simulation result of HBM-6
H7 computer simulation result of HBM-7
H8 computer simulation result of HBM-8
H9 computer simulation result of HBM-9

Figure A.4 — Comparison of BM-displacement curves for 3-point bending of the thigh between the nine parametric HBMs and PMHSs

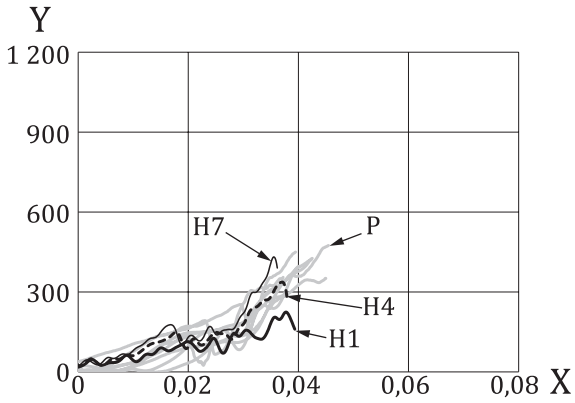

a) PMHSs and HBMs (H1, H4, H7)

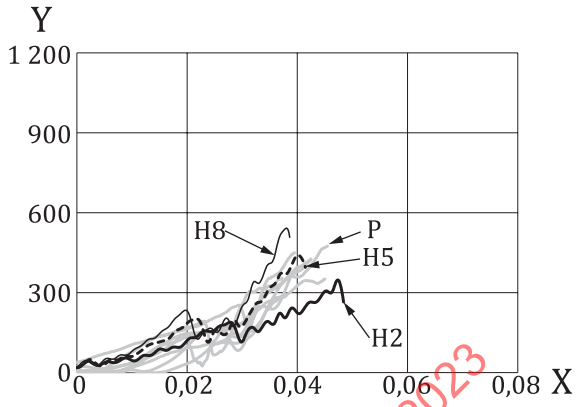

b) PMHSs and HBMs (H2, H5, H8)

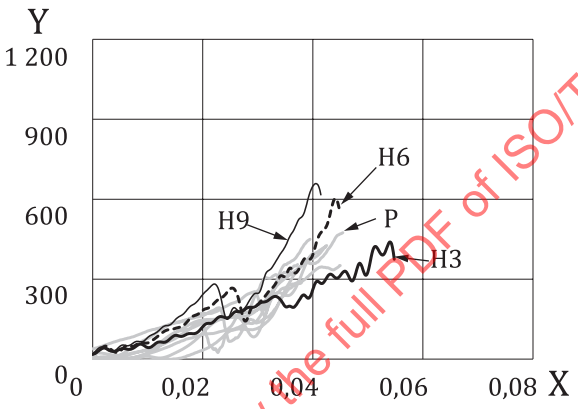

c) PMHSs and HBMs (H3, H6, H9)

Key

X deflection [m]
Y BM [Nm]
P PMHS test data
H1 computer simulation result of HBM-1
H2 computer simulation result of HBM-2
H3 computer simulation result of HBM-3
H4 computer simulation result of HBM-4
H5 computer simulation result of HBM-5
H6 computer simulation result of HBM-6
H7 computer simulation result of HBM-7
H8 computer simulation result of HBM-8
H9 computer simulation result of HBM-9

Figure A.5 — Comparison of BM-displacement curves for 3-point bending of the leg between the nine parametric HBMs and PMHSs

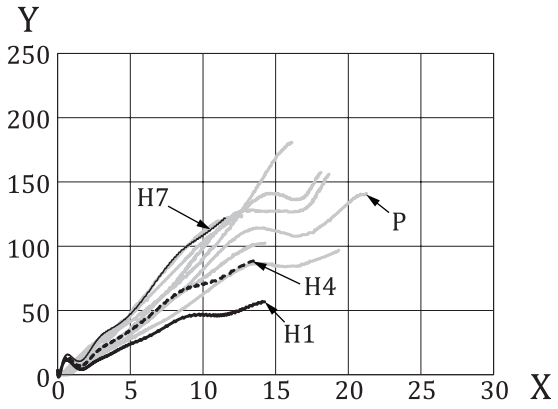

a) PMHSs and HBMs (H1, H4, H7)

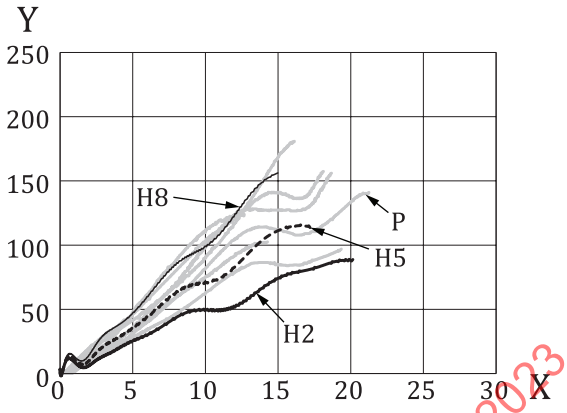

b) PMHSs and HBMs (H2, H5, H8)

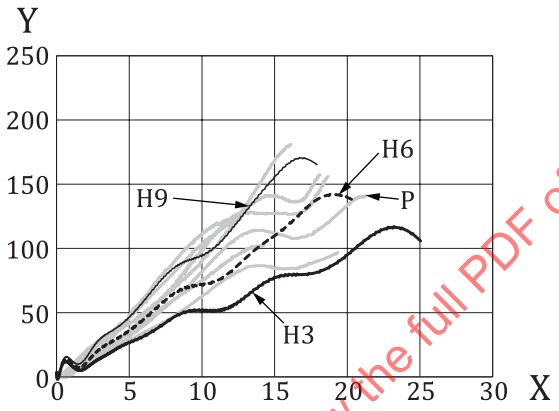

c) PMHSs and HBMs (H3, H6, H9)

Key

X knee valgus angle [°]
Y BM [Nm]
P PMHS test data
H1 computer simulation result of HBM-1
H2 computer simulation result of HBM-2
H3 computer simulation result of HBM-3
H4 computer simulation result of HBM-4
H5 computer simulation result of HBM-5
H6 computer simulation result of HBM-6
H7 computer simulation result of HBM-7
H8 computer simulation result of HBM-8
H9 computer simulation result of HBM-9

Figure A.6 — Comparison of BM-knee valgus angle curves for 4-point bending of the knee between the nine parametric HBMs and PMHSs

A.2.2.2.2 Transfer-function (TF) method

Due to the lack of sufficient full-scale pedestrian impact test data using human subjects, the TF method initially develops an IPF for humans based on biomechanical data using isolated lower limb segments, such as the thigh, the leg and the knee. Therefore, the IPF for humans represents failure tolerance of each individual lower limb segment. Next, a TF is determined for each lower limb segment by calculating a regression function between the maximum values of the corresponding injury metric for human

and the aPLI, when subjected to the same impacts. Impacts are delivered to a full-body pedestrian along with the full assembly of the aPLI to determine the function in a full-scale impact configuration to accurately represent the regression function under the load case specified in the STP. The lack of sufficient full-scale pedestrian impact test data requires the use of HBMs as opposed to actual human subjects. Since the use of computational modelling would make it possible to incorporate a number of different impact conditions with different types of cars at an affordable cost, injury values for the aPLI are also obtained from its computational model. IPFs for the aPLI are then developed by converting human IPFs to those of the aPLI using corresponding TFs. Figure A.7 shows a flow to develop IPFs for the aPLI using the TF method.

First, virtual IPFs for human were developed by applying the TF method to the virtual biomechanical data generated by the parametric HBMs. Nine sets of the thigh, the leg and the knee were isolated from the nine parametric HBMs. The thigh and the leg were subjected to lateral-to-medial mid-span dynamic 3-point bending to failure of the bones, while the knee was subjected to dynamic 4-point valgus bending to failure of the MCL. The maximum values of the BM were recorded for the thigh and the leg, while the maximum value of the knee valgus angle was obtained for the knee. Using the nine data for each of the lower limb components, virtual IPFs for human were developed by treating the data as exact data at failure and applying the Weibull survival analysis.

Next, TF was determined for each the thigh, the leg and the knee using one of the nine parametric HBMs that represents mean material property. The aPLI model developed in a pevious study[17] was also used. Since the aPLI does not represent failure of the tissues for repeatability, reproducibility and durability, the maximum value of an injury metric measured during an impact from a car may exceed the injury limits when an excessive load is applied. For this reason, failure representation of the HBM, except the fibula, was inactivated to correlate the maximum values of the injury metrics with those of the aPLI model under such conditions. Failure of the fibula was exceptionally activated so as to not underestimate loadings to the tibia, for which the injury metric is set for the aPLI. Thirty-six SCMs developed[17] were used to represent various load cases, with each of the 18 SCMs representing high-bumper and low-bumper cars. The aPLI model and the HBM were hit by each of the 36 SCMs in conformity to the STP. Specifically, the SCMs were made to collide with each of the HBM and the aPLI model in the lateral-to-medial direction at an impact speed of 11,1 m/s. As the bottom of the aPLI corresponds to the sole of a bare foot, the impact height of the aPLI model was set at 25 mm above the ground to compensate for the height of the sole of the shoe. As the length of the lower limb of the HBM is the same as that of the aPLI, and the mass of the shoe is combined with the foot model representing the shape of the bare foot, the impact height of the HBM was also set at 25 mm above the ground, as shown in Figure A.8. A gravity field is applied to the entire models. The lower limb orientation of the HBM was set such that the line connecting the centre of the hip joint and the ankle joint of the struck-side lower limb is vertical to the ground, and the same line on the non-struck side is rotated 20° forward about the hip joint, as shown in Figure A.9.

Injury metrics of the HBM and the aPLI model were measured at the locations illustrated in Figure A.10. The measurement locations on the femur and the tibia are labelled femur-1 through femur-3 and tibia-1 through tibia-4, respectively, in the ascending order from the location closest to the knee joint. The maximum values of the injury metrics for the thigh, the leg and the knee were recorded and used for regression analysis to develop virtual TFs. The BM was used as the injury metric for the femur and the tibia of the HBM and the aPLI model. In terms of the knee injury metric, the PMHS component tests to be used to develop the IPF for humans measure the knee valgus angle, rather than the elongation of the MCL, due to the need for the use of intact knees to ensure biofidelic response measurements. As the aPLI is capable of directly measuring elongation of the MCL, a transfer function was determined between the knee valgus angle of the HBM and the MCL elongation of the aPLI model. The femur BM and the tibia BM of the HBM were measured about the x-axis of the local coordinate system defined for each of the cross sections of the bones and affixed to the nodes comprising the solid elements that define the cross sections. The x-axis of all cross sections was initially oriented anteroposteriorly as shown in Figure A.10 in conformity to the BM measurement of the aPLI and FlexPLI.

The BM on the femur and the tibia/fibula of the HBM was measured by the section moment defined by the elements closest to the measurement locations of the aPLI. For the leg, the summation of the section moment on the tibia and the fibula was used for the assessment because these two bones are represented by a single bone core installed in the leg of the aPLI. The knee valgus angle was measured

by the local coordinate system defined at the knee-joint centre. The two nodes at the origin of the coordinate system were rigidly attached to the node on the femoral condyle and the tibial plateau with the closest proximity to these nodes to measure the angle of the tibia relative to the femur.

The femur BM and the tibia BM of the aPLI FE model were obtained by measuring the strain of the elements on the bone core closest to the measurement location of the aPLI hardware unit and converting it to bending moment using the sensitivity determined in a 3-point bending simulation of the bone core. The MCL elongation was directly measured by the elongation of the bar element simulating the MCL of the aPLI hardware.

The virtual TFs for the thigh and the leg were developed as linear regression functions with zero intercept determined between the maximum values of the BM obtained from the HBM and the aPLI model. In accordance with the STP, the maximum value of the BM was determined, for each the thigh and the leg, by the maximum of the maximum values obtained from multiple measurement locations (three and four locations on the femur and the tibia, similar to those of the aPLI). The virtual TF for the knee was developed by applying the same methodology as that used for the thigh and the leg, with the exception that the regression function was determined between different injury metrics (knee valgus angle for the HBM and the MCL elongation for the aPLI model).

Finally, the virtual IPFs for the aPLI were developed by applying the TFs determined above to the injury metrics for the HBM that define the virtual IPFs for human. Specifically, the virtual IPFs for the aPLI were determined using Formula (A.1):

$$\boldsymbol{P} = \boldsymbol{F}(\boldsymbol{I}_{\mathbf{human}}) = \boldsymbol{F}(\boldsymbol{G}(\boldsymbol{I}_{\mathbf{aPLI}})) \tag{A.1}$$

where

P is the probability of injury of human;

F is the IPF for human;

G is the transfer function;

I_{human} is the injury metric for human;

I_{aPLI} is the injury metric for the aPLI.

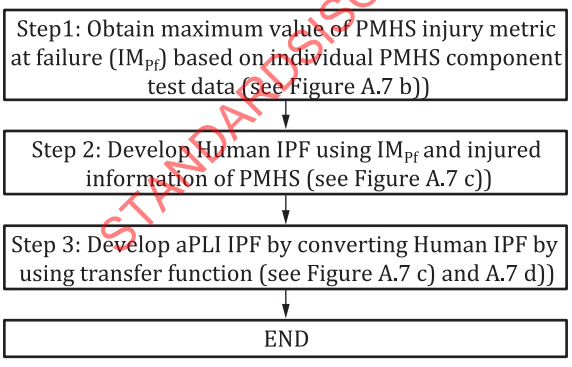

a) Flow chart for TF method

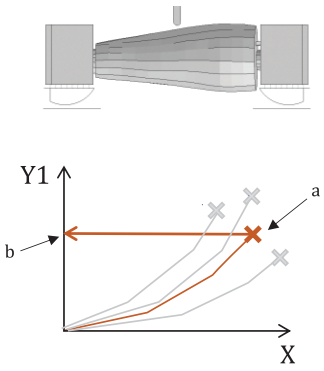

b) Schematic image of PMHS failure test and data

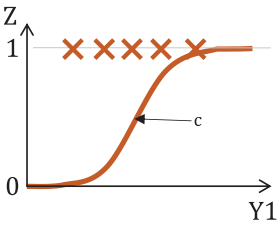

c) Schematic image of human IPF

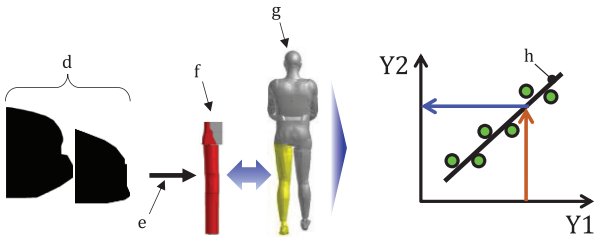

d) Schematic image of TF

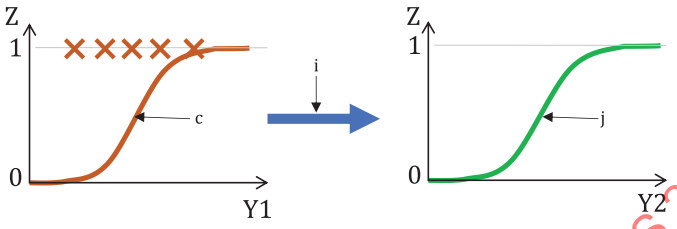

e) Schematic image of conversion

Key

X PMHS input (e.g. deflection)
Y1 PMHS injury metric
Y2 aPLI injury metric
Z human injury probability
a Injured.
b Maximum value of PMHS injury metric at failure (IM_{pf}).
c Human IPF.
d Car models.
e 11,1 m/s.
f aPLI model.
g HBM.
h TF (regression line).
i Conversion by using TF.
j aPLI IPF.

Figure A.7 — Development flow of IPF for human by means of the TF method

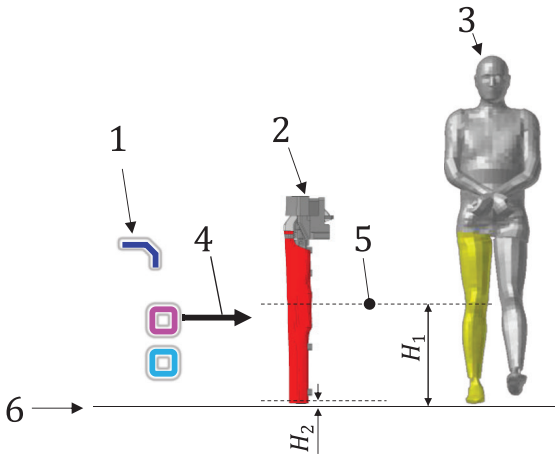

Key

1 SCM
2 aPLI FE model
3 HBM
4 11,1 m/s
5 knee joint
6 ground level
H_1 519 mm
H_2 25 mm

Figure A.8 — Setting of impact height of the HBM and the aPLI model

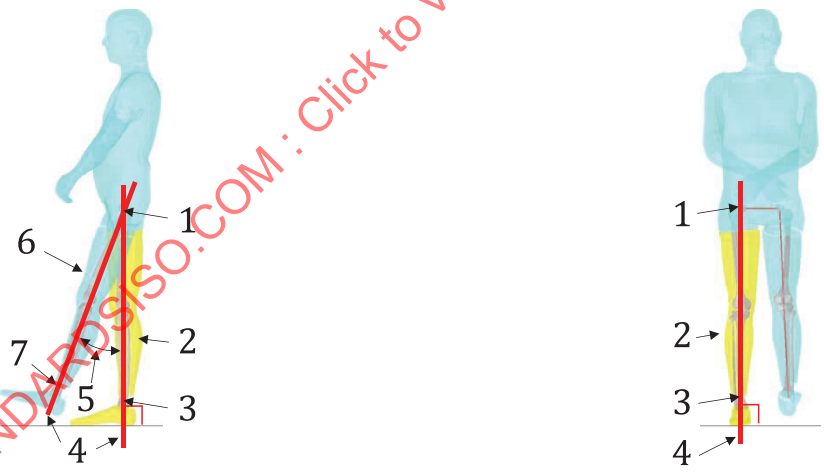

a) Struck-side view **b) Back view**

Key

1 hip-joint centre
2 struck side of vertical lower limb
3 ankle-joint centre
4 line connecting the centre of the hip joint and the ankle joint
5 20°
6 non-struck side of straight lower limb
7 ankle-joint centre

Figure A.9 — Lower-limb posture of the HBM

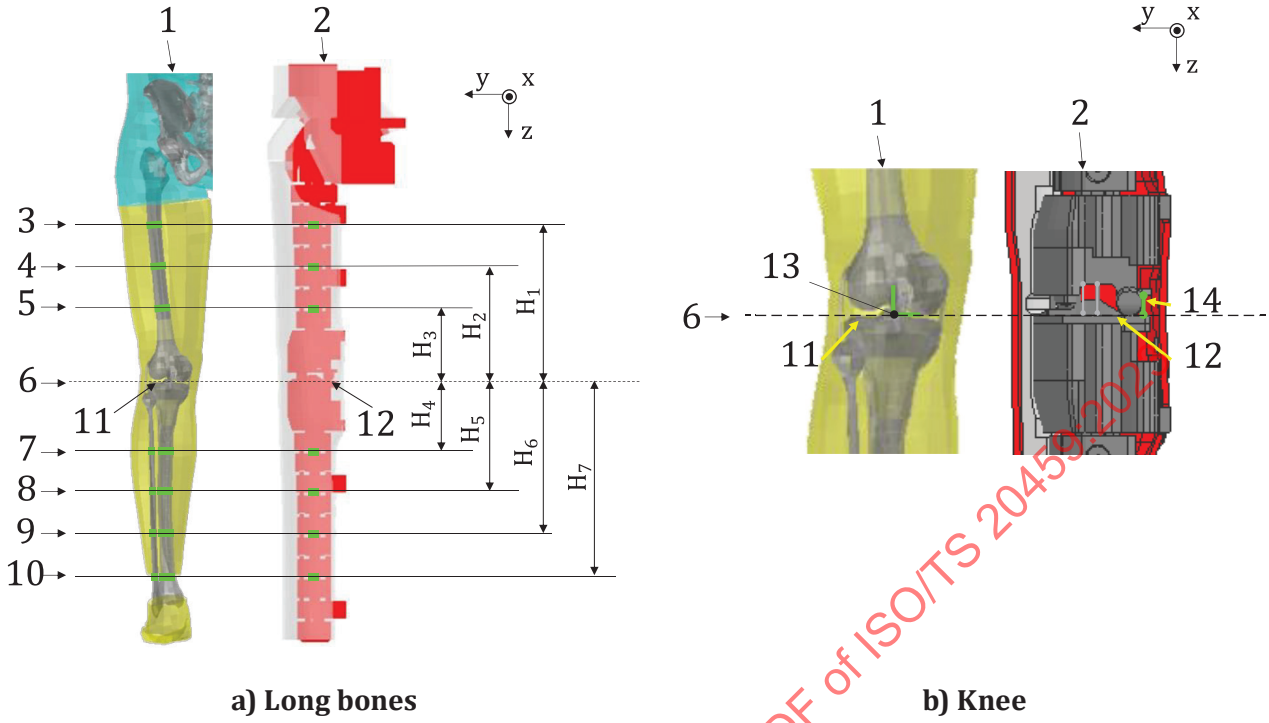

a) Long bones **b) Knee**

Key

1 HBM
2 aPLI FE model
3 BM measurement location (femur-3)
4 BM measurement location (femur-2)
5 BM measurement location (femur-1)
6 knee joint
7 BM measurement location (tibia-1)
8 BM measurement location (tibia-2)
9 BM measurement location (tibia-3)
10 BM measurement location (tibia-4)
11 tibial plateau
12 flat surface of tibial plateau
13 knee valgus angle measured at knee-joint centre
14 MCL elongation
H_1 297 mm
H_2 217 mm
H_3 137 mm
H_4 134 mm
H_5 214 mm
H_6 294 mm
H_7 374 mm

Figure A.10 — Measurement locations of the HBM and the aPLI model

A.2.2.2.3 Energy equivalent (EE) method

The assumption behind the EE method is that the deformation energy is the predictor of tissue failure. Given this assumption, injury occurrence is related to the aPLI injury value at the same deformation

energy as that absorbed by a human body up to the tissue failure. Component tests are used to establish this relationship due to the lack of sufficient full-scale pedestrian impact test data. For each individual human subject, a lower limb segment is subjected to a component test, such as a dynamic 3-point or 4-point test, and the deformation energy is calculated up to failure of the tissue. The same component test is performed using the corresponding aPLI segment, and the injury value at the same deformation energy is recorded. This develops a list of aPLI injury values corresponding to tissue failure of all the human subjects involved in the analysis. IPFs are determined by interpreting these injury values as those at failure. Figure A.11 shows a flow to develop IPFs for the aPLI using the EE method.

First, using the virtual biomechanical data generated by the parametric HBMs for the TF method as described in A.2.2.2.2, the deformation energy up to failure of the tissue (femur, tibia and MCL) was calculated for each of the nine parametric HBMs. The deformation energy up to failure was calculated by integrating the applied force in the 3-point bending simulation (thigh and leg) and the knee moment in the 4-point bending simulation (knee) with respect to the displacement of the indenter (thigh and leg) and the knee valgus angle (knee), respectively, from the initiation of the loading up to the initiation of the failure predicted by the HBM.

Second, each part of the lower limb (thigh, leg and knee) of the aPLI model was isolated, and dynamic 3-point bending simulation and dynamic 4-point bending simulation were performed with the thigh/leg and the knee, respectively, using the same boundary and loading conditions as those used for the HBM simulations. By applying the same methodology as that described above for the HBMs, the function defining the relationship between the injury value and the deformation energy was determined for the aPLI model for each of the injury metrics. For each combination of the nine parametric HBMs and the injury metrics, the aPLI injury value corresponding to the failure of the human tissue was determined by giving the deformation energy at failure obtained from the HBM to the function described above.

Finally, the resulting set of the nine aPLI injury values for each of the injury metrics was used to determine virtual IPF for the aPLI using the EE method by applying the Weibull survival analysis to each of the datasets and treating the data as exact.

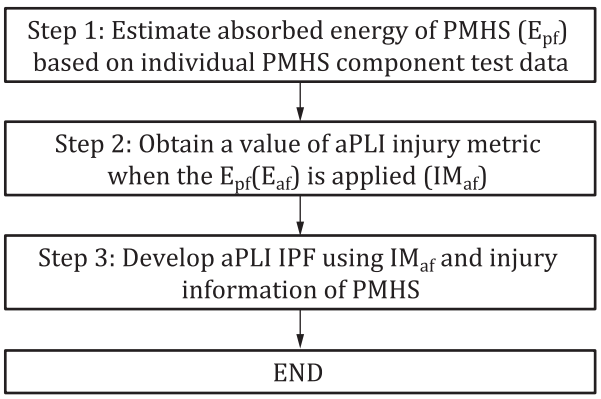

a) Flow chart for EE method

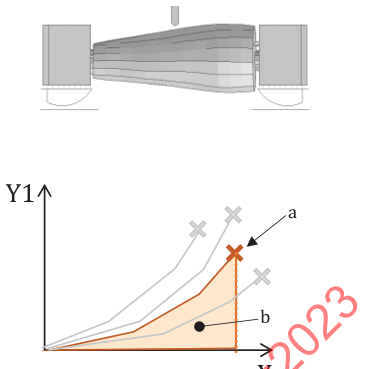

b) Schematic image of PMHS failure test and data

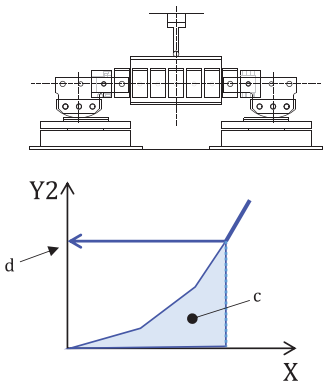

c) Schematic image of aPLI loading test and data

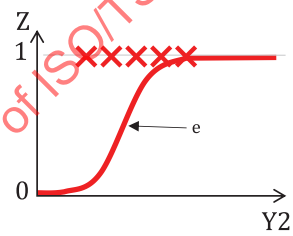

d) Schematic image of aPLI IPF

Key

X PMHS input (e.g. deflection)
Y1 PMHS injury metric
Y2 aPLI injury metric
Z human injury probability
a Injured.
b Estimated absorbed energy of PMHS (E_{pf}).
c Applied energy to aPLI (E_{af} = E_{pf}).
d A value of aPLI injury metric when the E_{pf} is applied (IM_{af}).
e aPLI IPF.

Figure A.11 — Development flow of IPF for human by means of the EE method

A.2.2.2.4 Paired test method

The paired test method (ISO/TR 12350) was used to derive IPFs for WorldSID, where full-scale human subjects and a full-scale dummy are subjected to an impact in the same loading condition, and IPFs for the dummy are derived by correlating occurrence of injuries to the human subjects and the maximum values of injury metrics for the specific body regions where the injuries occurred. Figure A.12 shows a flow to develop IPFs for the aPLI using the paired method.

First, the parametric HBMs and the aPLI model were subjected to impacts from SCMs. In order to develop reliable IPFs using the paired test method, the HBM impact simulations needed to provide data both

with injury and without injury, preferably with an even distribution, to a specific tissue (femur, tibia and MCL) to be assessed. Due to different tolerances and loading mechanisms of the tissues, different sets of nine SCMs needed to be used to obtain such data for the different tissues. The nine SCMs for the femur and the tibia were selected from the 36 SCMs[17] or 20 SCMs specified in A.2.4.2.2, while three modified SCMs as specified in Figure A.13, Figure A.14, Table A.2 and Table A.3 needed to be used, in addition to the six SCMs chosen from the set of 36 SCMs, to deliver impacts with no injury to the MCL. For the same reason, five impact speeds, with specific levels being different among different tissues, were also used. For each combination of the lower limb region and the impact speed, the combination of the nine SCMs and the nine parametric HBMs was randomly determined to reduce the number of simulation runs while maintaining evenly distributed probability of tissue failure. This resulted in 45 simulation runs for each of the lower limb regions. The simulation matrix is shown in Table A.1. In the table, the initial capital letter of the impact simulation case identifier denotes the specific lower limb region (T: thigh, L: leg, K: knee) for which an IPF was calculated using the data. The simplified car model identifier starting from either 'sedan' or 'SUV' are those selected from the set of 36 SCMs, while the identifier starting from 'Car' denotes the three modified SCMs specifically used for the knee. In addition, the human body model identifier corresponds to that described in A.2.2.2.1. The impact simulation setup, except impact speed, is the same as described in A.2.2.2.2. The aPLI model was subjected to impacts in all of the 135 load cases listed in Table A.1.

Next, the maximum values of the injury metrics of the aPLI model were linked with the occurrence of injury (with/without injury) predicted by the corresponding HBM impact simulations. Since the aPLI does not simulate failure of tissues and injury values may read beyond the tolerance of the tissues, aPLI injury values corresponding to 'injury' and 'no injury' were treated as left censored data and right censored data, respectively. The virtual IPFs for the aPLI using the paired method were developed by means of the Weibull survival analysis.

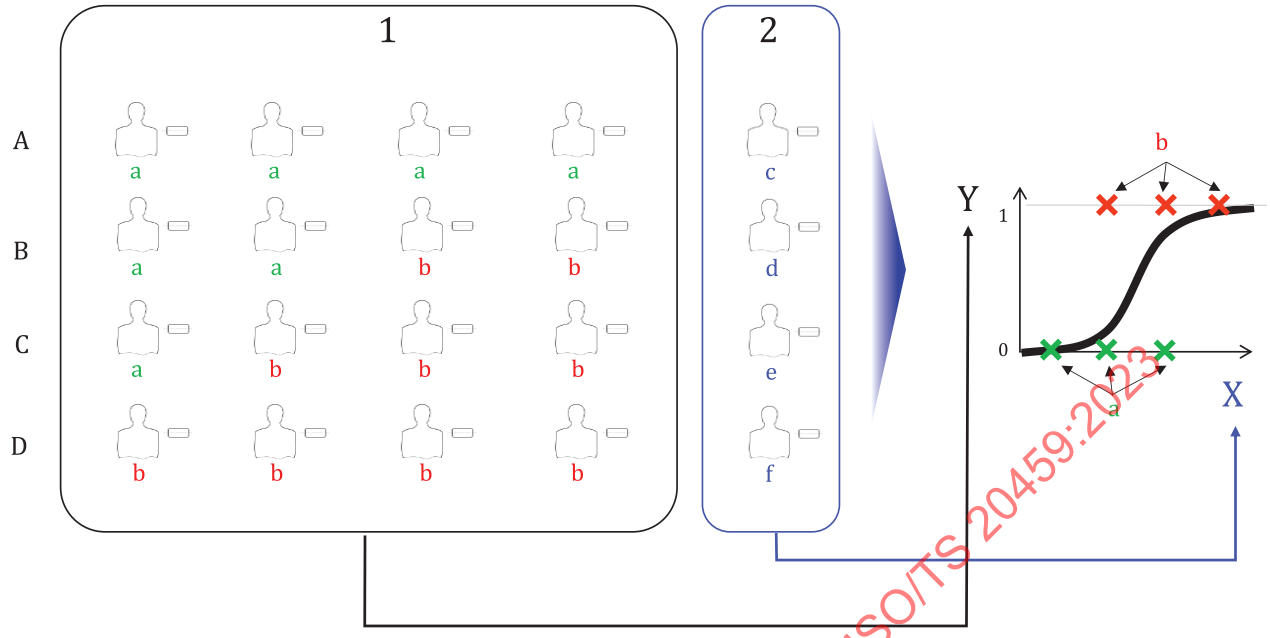

Key

X ATD injury metrics (e.g. force)
Y human injury probability
1 PMHS test
2 ATD test
A load case (A)
B load case (B)
C load case (C)
D load case (D)
a Intact.
b Injury.
c A value of ATD injury metric observed in load case (A).
d A value of ATD injury metric observed in load case (B).
e A value of ATD injury metric observed in load case (C).
f A value of ATD injury metric observed in load case (D).

Figure A.12 — Development Flow of IPF for human by means of the paired test method

Table A.1 — HBM impact simulation matrix for the virtual paired test method

Case	S	SCM	HBM	Case	S	SCM	HBM	Case	S	SCM	HBM
T-1	30	J-SDN-13	HBM-3	L-1	30	Sedan12	HBM-3	K-1	10	Car-PC	HBM-3
T-2	30	SUV09	HBM-9	L-2	30	SUV11	HBM-9	K-2	10	Sedan08	HBM-9
T-3	30	SUV11	HBM-4	L-3	30	SUV01	HBM-4	K-3	10	Sedan18	HBM-4
T-4	30	J-LoBP-SUV-09	HBM-8	L-4	30	Sedan17	HBM-8	K-4	10	Car-PA	HBM-8
T-5	30	J-SDN-10	HBM-2	L-5	30	Sedan05	HBM-2	K-5	10	Sedan07	HBM-2

Key

Case	impact simulation case identifier
S	impact speed [km/h]
SCM	simplified car model identifier
HBM	human body model identifier

Table A.1 *(continued)*

Case	S	SCM	HBM	Case	S	SCM	HBM	Case	S	SCM	HBM
T-6	30	J-SDN-02	HBM-7	L-6	30	Sedan08	HBM-7	K-6	10	Car-PB	HBM-7
T-7	30	Sedan12	HBM-1	L-7	30	SUV02	HBM-1	K-7	10	Sedan06	HBM-1
T-8	30	SUV05	HBM-5	L-8	30	SUV04	HBM-5	K-8	10	Sedan10	HBM-5
T-9	30	J-SDN-14	HBM-6	L-9	30	SUV15	HBM-6	K-9	10	Sedan11	HBM-6
T-10	40	J-SDN-02	HBM-3	L-10	40	Sedan08	HBM-3	K-10	20	Car-PB	HBM-3
T-11	40	J-SDN-14	HBM-1	L-11	40	SUV15	HBM-1	K-11	20	Sedan11	HBM-1
T-12	40	SUV09	HBM-2	L-12	40	SUV11	HBM-2	K-12	20	Sedan08	HBM-2
T-13	40	Sedan12	HBM-8	L-13	40	SUV02	HBM-8	K-13	20	Sedan06	HBM-8
T-14	40	SUV05	HBM-7	L-14	40	SUV04	HBM-7	K-14	20	Sedan10	HBM-7
T-15	40	J-LoBP-SUV-09	HBM-6	L-15	40	Sedan17	HBM-6	K-15	20	Car-PA	HBM-6
T-16	40	SUV11	HBM-5	L-16	40	SUV01	HBM-5	K-16	20	Sedan18	HBM-5
T-17	40	J-SDN-13	HBM-9	L-17	40	Sedan12	HBM-9	K-17	20	Car-PC	HBM-9
T-18	40	J-SDN-10	HBM-4	L-18	40	Sedan05	HBM-4	K-18	20	Sedan07	HBM-4
T-19	50	Sedan12	HBM-3	L-19	50	SUV02	HBM-3	K-19	30	Sedan06	HBM-3
T-20	50	SUV09	HBM-5	L-20	50	SUV11	HBM-5	K-20	30	Sedan08	HBM-5
T-21	50	J-SDN-02	HBM-9	L-21	50	Sedan08	HBM-9	K-21	30	Car-PB	HBM-9
T-22	50	J-SDN-14	HBM-8	L-22	50	SUV15	HBM-8	K-22	30	Sedan11	HBM-8
T-23	50	J-LoBP-SUV-09	HBM-4	L-23	50	Sedan17	HBM-4	K-23	30	Car-PA	HBM-4
T-24	50	SUV11	HBM-7	L-24	50	SUV01	HBM-7	K-24	30	Sedan18	HBM-7
T-25	50	J-SDN-10	HBM-2	L-25	50	Sedan05	HBM-2	K-25	30	Sedan07	HBM-2
T-26	50	J-SDN-13	HBM-1	L-26	50	Sedan12	HBM-1	K-26	30	Car-PC	HBM-1
T-27	50	SUV05	HBM-6	L-27	50	SUV04	HBM-6	K-27	30	Sedan10	HBM-6
T-28	60	SUV11	HBM-6	L-28	60	SUV01	HBM-6	K-28	40	Sedan18	HBM-6
T-29	60	Sedan12	HBM-4	L-29	60	SUV02	HBM-4	K-29	40	Sedan06	HBM-4
T-30	60	J-SDN-13	HBM-9	L-30	60	Sedan12	HBM-9	K-30	40	Car-PC	HBM-9
T-31	60	J-SDN-14	HBM-3	L-31	60	SUV15	HBM-3	K-31	40	Sedan11	HBM-3
T-32	60	J-LoBP-SUV-09	HBM-7	L-32	60	Sedan17	HBM-7	K-32	40	Car-PA	HBM-7
T-33	60	SUV09	HBM-2	L-33	60	SUV11	HBM-2	K-33	40	Sedan08	HBM-2
T-34	60	SUV05	HBM-1	L-34	60	SUV04	HBM-1	K-34	40	Sedan10	HBM-1
T-35	60	J-SDN-02	HBM-8	L-35	60	Sedan08	HBM-8	K-35	40	Car-PB	HBM-8
T-36	60	J-SDN-10	HBM-5	L-36	60	Sedan05	HBM-5	K-36	40	Sedan07	HBM-5
T-37	70	J-LoBP-SUV-09	HBM-2	L-37	70	Sedan17	HBM-2	K-37	50	Car-PA	HBM-2
T-38	70	Sedan12	HBM-1	L-38	70	SUV02	HBM-1	K-38	50	Sedan06	HBM-1
T-39	70	SUV05	HBM-8	L-39	70	SUV04	HBM-8	K-39	50	Sedan10	HBM-8
T-40	70	J-SDN-10	HBM-3	L-40	70	Sedan05	HBM-3	K-40	50	Sedan07	HBM-3
T-41	70	J-SDN-13	HBM-7	L-41	70	Sedan12	HBM-7	K-41	50	Car-PC	HBM-7
T-42	70	J-SDN-02	HBM-4	L-42	70	Sedan08	HBM-4	K-42	50	Car-PB	HBM-4
T-43	70	J-SDN-14	HBM-9	L-43	70	SUV15	HBM-9	K-43	50	Sedan11	HBM-9
T-44	70	SUV09	HBM-5	L-44	70	SUV11	HBM-5	K-44	50	Sedan08	HBM-5

Key

Case	impact simulation case identifier
S	impact speed [km/h]
SCM	simplified car model identifier
HBM	human body model identifier

Table A.1 *(continued)*

Case	S	SCM	HBM	Case	S	SCM	HBM	Case	S	SCM	HBM
T-45	70	SUV11	HBM-6	L-45	70	SUV01	HBM-6	K-45	50	Sedan18	HBM-6

Key

Case	impact simulation case identifier
S	impact speed [km/h]
SCM	simplified car model identifier
HBM	human body model identifier

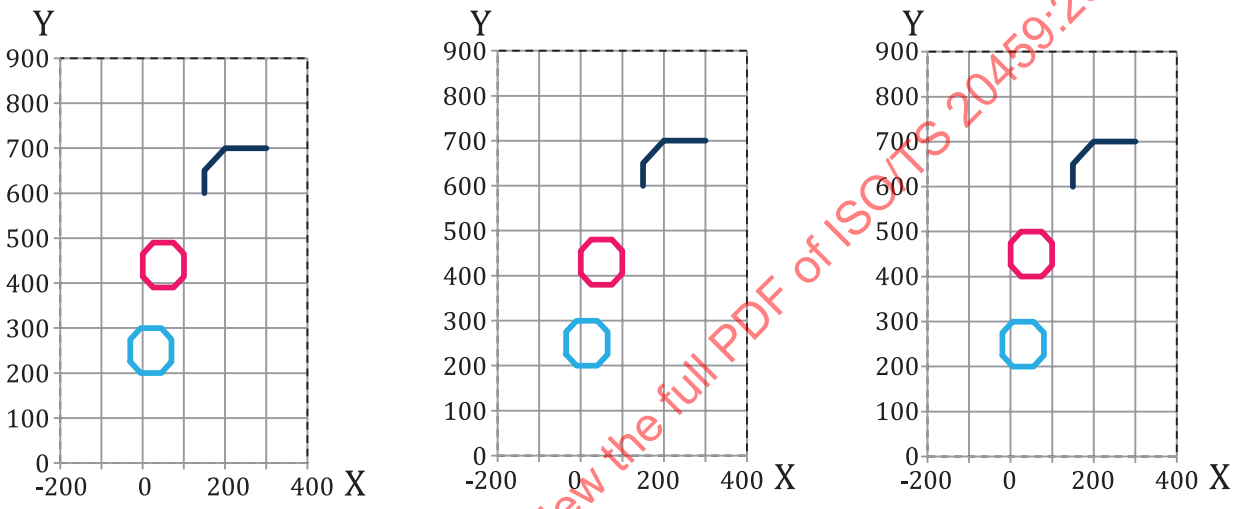

a) Car-PA **b) Car-PB** **c) Car-PC**

Key

X horizontal dimensions [mm]

Y vertical dimensions [mm]

Figure A.13 — Geometry of additional SCMs (car-PA, car-PB and car-PC) to develop a virtual IPF for the knee by using the pared test method

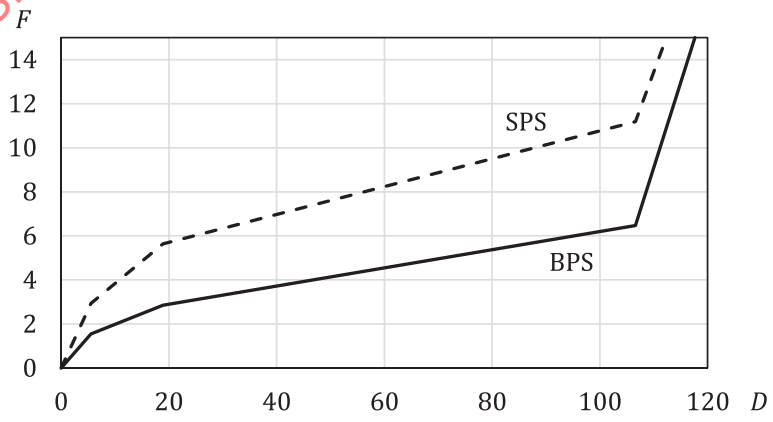

a) Bumper and spoiler stiffness

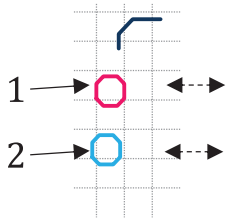

b) Direction of deflection

Key

1	bumper
2	spoiler
F	force [kN]
D	deflection [mm]
BPS	bumper stiffness curve specified for car-PA, car-PB and car-PC
SPS	spoiler stiffness curve specified for car-PA, car-PB and car-PC

Figure A.14 — Stiffness curves specified for the bumper and spoiler of the three SCMs (car-PA, car-PB, car-PC)

Table A.2 — Tabulated geometry data of three SCMs (car-PA, car-PB, car-PC)

SCM ID	Dimensions in millimeters				
	H1	H2	H3	L1	L2
Car-PA	700	440	250	200	-30
Car-PB	700	430	250	200	-35
Car-PC	700	450	250	200	-20

Key

1	bonnet leading edge (BLE)
2	bumper (BP)
3	spoiler (SP)
H1	BLE height
H2	bumper centre height
H3	spoiler centre height
L1	bonnet lead
L2	SP lead

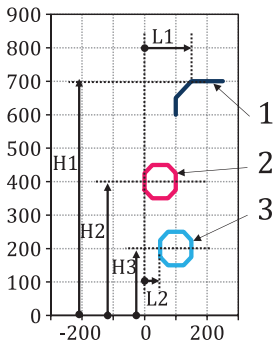

Table A.3 — Tabulated stiffness data specified for bumper and spoiler of three SCMs (car-PA, car-PB, car-PC)

Bumper		Spoiler	
D	F	D	F
0,0	0	0,0	0

Key

D	deflection [mm]
F	force [kN]
BP	bumper stiffness curve specified for car-PA, car-PB and car-PC
SP	spoiler stiffness curve specified for car-PA, car-PB and car-PC

Table A.3 *(continued)*

Bumper		Spoiler	
D	**F**	**D**	**F**
5,6	1,5	5,6	2,9
18,9	2,9	18,9	5,6
106,6	6,5	106,6	11,2
150,0	40,0	150,0	40,0

Key

D deflection [mm]

F force [kN]

BP bumper stiffness curve specified for car-PA, car-PB and car-PC

SP spoiler stiffness curve specified for car-PA, car-PB and car-PC

A.2.2.3 Assessment of methods

Due to the lack of suitable and sufficient biomechanical data, an alternative methodology to develop the IPFs for the aPLI to the paired test method described in ISO/TR 12350 needed to be defined. In order to select one of the proposed methodologies (TF method or EE method), biomechanical data were virtually generated to develop IPFs using the three methods (TF method, EE method and paired test method) as described in A.2.2.2, and the IPFs determined using the TF method and the EE method were compared against the IPFs calculated using the paired test method to identify the methodology that provides the IPFs that better represent those from the paired test method.

The use of the EE method described in A.2.3.2.3 requires calculation of the deformation energy from the biomechanical data, while the TF method requires only the maximum values of the injury metrics as described in A.2.2.2.2. For this reason, the availability of sufficient data from that literature was also analysed.

A.2.2.3.1 Assessment against virtual paired test method

Figure A.15 through Figure A.17 shows the comparison of the virtual IPFs for the aPLI developed by using the TF method, EE method and paired test method. The virtual IPFs developed by using the TF method better represent those of the paired test method than that developed using the EE method. The normalized errors of the injury value at 50 % probability of injury relative to the IPF developed using the paired test method were 12,1 %, 1,0 % and 0,5 % for the TF method, and 23,1 %, 21,0 % and 7,4 % for the EE method, for the thigh, the leg and the knee, respectively. These results indicate that use of the TF method is recommended as an alternative method to the paired test method recommended by ISO.

Note that the reliability of the conclusion depends on the validity of the baseline and parametric HBMs used in this analysis. See Tables A.5 and A.6 for the parameters of virtual aPLI IPF for the MCL complete rupture and for the femus shaft (Weibull distribution).

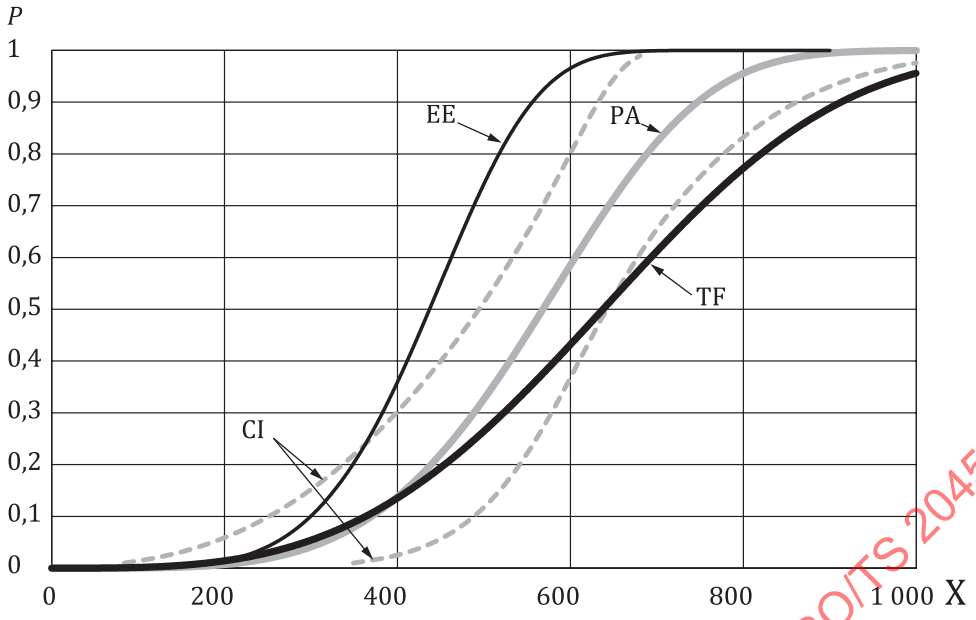

Key

X aPLI femur BM [Nm]

P probability of femur shaft fracture

TF virtual aPLI IPF for femur shaft fracture developed by using TF method

EE virtual aPLI IPF for femur shaft fracture developed by using EF method

PA virtual aPLI IPF for femur shaft fracture developed by using paired test method

CI 95 % confidence interval

Figure A.15 — Virtual aPLI IPFs for the femur shaft fracture developed by using the TF method, EE method and paired test method

Table A.4 — Parameters of virutal aPLI IPF for the femur shaft (Wibull distribution)

Deveopment method	C_{Scale}	C_{Shape}
TF	711	3,35
EE	470	4,99
Paired	618	4,39

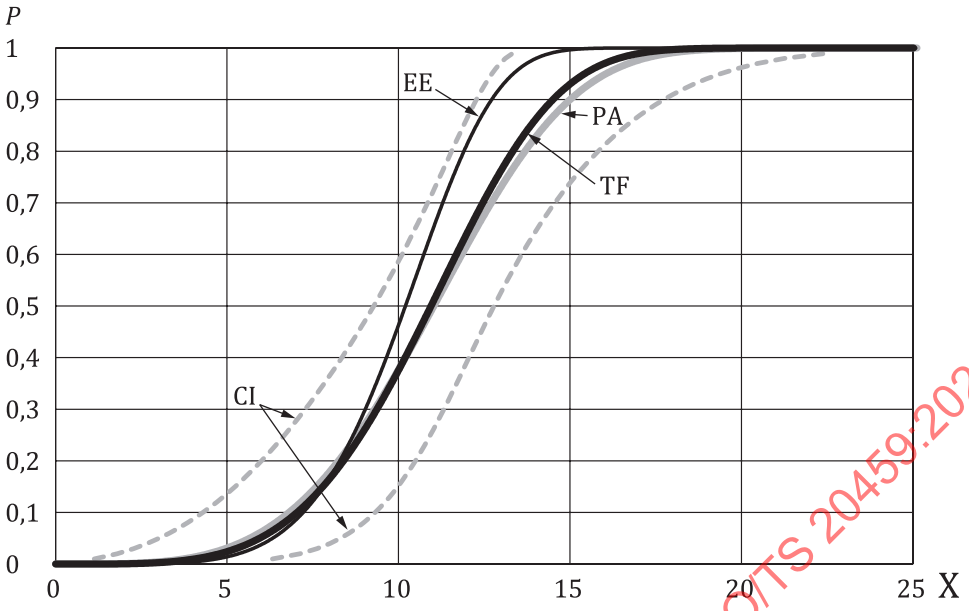

Key

Y aPLI MCL elongation [mm]
P probability of MCL complete rupture
TF virtual aPLI IPF for MCL complete rupture developed by using TF method
EE virtual aPLI IPF for MCL complete rupture developed by using EE method
PA virtual aPLI IPF for MCL complete rupture developed by using paired test method
CI 95 % confidence interval

Figure A.16 — Virtual aPLI IPFs for the MCL complete rupture developed by using the TF method, EE method and paired test method

Table A.5 — Parameters of virtual aPLI IPF for the MCL complete rupture (Weibull distribution)

Development method	C_{Scale}	C_{Scale}
TF	12,0	4,27
EE	10,9	5,45
Paired	12,1	3,90

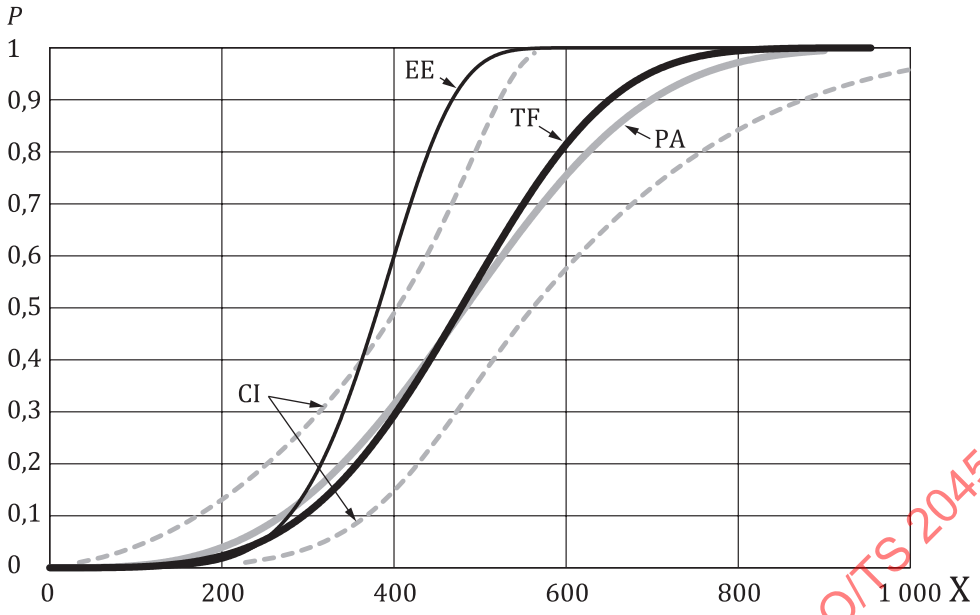

Key

X aPLI tibia BM [Nm]
P probability of tibia shaft fracture
TF virtual aPLI IPF for tibia shaft fracture developed by using TF method
EE virtual aPLI IPF for tibia shaft fracture developed by using EE method
PA virtual aPLI IPF for tibia shaft fracture developed by using paired test method
CI 95 % confidence interval

Figure A.17 — Virtual aPLI IPFs for the tibia shaft fracture developed by using the TF method, EE method and paired test method

Table A.6 — Parameters of virtual aPLI IPF for the femur shaft (Weibull distribution)

Development Method	C_{Scale}	C_{Shape}
TF	525	3,90
EE	406	5,92
Paired	540	3,24

A.2.2.3.2 Assessment of number of biomechanical data

Table A.7 summarizes the availability of maximum values of injury metrics used for the TF method, and the availability of diagrams (BM – indenter displacement for the thigh/leg, BM - valgus angle for the knee) used for the EE method, from the literature (see [13], [15], [14], [16], [18], [19], [20], [21], [22] and [23]). The number of available data is significantly smaller for those with diagrams.

Table A.7 — Availability of maximum values of injury metrics and diagrams from the literature

Body region	Reference	Number of tests	
		Maximum value of injury metrics	Diagram
Thigh	Kerrigan et al. (2003a)	4	1
	Kerrigan et al. (2004)	6	6
	Funk et al. (2004)	15	0
	Ivarsson et al. (2009)	10	10
	Total	35	17
Leg	Nyquist et al. (1985)	9	0
	Kerrigan et al. (2003a)	4	1
	Kerrigan et al. (2003b)	6	0
	Kerrigan et al. (2004)	4	4
	Total	23	5
Knee	Kajzer et al. (1997)	9	0
	Kajzer et al. (1999)	3	0
	Bose et al. (2004)	8	8
	Bose et al. (2008)	8	0
	Total	28	8

A.2.2.3.3 Conclusions

Based on the results of A.2.2.3.1 and A.2.2.3.2 discussed at the 9th aPLI TG meeting in London, the aPLI TG decided to use the TF method.

A.2.3 Development of IPFs for human

A.2.3.1 General

Biomechanical data consistent with the load case under which the subsystem test is performed with the aPLI were taken from the literature. In terms of the anthropometry, the height and the weight of human subjects were used as covariates in the statistical prediction modelling to control for a 50th percentile male represented by the aPLI.[3] In addition, the age was also controlled for the average age of all the subjects used in the experiments from which human biomechanical data were obtained (see Annex A.2.3.3). Only the past studies where these anthropometric parameters are specified were referenced. Data were collected from the studies that dynamically tested the isolated thigh and/or the leg (femur and/or tibia/fibula surrounded by the flesh and the skin) in the lateral-medial 3-point bending, and the studies that dynamically tested the intact knee in valgus bending. In addition, the injury metrics specified in the scope of the IPFs (femur and tibia BM, knee valgus angle; see Annex A.2.3.3.1) needed to be measured by the studies. The statistical procedure described in ISO/TS 18506 was employed to establish statistical prediction models.

A.2.3.2 Statistical prediction modelling

In the statistical prediction modelling, survival analysis was used to determine the injury probability function, with the height, the weight and the age of a subject defined as covariates.

With regard to data censoring, injury and intact (no injury) data were treated as exact and right censored data, respectively. In cases where a low-pass filter was applied, data were treated as right censored data due to attenuation of the maximum values. Data for the femur and the tibia obtained from the experiments using the specimens without the flesh were treated as right censored data considering the reduction of the maximum values due to the lack of load distribution provided by the flesh[14].

Within the three distributions recommended by ISO/TS 18506, one of the three distributions (Weibull distribution, Log-Normal distribution and Log-Logistic distribution; best fit to data) is used to define human IPFs for each of the injury metrics based on the score of Akaike's information criterion (AIC). The smallest score of the AIC means the best fit to data. The formulae of the human IPFs for these distributions are presented below.

The injury probability when the Weibull distribution is applied [Formula (A.2)]:

$$P = 1 - \exp\left\{-\left(\frac{x_{\text{human}}}{C_{\text{Scale}}}\right)^{C_{\text{Shape}}}\right\} \tag{A.2}$$

where

P is the injury probability of human;

C_{Scale} is the parameter determined for the Weibull distribution for human IPFs;

C_{Shape} is the parameter determined for the Weibull distribution for human IPFs;

C_{Slope} is the slope of the transfer function (TF);

x_{human} is the value of the injury metric for human.

The injury probability when the Log-Normal distribution is applied [Formula (A.3)]:

$$P = \frac{1}{C_{\sigma}\sqrt{2\pi}} \int_0^{x_{\text{human}}} \frac{1}{t} \exp\left\{\frac{-\left(\ln t - C_{\mu}\right)^2}{2{C_{\sigma}}^2}\right\} dt \tag{A.3}$$

where

P is the injury probability of human;

C_{μ} is the parameter determined for the Log-Normal distribution for human IPFs;

C_{σ} is the parameter determined for the Log-Normal distribution for human IPFs;

C_{Slope} is the slope of the TF;

x_{human} is the value of the injury metric for human.

The injury probability when the Log-Logistic distribution is applied [Formula (A.4)]:

$$P = \frac{1}{1 + \left(\frac{x_{\text{human}}}{\exp(C_{\text{Scale}})}\right)^{\frac{-1}{C_{\text{Shape}}}}} \tag{A.4}$$

where

P is the injury probability of human;

C_{Scale} is the parameter determined for the Log-Logistic distribution for human IPFs;

C_{Shape} is the parameter determined for the Log-Logistic distribution for human IPFs;

C_{Slope} is the slope of the TF;

x_{human} is the value of the injury metric for human.

A.2.3.3 Biomechanical data

A.2.3.3.1 Data collection

Human biomechanical data obtained from past experimental studies were collected from the literature. The following inclusion criteria were set to generate IPFs for human consistent with the conditions and the load case specified by the STP under which aPLI car tests are performed:

— regions of the lower limb: thigh, leg and knee;

— specific injuries reproduced: femur shaft fracture, tibia shaft fracture and MCL complete rupture;

— injury metrics: thigh BM, tibia BM and knee valgus angle;

— loading rate: equivalent to a 11,1 m/s car-pedestrian collision;

— loading direction: lateral-to-medial, anterior-to-posterior and posterior-to-anterior for the thigh and lateral-to-medial for the leg and the knee;

— lower-limb posture: fully-extended knee.

In addition to the lateral-to-medial loading direction (STP loading direction), posterior-to-anterior and anterior-to-posterior loading direction were also accepted for the thigh because the bending tolerance of the thigh is not sensitive to the loading direction due to the circular cross-sectional shape of the femoral shaft[23]).

The IPFs for the aPLI shall be developed for the thigh, leg and knee that comprises a human lower limb for which the aPLI measures injury values.

Femur shaft fracture, tibia shaft facture and MCL complete rupture were selected because these are the primary injuries to the three lower limb regions specified (References [8] and [24]). Although not necessarily frequent compared to bone fractures, MCL failure was included considering long-term consequences of the injury[25]. Failure of the ACL and PCL were not included because isolated failure of these ligaments is rare in pedestrian accidents[26] and is typically accompanied by MCL failure[16]. Bending moment was used as an injury metric for femur fracture and tibia fracture because bending moment was found to be the best predictor of those injuries in car-pedestrian impacts[27]. MCL elongation was chosen because failure of ligaments was found to be solely determined by the ultimate strain[28],[29]. Due to the lack of biomechanical data for MCL elongation, the knee valgus angle was used to describe the IPF for the human knee as the knee valgus angle determines the elongation of the MCL in lateral bending of the knee that occurs in a lateral impact specified in the STP.

The load case for which IPFs for human are to be developed followed that specified by the STP. The loading rate of a component shall be equivalent to the impact speed of 11,1 m/s. The impact direction shall be the lateral-to-medial direction to a pedestrian lower limb, and the knee shall be fully extended, to represent the load case specified in the STP.

In order to eliminate outliers, the dfbetas statistics defined in ISO/TS 18506 with the cut-off value of 0,3 were applied to identify overly influential observations in the collected biomechanical data.

A.2.3.3.2 Thigh

Table A.8 shows the collected biomechanical data for the thigh available from literature (see References [13], [14], 18] and [19]).

Potential overly influential PMHS test data (ID: 1-1, 1-4, 1-7, 1-8, 1-10, 1-13) were identified using the dfbetas statistics (Dfbetas > 0,3) as specified in ISO/TS 18506. IPFs with the identified data excluded one by one from the dataset were developed as shown in D.1.1. This resulted in the range of the injury values at the 50 % probability of injury being average ±4,0 %, compared to the range of confidence intervals of ±8,6 %. As the influence of the identified data was found to be not significant, all the PMHS data were used to develop the IPF.

Table A.8 — Biomechanical data for the thigh

Reference	ID	Age (YO)	Gender	Body mass [kg]	Stature [cm]	Flesh	Loading direction	Test type	BM [Nm]	Injury occurrence	Censoring	POI
Kerrigan et al. (2003)	1-1	55	M	85,0	172,7	Without	LM	D-3PB	632,5	Yes	RC	Yes
Kerrigan et al. (2003)	1-2	59	F	79,0	167,6	Without	LM	D-3PB	362,3	Yes	RC	No
Kerrigan et al. (2003)	1-3	54	F	50,0	162,6	Without	LM	D-3PB	340,0	Yes	RC	No
Kerrigan et al. (2003)	1-4	54	F	50,0	162,6	With	LM	D-3PB	376,7	Yes	EX	Yes
Kerrigan et al. (2004)	1-5	66	M	79,8	182,9	With	LM	D-3PB	548,0	Yes	EX	No
Kerrigan et al. (2004)	1-6	69	M	81,6	170,2	With	LM	D-3PB	568,0	Yes	EX	No
Kerrigan et al. (2004)	1-7	65	M	118,8	172,7	With	LM	D-3PB	640,0	Yes	EX	Yes
Kerrigan et al. (2004)	1-8	54	M	87,5	190,5	With	LM	D-3PB	424,0	Yes	EX	Yes
Kerrigan et al. (2004)	1-9	69	M	83,9	172,7	With	LM	D-3PB	488,0	Yes	EX	No
Kerrigan et al. (2004)	1-10	54	M	117,9	188,0	With	LM	D-3PB	685,0	Yes	EX	Yes
Funk et al. (2004)	1-11	67	M	64,0	188,0	Without	PA	D-3PB	355,0	Yes	RC	No
Funk et al. (2004)	1-12	59	M	108,0	182,9	Without	PA	D-3PB	593,0	Yes	RC	No
Funk et al. (2004)	1-13	40	M	70,0	180,3	Without	PA	D-3PB	605,0	Yes	RC	Yes
Funk et al. (2004)	1-14	55	M	64,0	167,6	Without	PA	D-3PB	363,0	Yes	RC	No
Funk et al. (2004)	1-15	70	M	73,0	167,6	Without	PA	D-3PB	359,0	Yes	RC	No
Funk et al. (2004)	1-16	69	M	92,0	162,6	Without	PA	D-3PB	460,0	Yes	RC	No
Funk et al. (2004)	1-17	51	M	124,0	188,0	Without	PA	D-3PB	599,0	Yes	RC	No
Funk et al. (2004)	1-18	66	M	95,0	182,9	Without	PA	D-3PB	373,0	Yes	RC	No
Funk et al. (2004)	1-19	67	M	64,0	188,0	Without	LM	D-3PB	435,0	Yes	RC	No
Funk et al. (2004)	1-20	59	M	108,0	182,9	Without	LM	D-3PB	497,0	Yes	RC	No
Funk et al. (2004)	1-21	40	M	70,0	180,3	Without	LM	D-3PB	528,0	Yes	RC	No
Funk et al. (2004)	1-22	55	M	64,0	167,6	Without	LM	D-3PB	389,0	Yes	RC	No
Funk et al. (2004)	1-23	70	M	73,0	167,6	Without	LM	D-3PB	356,0	Yes	RC	No
Funk et al. (2004)	1-24	69	M	92,0	162,6	Without	LM	D-3PB	419,0	Yes	RC	No
Funk et al. (2004)	1-25	51	M	124,0	188,0	Without	LM	D-3PB	543,0	Yes	RC	No
Ivarsson et al. (2009)	1-26	52	F	45,0	162,6	Without	AP	D-3PB	120,0	Yes	RC	No
Ivarsson et al. (2009)	1-27	52	F	45,0	162,6	Without	PA	D-3PB	147,0	Yes	RC	No
Ivarsson et al. (2009)	1-28	63	M	89,0	180,3	Without	PA	D-3PB	422,0	Yes	RC	No
Ivarsson et al. (2009)	1-29	62	F	90,7	170,2	Without	AP	D-3PB	364,0	Yes	RC	No
Ivarsson et al. (2009)	1-30	62	F	90,7	170,2	Without	AP	D-3PB	440,0	Yes	RC	No
Ivarsson et al. (2009)	1-31	45	M	68,1	175,3	Without	PA	D-3PB	238,0	Yes	RC	No
Ivarsson et al. (2009)	1-32	45	M	68,1	175,3	Without	AP	D-3PB	381,0	Yes	RC	No
Ivarsson et al. (2009)	1-33	39	M	79,4	184,0	Without	PA	D-3PB	433,0	Yes	RC	No
Ivarsson et al. (2009)	1-34	51	M	54,9	175,0	Without	AP	D-3PB	343,0	Yes	RC	No
Ivarsson et al. (2009)	1-35	57	F	108,9	165,0	Without	PA	D-3PB	193,0	Yes	RC	No

Key

YO	years-old
M	male
F	female
LM	lateral to medial
AP	anterior to posterior
PA	posterior to anterior
D-3PB	dynamic 3-point bending test
RC	right censored
EX	exact
POI	potential overly influential observation

A.2.3.3.3 Leg

Table A.9 shows the collected biomechanical data for the leg available from literature (see References [20], [13], [15] and [14]).

Potential overly influential PMHS test data (ID: 2-13, 2-18 through 2-23) were identified using the dfbetas statistics (Dfbetas > 0,3) as specified in ISO/TS 18506. IPFs with the identified data excluded one by one from the dataset were developed as shown in D.1.2. This resulted in the range of the injury values at the 50 % probability of injury being average ±5,3 %, compared to the range of confidence intervals of ±9,5 %. As the influence of the identified data was found to be not significant, all the PMHS data were used to develop the IPF.

Table A.9 — Biomechanical data for the leg

Reference	ID	Age (YO)	Gender	Body mass [kg]	Stature [cm]	Flesh	Loading direction	Test type	BM [Nm]	Injury occurrence	Censoring	POI
Nyquist et al. (1985)	2-1	54	M	68,0	182,0	With	LM	D-3PB	395,0	Yes	RC	No
Nyquist et al. (1985)	2-2	64	M	82,0	177,0	With	LM	D-3PB	287,0	Yes	RC	No
Nyquist et al. (1985)	2-3	58	M	73,0	174,0	With	LM	D-3PB	224,0	Yes	RC	No
Nyquist et al. (1985)	2-4	56	M	79,0	176,0	With	LM	D-3PB	237,0	Yes	RC	No
Nyquist et al. (1985)	2-5	57	M	99,0	178,0	With	LM	D-3PB	349,0	Yes	RC	No
Nyquist et al. (1985)	2-6	57	M	45,0	187,0	With	LM	D-3PB	264,0	Yes	RC	No
Nyquist et al. (1985)	2-7	57	M	84,0	178,0	With	LM	D-3PB	431,0	Yes	RC	No
Nyquist et al. (1985)	2-8	57	F	75,0	163,0	With	LM	D-3PB	254,0	Yes	RC	No
Nyquist et al. (1985)	2-9	51	F	68,0	163,0	With	LM	D-3PB	274,0	Yes	RC	No
Kerrigan et al. (2003a)	2-10	63	M	78,5	175,3	Without	LM	D-3PB	333,8	Yes	RC	No
Kerrigan et al. (2003a)	2-11	60	M	73,0	175,3	Without	LM	D-3PB	251,7	Yes	RC	No
Kerrigan et al. (2003a)	2-12	44	M	72,6	170,2	Without	LM	D-3PB	301,5	Yes	RC	No
Kerrigan et al. (2003a)	2-13	44	M	72,6	170,2	With	LM	D-3PB	416,5	Yes	EX	Yes
Kerrigan et al. (2003b)	2-14	54	M	88,0	190,5	With	LM	D-3PB	463,0	Yes	EX	No
Kerrigan et al. (2003b)	2-15	54	M	88,0	190,5	With	LM	D-3PB	485,0	Yes	EX	No
Kerrigan et al. (2003b)	2-16	68	M	51,0	165,1	With	LM	D-3PB	290,0	Yes	EX	No
Kerrigan et al. (2003b)	2-17	68	M	51,0	165,1	With	LM	D-3PB	309,0	Yes	EX	No
Kerrigan et al. (2003b)	2-18	65	F	60,0	172,7	With	LM	D-3PB	416,0	Yes	EX	Yes
Kerrigan et al. (2003b)	2-19	75	M	65,0	177,8	With	LM	D-3PB	306,0	Yes	EX	Yes
Kerrigan et al. (2004)	2-20	66	M	79,8	182,9	With	LM	D-3PB	277,0	Yes	EX	Yes
Kerrigan et al. (2004)	2-21	69	M	81,6	170,2	With	LM	D-3PB	433,0	Yes	EX	Yes
Kerrigan et al. (2004)	2-22	62	M	60,8	182,9	With	LM	D-3PB	259,0	Yes	EX	Yes
Kerrigan et al. (2004)	2-23	54	M	117,9	188,0	With	LM	D-3PB	482,0	Yes	EX	Yes

Key

M	male
F	female
LM	lateral to medial
D-3PB	dynamic 3-point bending test
RC	right censored
EX	exact
POI	potential overly influential observation

A.2.3.3.4 Knee

Table A.10 shows the collected biomechanical data for the MCL available from literature (see References [21], [22], 23] and [16]).

Potential overly influential PMHS test data (ID: 3-3, 3-9, 3-11, 3-21, 3-25) were identified using the dfbetas statistics (Dfbetas > 0,3) as specified in ISO/TS 18506. IPFs with the identified data excluded one by one from the dataset were developed as shown in D.1.3. This resulted in the range of the injury values at the 50 % probability of injury being average ±6,3 %, compared to the range of confidence intervals of ±41,7 %. As the influence of the identified data was found to be not significant, all the PMHS data were used to develop the IPF.

Table A.10 — Biomechanical data for the MCL

Reference	ID	Age (YO)	Gender	Body mass [kg]	Stature [cm]	Test type	VA [°]	Injury occurrence	Censoring	POI
Kajzer et al. (1997)	3-1	36	M	104	192	D-2BP	19,5	No	RC	No
Kajzer et al. (1997)	3-2	69	M	85	170	D-2BP	14,4	Yes	EX	No
Kajzer et al. (1997)	3-3	68	M	96	178	D-2BP	14,7	Yes	EX	Yes
Kajzer et al. (1997)	3-4	35	M	75	177	D-2BP	21,9	No	RC	No
Kajzer et al. (1997)	3-5	35	F	67	161	D-2BP	15,5	No	RC	No
Kajzer et al. (1997)	3-6	59	M	66	170	D-2BP	14,8	No	RC	No
Kajzer et al. (1997)	3-7	44	M	70	168	D-2BP	10,0	No	RC	No
Kajzer et al. (1997)	3-8	63	M	80	177	D-2BP	12,6	No	RC	No
Kajzer et al. (1997)	3-9	68	M	94	165	D-2BP	20,4	No	RC	Yes
Kajzer et al. (1999)	3-10	72	F	73	159	D-2BP	12,3	No	RC	No
Kajzer et al. (1999)	3-11	83	F	53	160	D-2BP	10,2	Yes	EX	Yes
Kajzer et al. (1999)	3-12	42	F	56	163	D-2BP	14,3	No	RC	No
Bose et al. (2004)	3-13	69	M	81,8	170,0	D-4PB	12,3	No	RC	No
Bose et al. (2004)	3-14	66	M	65,9	166,5	D-4PB	21,2	No	RC	No
Bose et al. (2004)	3-15	65	M	78,2	177,8	D-4PB	18,2	No	RC	No
Bose et al. (2004)	3-16	78	M	65,0	178,0	D-4PB	14,3	No	RC	No
Bose et al. (2004)	3-17	78	M	65,0	178,0	D-4PB	19,7	Yes	EX	No
Bose et al. (2004)	3-18	65	M	78,2	177,8	D-4PB	18,8	No	RC	No
Bose et al. (2004)	3-19	54	M	112,7	177,8	D-4PB	21,4	No	EX	No
Bose et al. (2004)	3-20	70	M	79,5	178,0	D-4PB	16,3	No	RC	No
Bose et al. (2008)	3-21	80	F	65,3	156,5	D-4PB	16,2	No	RC	Yes
Bose et al. (2008)	3-22	79	F	46,3	160,5	D-4PB	18,0	Yes	EX	No
Bose et al. (2008)	3-23	79	M	73,5	172,5	D-4PB	15,6	Yes	EX	No
Bose et al. (2008)	3-24	79	M	73,5	172,5	D-4PB	14,0	No	RC	No
Bose et al. (2008)	3-25	67	F	79,8	166,3	D-4PB	10,5	Yes	EX	Yes
Bose et al. (2008)	3-26	67	F	79,8	166,3	D-4PB	14,1	Yes	EX	No
Bose et al. (2008)	3-27	57	F	49,9	168,3	D-4PB	21,5	No	RC	No
Bose et al. (2008)	3-28	66	M	79,8	182,0	D-4PB	17,5	No	RC	No

Key

M	male
F	female
D-2PB	dynamic knee 2-point bending test
D-4PB	dynamic 4-point bending test
VA	knee valgus angle measured at maximum bending moment
RC	right censored
EX	exact
POI	potential overly influential observation

A.2.3.4 Results

A.2.3.4.1 Thigh

The human IPF for the thigh defines probability of femur shaft fracture to a pedestrian subjected to the specific load case represented by the STP as a function of maximum value of femur BM applied to human.

Figure A.18 presents the human IPF for the thigh. The injury probability function is shown in a solid line, with the 95 % confidence interval shown in dotted lines. The horizontal axis represents the maximum value of the femur BM applied to human, and the vertical axis represents the probability of injury.

For the thigh, the AIC scores for the three candidates of the distribution function (Weibull, Log-Normal and Log-logistic) were 98,8, 102,5 and 101,0, respectively. The Weibull distribution function showing the best fit to the data was used to determine the human IPF.

The human IPF for the thigh is given by Formula (A.5):

$$P = 1 - \exp\left\{-\left(\frac{x_{\text{human}}}{C_{\text{Scale}}}\right)^{C_{\text{Shape}}}\right\} \tag{A.5}$$

where

P is the injury probability for the femur shaft of human;

C_{Scale} is the parameter determined for the Weibull distribution for the human IPF for the femur shaft;

C_{Shape} is the parameter determined for the Weibull distribution for the human IPF for the femur shaft;

x_{human} is the thigh/femur BM for human in Nm.

The parameters needed to define the human IPF (C_{Scale} and C_{Shape}) for the function are described in Table A.11.

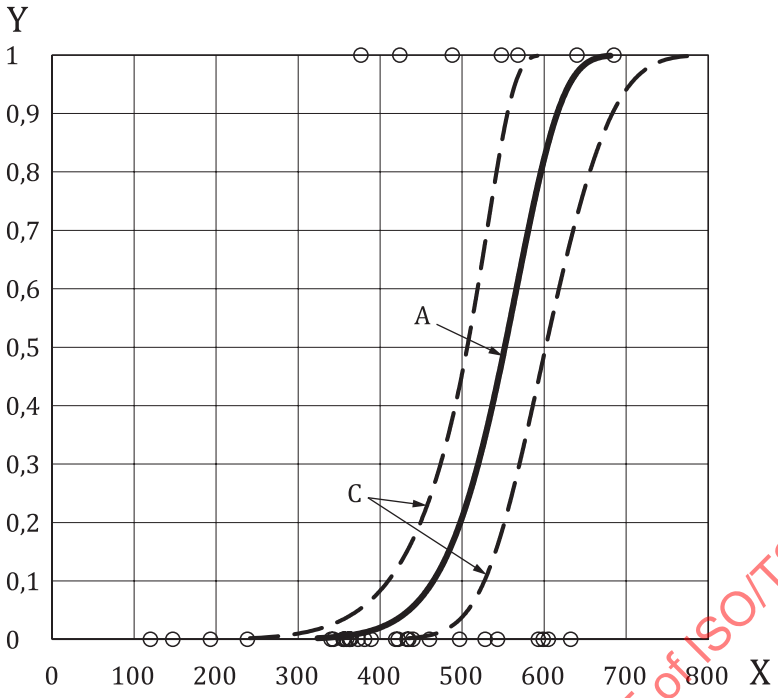

Key

X	human femur BM [Nm]
Y	probability of femur shaft fracture
A	human IPF for femur shaft in STP condition
C	95 % confidence interval
◯	observed data

Figure A.18 — Human IPF for the femur shaft

Table A.11 — Parameters of human IPF for the femur shaft

C_{Scale}	C_{Shape}
571	11,1

A.2.3.4.2 Leg

The human IPF for the leg defines probability of tibia shaft fracture to a pedestrian subjected to the specific load case represented by the STP as a function of maximum value of tibia BM applied to human.

Figure A.19 presents the human IPF for the leg. The injury probability function is shown in a solid line, with the 95 % confidence interval shown in dotted lines. The horizontal axis represents the maximum value of the tibia BM applied to human, and the vertical axis represents the probability of injury.

For the leg, the AIC scores for the three candidates of the distribution function (Weibull, Log-Normal and Log-logistic) were 137,2, 137,3 and 138,0, respectively. The Weibull distribution function showing the best fit to the data was used to determine the human IPF.

The human IPF for the leg is given by Formula (A.6):

$$P = 1 - \exp\left\{-\left(\frac{x_{human}}{C_{Scale}}\right)^{C_{Shape}}\right\} \quad \text{(A.6)}$$

where

P is the injury probability for the tibia shaft of human;

C_{Scale} is the parameter determined for the Weibull distribution for the human IPF for the tibia shaft ;

C_{Shape} is the parameter determined for the Weibull distribution for the human IPF for the tibia shaft ;

x_{human} is the leg/tibia BM for human in Nm.

The parameters needed to define the human IPF (C_{Scale} and C_{Shape}) for the function are described in Table A.12.

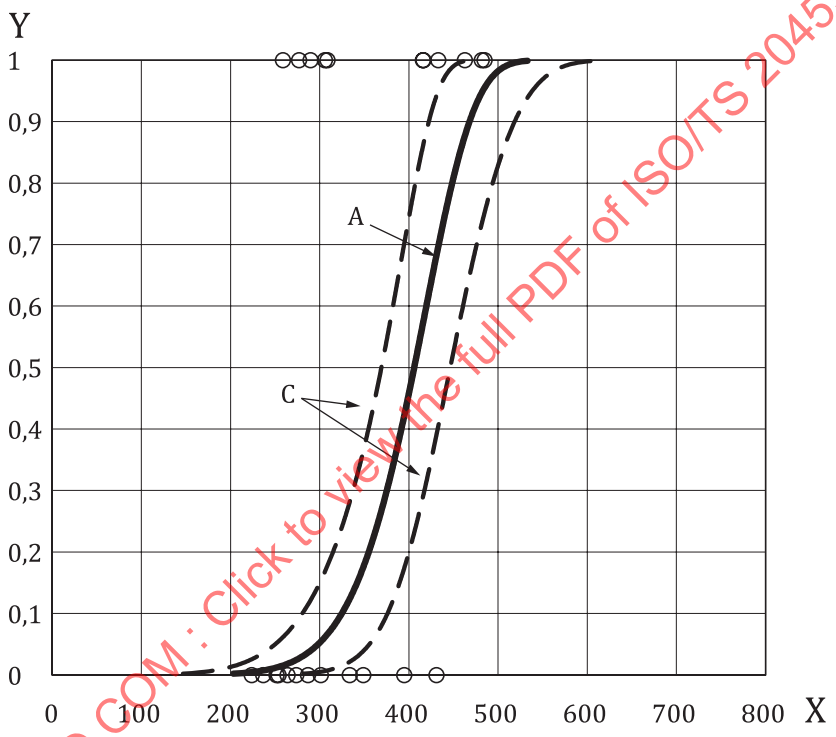

Key

X human tibia BM [Nm]
Y probability of tibia shaft fracture
A human IPF for tibia shaft in STP condition
C 95 % confidence interval
◯ observed data

Figure A.19 — Human IPF for the tibia shaft

Table A.12 — Parameters of human IPF for the tibia shaft

C_{Scale}	C_{Shape}
424	8,45

A.2.3.4.3 Knee

The human IPF for the knee defines probability of MCL failure to a pedestrian subjected to the specific load case represented by the STP as a function of maximum value of knee valgus angle applied to human.

Figure A.20 presents the human IPF for the knee. The injury probability function is shown in a solid line, with the 95 % confidence interval shown in dotted lines. The horizontal axis represents the maximum value of the knee valgus angle applied to human, and the vertical axis represents the probability of injury.

For the MCL, the AIC scores for the three candidates of the distribution function (Weibull, Log-Normal and Log-logistic) were 70,2, 69,7 and 70,0 respectively. The Log-Normal distribution function showing the best fit to the data was used to determine the human IPF.

The human IPF for the knee is given by Formula (A.7):

$$P = \frac{1}{C_\sigma \sqrt{2\pi}} \int_0^{x_{\text{human}}} \frac{1}{t} \exp\left\{ \frac{-\left(\ln t - C_\mu\right)^2}{2{C_\sigma}^2} \right\} \mathrm{d}t \tag{A.7}$$

where

P is the injury probability for the MCL of human;

C_μ is the parameter determined for the Log-Normal distribution for human IPFs for the MCL;

C_σ is the parameter determined for the Log-Normal distribution for human IPFs for the MCL;

x_{human} is the knee valgus angle for human in degrees.

The parameters needed to define the human IPF (C_μ and C_σ) for the function are described in Table A.13.

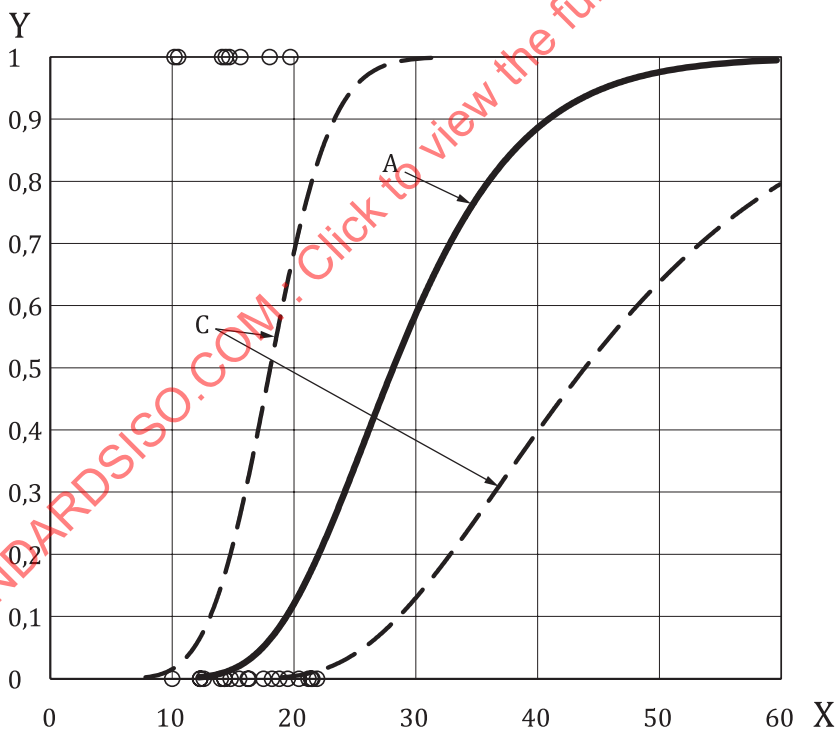

Key

X human knee valgus angle [°]

Y probability of MCL complete rupture

A human IPF for MCL complete rupture

C 95 % confidence interval

◯ observed data

Figure A.20 — Human IPF for the MCL complete rupture

Table A.13 — Parameters of human IPF for the MCL complete rupture

C_μ	C_σ
3,34	0,291

A.2.4 Development of TFs

A.2.4.1 General

The TFs for the thigh, leg and knee were determined by the correlation between the maximum values of injury metrics from aPLI models and HBMs. Based on the load case described in the STP, impacts were delivered by RCMs laterally at 11,1 m/s. Linear regression functions with the intercept set at zero were determined from the impact simulation results to define the TFs.

A.2.4.2 FE model

A.2.4.2.1 aPLI model

aPLI models well validated against aPLI hardware were used. Multiple aPLI models were used because impact simulations needed to be performed by some different institutions to ensure nonbiased distribution of the geometric and stiffness characteristics of the front-ends of the RCMs to represent a global fleet. Each of the aPLI models was validated against aPLI full assembly certification tests as defined in ISO/TS 20458. Validations were performed in two impact conditions defined: impact test at knee and below knee. The time history plots of all injury metrics up to 40 ms were compared between aPLI models and the test results. In order to evaluate the phase, magnitude and shape of the wave profiles of the time histories of the injury metrics using the ISO metric, all the test results used to determine the aPLI full assembly certification corridors as defined in ISO/TS 20458 were averaged and subjected to the comparison. The ISO metric as defined in ISO/TS 18571:2014 was calculated for each of the aPLI models. As shown in Table A.14, all of the ISO scores for overall rating were greater than 0,75 for all aPLI models and injury metrics.

All the time history plots for the aPLI models used in this analysis (aPLI model (A) through (F)) are shown in C.1.

Table A.14 — aPLI model (A through F) validation results indicated by the score of ISO metric by comparing time history plots of aPLI measurements with those of hardware in full-assembly impact test (at/below knee)

Measurements	Score of ISO metric											
	aPLI model (A)		aPLI model (B)		aPLI model (C)		aPLI model (D)		aPLI model (E)		aPLI model (F)	
	BK	AK	BK	AK	BK	AK	BK	AK	BK	AK	BK	AK
Femur-3	0,88	0,82	0,79	0,76	0,80	0,60	0,86	0,81	0,58	0,65	0,73	0,80
Femur-2	0,80	0,86	0,82	0,85	0,77	0,72	0,82	0,88	0,64	0,78	0,69	0,86
Femur-1	0,77	0,80	0,81	0,83	0,78	0,87	0,76	0,72	0,71	0,81	0,79	0,80
Tibia-1	0,86	0,85	0,81	0,79	0,85	0,81	0,84	0,84	0,72	0,83	0,82	0,87
Tibia-2	0,83	0,82	0,78	0,80	0,86	0,81	0,84	0,78	0,75	0,80	0,78	0,87
Tibia-3	0,76	0,79	0,73	0,77	0,78	0,79	0,75	0,73	0,67	0,77	0,72	0,84
Tibia-4	0,67	0,75	0,69	0,75	0,69	0,77	0,62	0,67	0,60	0,77	0,68	0,80
ACL	0,83	0,83	0,77	0,72	0,70	0,81	0,87	0,82	0,69	0,86	0,64	0,79
PCL	0,87	0,87	0,80	0,86	0,86	0,84	0,92	0,90	0,85	0,89	0,82	0,83
MCL	0,87	0,88	0,84	0,93	0,90	0,85	0,87	0,90	0,85	0,90	0,87	0,85
Overall rating	0,82		0,79		0,79		0,81		0,76		0,79	

Key

BK full-assembly certification test (below knee)

AK full-assembly certification test (at knee)

A.2.4.2.2 HBM

The following four human full-body models representing anthropometry of a 50th percentile of adult male are used:

— HBM-A, the model developed by References [7], [8] and [9];

— HBM-B, the model developed by Reference [31];

— HBM-C, a modified version of the model developed by Reference [32];

— HBM-D, a modified version of the model developed by Reference [33].

HBM-A and HBM-B are used by the aPLI TG Japanese delegation, and the HBM-C is used by the German delegation. HBM-D was developed by a global consortium, and it is used among French, the United States and Japanese delegations. The results of HBM impact simulations were shared at the aPLI TG and combined to define an HBM dataset.

Similar modelling approaches were used to develop the lower limb of these four HBMs. The femur, the tibia and the fibula are divided into an outer cortical layer and an inner trabecular layer modelled with a shell and/or solid elements. Each of the four major knee ligaments (ACL, PCL, MCL and LCL) are modelled using solid or shell elements, and the meniscus are modelled using solid elements. The flesh surrounding the bony structure is modelled with solid elements and the skin covering the flesh is modelled using shell elements. More details can be found in the corresponding references described above.

In order to confirm that the impact response data obtained from these four HBMs are reasonably distributed, without any significant bias for specific HBM(s), lateral impact simulations at 11,1 m/s were conducted using each of the four HBMs at the bumper angles of 0° and ±40°. Impacts were delivered from twenty SCMs to represent a number of different loading conditions. Cars on the global market are represented by cars in the following four categories:

— Japanese sedan (J sedan);

— low-bumper Japanese SUV (J low-bumper SUV);

— high-bumper Japanese SUV (J high-bumper SUV);

— American SUV and pick-up truck (US SUV).

The SCMs represent a car front-end with discrete rigid components for BLE, grille, BP and SP that translate in the opposite direction of car travel with specified non-linear spring characteristics, except for BLE of J sedan, J low-bumper SUV and part of J high-bumper SUV modelled using shell elements. A translational degree of freedom in the vertical direction was also added specifically to the BLE of part of J high-bumper SUV and US SUV. Such specific modelling strategy is needed because BLE of such cars tends to be subjected to a combined longitudinal and vertical force due to contact with the lower limb of a pedestrian. SP is modelled only for low-bumper cars. Grille is not modelled for J sedan, J low-bumper SUV and part of J high-bumper SUV with a relatively small vertical dimension of the grille. In contrast, the grille of part of J high-bumper SUV is modelled using two rigid components due to a relatively large vertical dimension and a stiffness distribution of the grille. The combinations of the geometric and stiffness characteristics of the SCMs representing the four categories were determined through a collaborative effort of international experts at the aPLI TG in such a way that peak values of aPLI injury metrics are widely and evenly distributed as much as possible, resulting in 6 J sedan SCMs, 6 J low-bumper SUV SCMs, 4 J high-bumper SUV SCMs and 4 US SUV SCMs (20 SCMs in total).

The schematics of the geometric and stiffness characteristics of the twenty SCMs are presented in Figure A.21 through Figure A.24 and Figure A.25 through Figure A.30, respectively. The tabulated data of the geometric and stiffness characteristics of the SCMs are provided at:

https://standards.iso.org/iso/ts/20459/ed-1/en

Figure A.31 through Figure A.39 show plots of peak values of injury metrics (thigh BM, MCL elongation and leg BM) predicted by the four HBMs against lower bumper reference line height of each of the twenty SCMs. The experts of the aPLI TG recognized that the data are reasonably distributed, considering a large variability of human impact responses. It was decided by the aPLI TG members to use these four models to develop TFs for the aPLI.

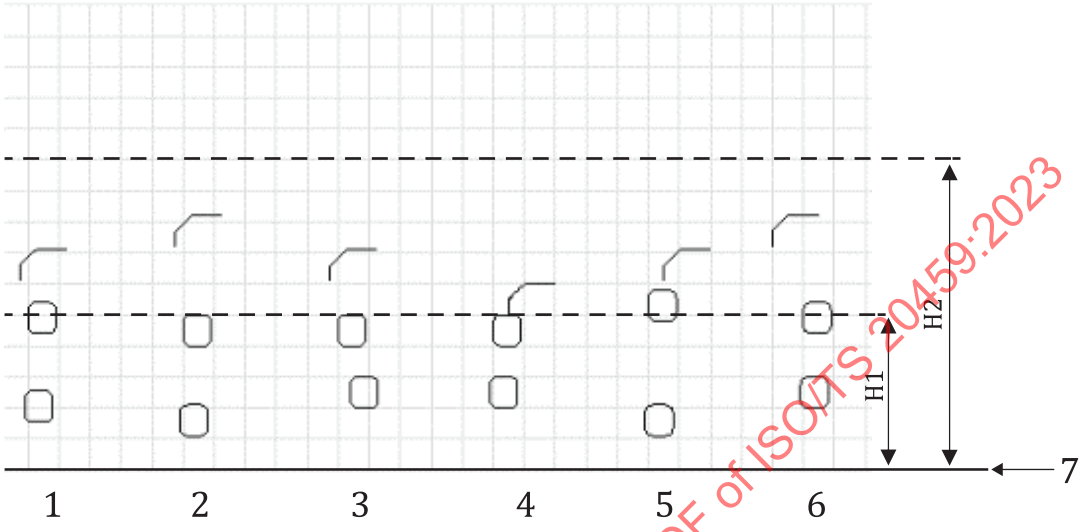

Key

1 J-SDN-02
2 J-SDN-06
3 J-SDN-07
4 J-SDN-11
5 J-SDN-13
6 J-SDN-16
7 ground level
H1 500 mm
H2 1 000 mm

NOTE Grid size is 100 mm × 100 mm.

Figure A.21 — Geometry of the six J sedan SCMs

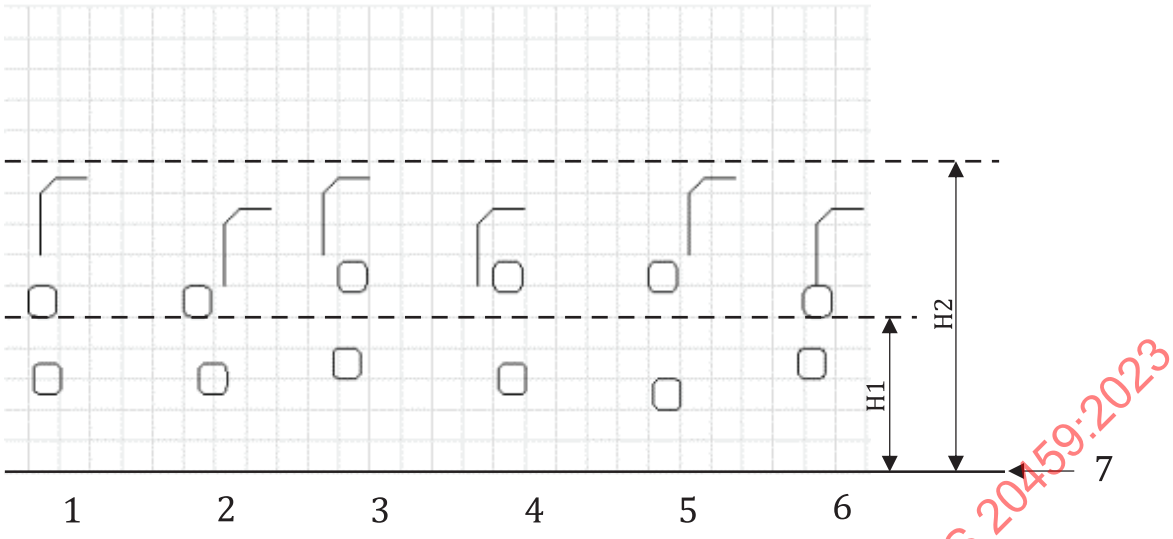

Key

1 J-LoBP-SUV-02
2 J-LoBP-SUV-04
3 J-LoBP-SUV-05
4 J-LoBP-SUV-09
5 J-LoBP-SUV-13
6 J-LoBP-SUV-15
7 ground level
H1 500 mm
H2 1 000 mm

NOTE Grid size is 100 mm × 100 mm.

Figure A.22 — Geometry of the six J low-bumper SUV SCMs

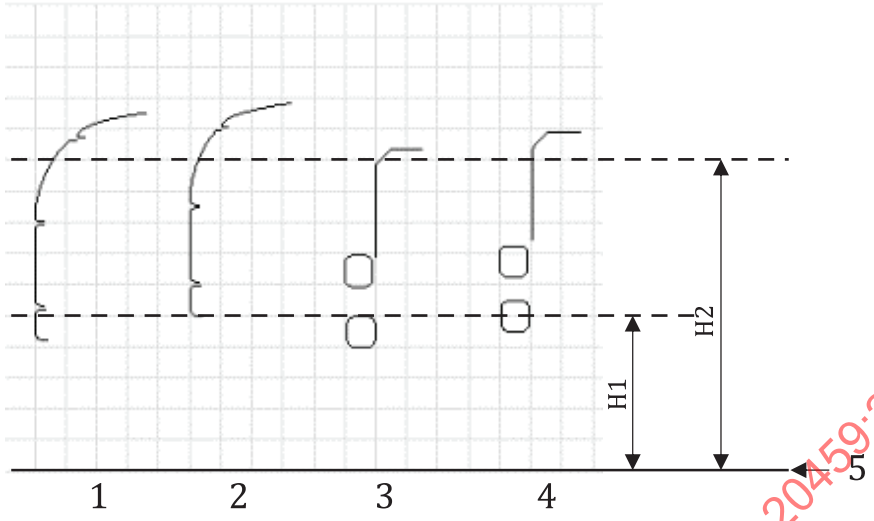

Key

1 J-HiBP-01aH
2 J-HiBP-01cH
3 J-HiBP-02
4 J-HiBP-04
5 ground level
H1 500 mm
H2 1 000 mm

NOTE Grid size is 100 mm × 100 mm.

Figure A.23 — Geometry of the four J high-bumper SUV SCMs

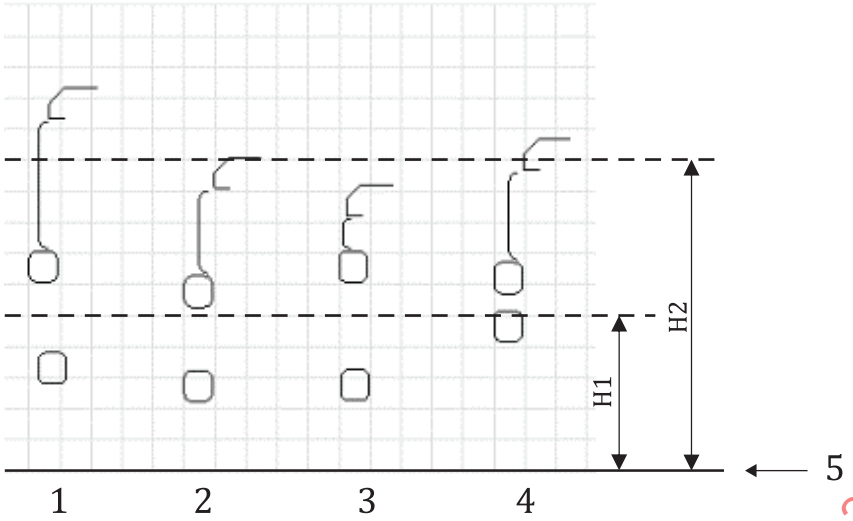

Key

1 US-LSUV-02S
2 US-SUV-01S
3 US-SUV-02H
4 US-TR-02S
5 ground level
H1 500 mm
H2 1 000 mm

NOTE Grid size is 100 mm × 100 mm.

Figure A.24 — Geometry of four US SUV SCMs

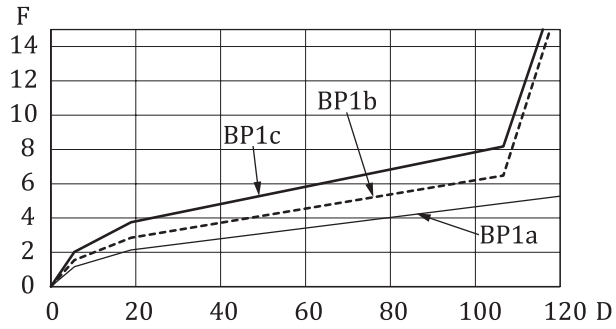

a) Bumper

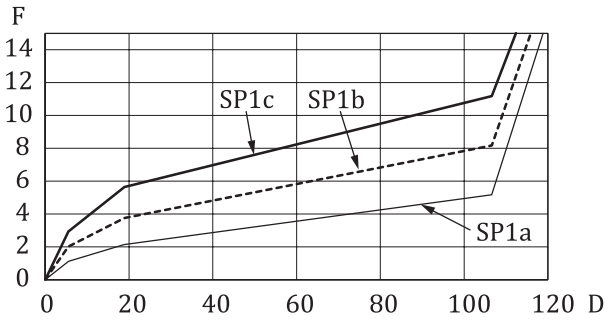

b) Spoiler

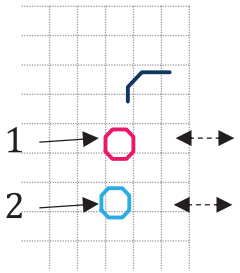

c) Direction of deflection

Key

1	bumper
2	spoiler
D	deflection [mm]
F	force [kN]
BP1a	bumper stiffness curve specified for JSDN02 and JSDN11
BP1b	bumper stiffness curve specified for JSDN06 and JSDN13
BP1c	bumper stiffness curve specified for JSDN07 and JSDN16
SP1a	spoiler stiffness curve specified for JSDN07, JSDN13 and JSDN16
SP1b	spoiler SP stiffness curve specified for JSDN02 and JSDN11
SP1c	spoiler SP stiffness curve specified for JSDN06

Figure A.25 — Force-deflection curves specified for the bumper and spoiler of the six J sedan SCMs

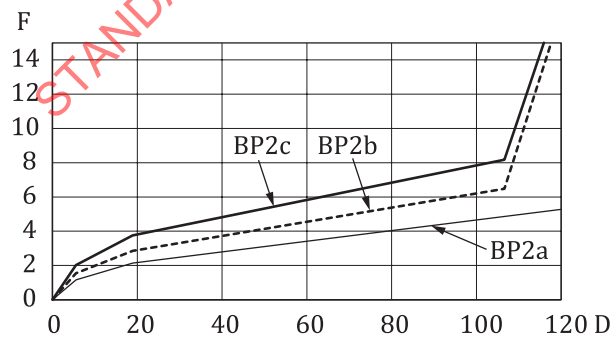

a) Bumper stiffness

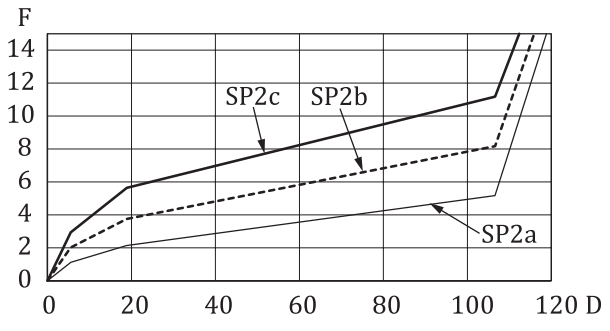

b) Spoiler stiffness

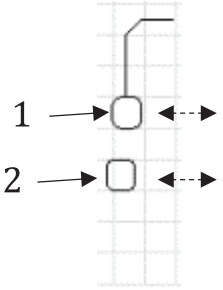

c) Direction of deflection

Key

1	bumper
2	spoiler
D	deflection [mm]
F	force [kN]
BP2a	bumper stiffness curve specified for J-LoBP-SUV-02
BP2b	bumper stiffness curve specified for JLoBP-SUV-04, J-LoBP-SUV-05, J-LoBP-SUV-13 and J-LoBP-SUV-15
BP2c	bumper stiffness curve specified for J-LoBP-SUV-09
SP2a	spoiler stiffness curve specified for J-LoBP-SUV-04 and J-LoBP-SUV-13
SP2b	spoiler stiffness curve specified for J-LoBP-SUV-02 and J-LoBP-SUV-05
SP2c	spoiler stiffness curve specified for J-LoBP-SUV-09 and J-LoBP-SUV-15

Figure A.26 — Force-deflection curves specified for the bumper and spoiler of the six J low-bumper SUV SCMs

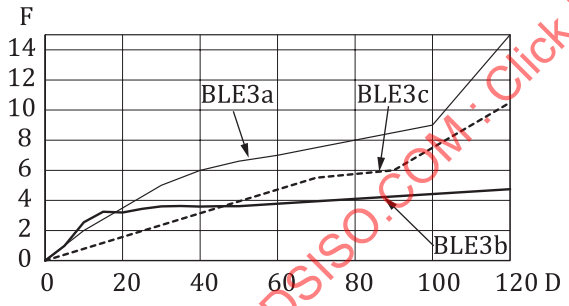

a) BLE stiffness (y)

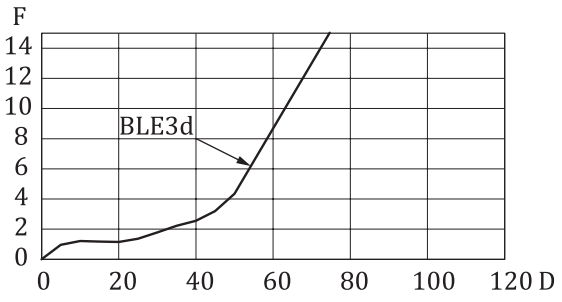

b) BLE stiffness (z)

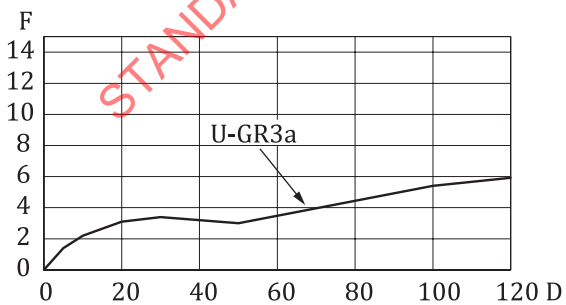

c) Upper grill stiffness

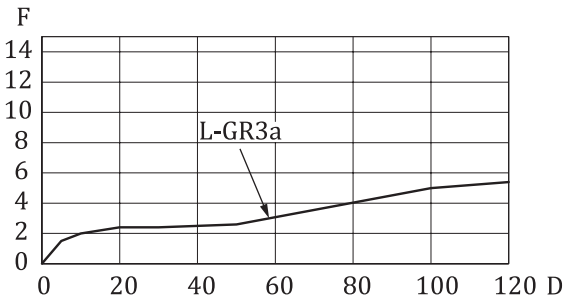

d) Lower grill stiffness

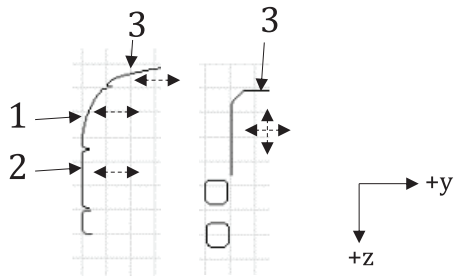

e) Direction of deflection

Key

1	upper grille
2	lower grille
3	BLE
D	deflection [mm]
F	force [kN]
BLE3a/UGR3a/ LGR3a	stiffness curve specified for J-HiBP-01aH and JHiBP01cH
BLE3b/BLE3d	stiffness curve specified for J-HiBP-02
BLE3c	stiffness curve specified for J-HiBP-04
(y)	stiffness curve specified for y-direction
(z)	stiffness curve specified for z-direction

Figure A.27 — Force-deflection curves specified for the BLE and grille of the four J high-bumper SUV SCMs

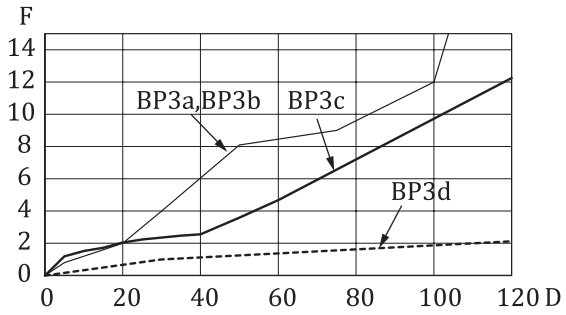

a) Bumper stiffness

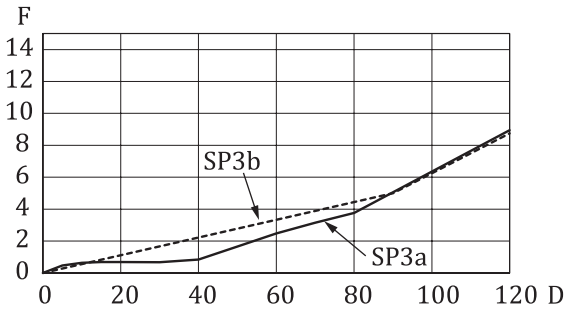

b) Spoiler stiffness

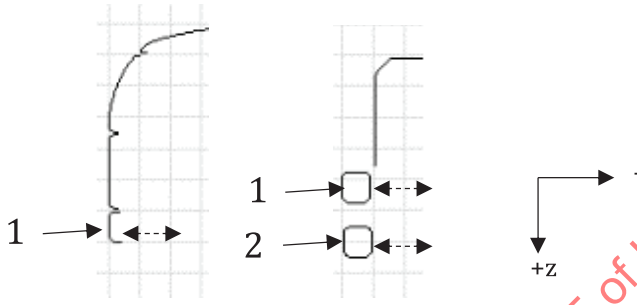

c) Direction of deflection

Key

1	bumper
2	spoiler
D	deflection [mm]
F	force [kN]
BP3a/SP3a	stiffness curve specified for J-HiBP-01aH and JHiBP-01cH
BP3b/SP3a	stiffness curve specified for J-HiBP-02
BP3c/SP3b	stiffness curve specified for J-HiBP-04

Figure A.28 — Force-deflection curves specified for the bumper and spoiler of the four J high-bumper SUV SCMs

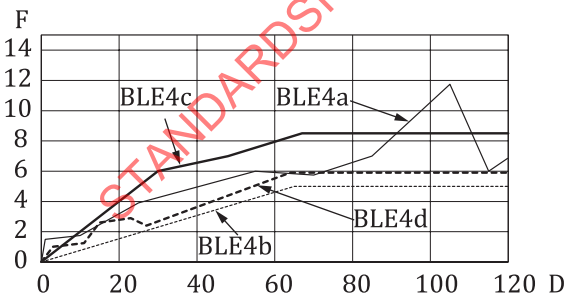

a) BLE stiffness (y)

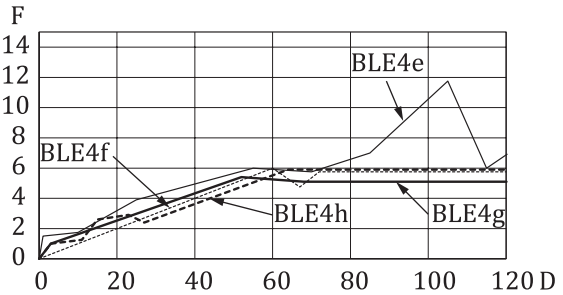

b) BLE stiffness (z)

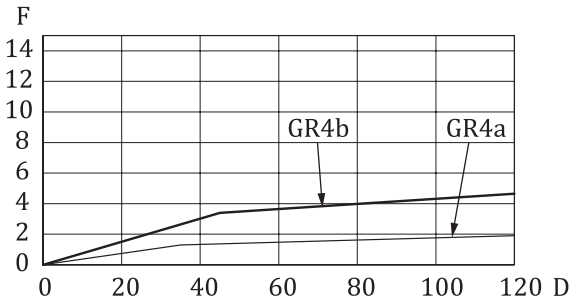

c) Grill stiffness

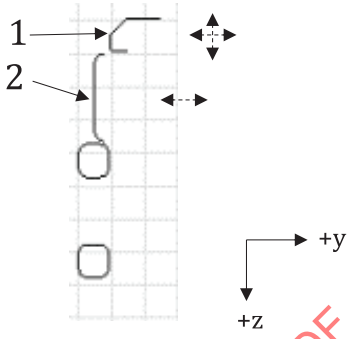

d) Direction of deflection

Key

1	BLE
2	grille
F	force [kN]
D	deflection [mm]
BLE4a/BLE4e/GF4a	stiffness curve specified for US-LSUV-02S
BLE4b/BLE4f/GF4a	stiffness curve specified for US-SUV-01S
BLE4c/BLE4g/GF4b	stiffness curve specified for US-SUV-02H
BLE4d/BLE4h/GR4a	stiffness curve specified for US-TR-02S
(y)	stiffness curve specified for y-direction
(z)	stiffness curve specified for z-direction

Figure A.29 — Force-deflection curves specified for the BLE and grille of the four US SUV SCMs

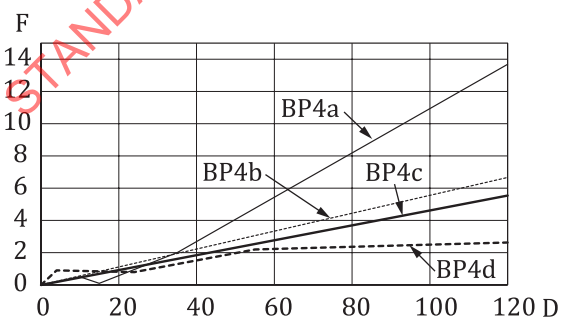

a) Bumper stiffness

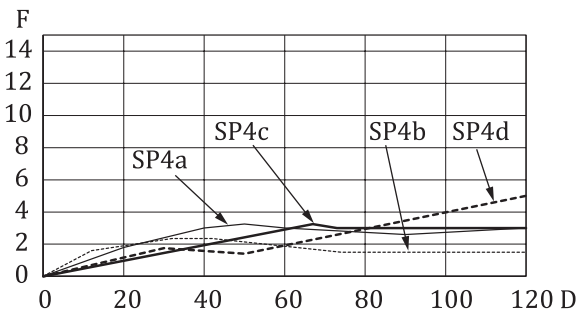

b) Spoiler stiffness

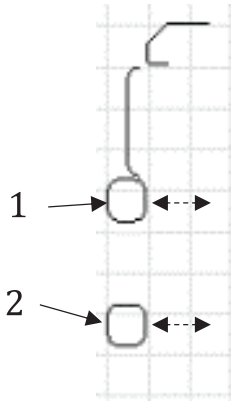

c) Direction of deflection

Key

1	bumper
2	spoiler
F	force [kN]
D	deflection [mm]
BP4a/SP4a	stiffness curve specified for US-LSUV-02S
BP4b/SP4b	stiffness curve specified for US-SUV-01S
BP4c/SP4c	stiffness curve specified for US-SUV-02H
BP4d/SP4d	stiffness curve specified for US-TR-02S

Figure A.30 — Force-deflection curves specified for the bumper and spoiler of the four US SUV SCMs

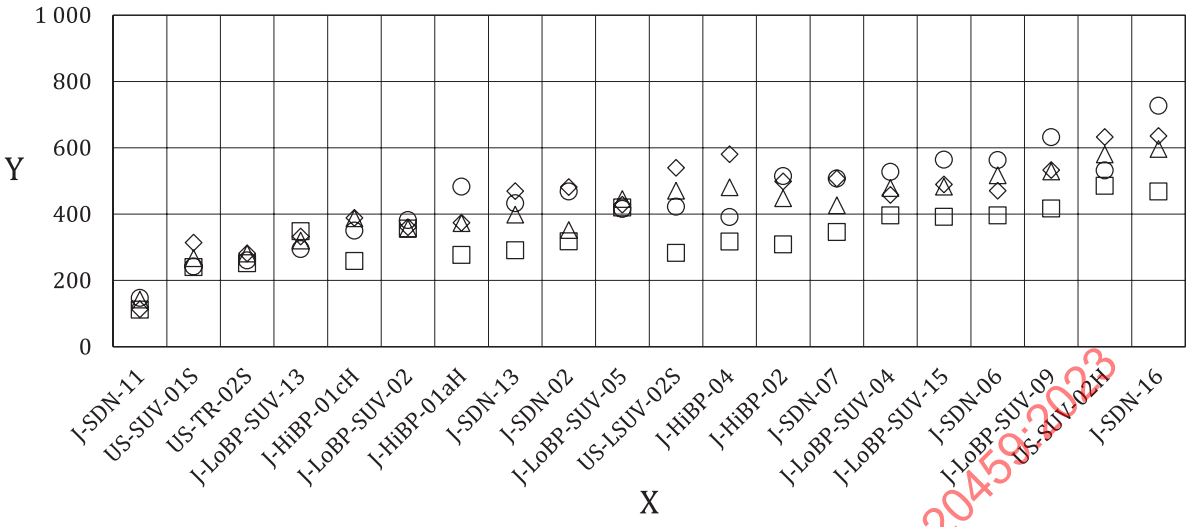

Key

X twenty SCMs in ascending order of the average peak value of the thigh BM of the four HBMs from left to right

Y peak value of the femur BM of the four HBMs [Nm]

○ HBM-A

△ HBM-B

□ HBM-C

◇ HBM-D

Figure A.31 — Peak values of the thigh BM predicted by the four HBMs in impacts with the twenty SCMs (bumper angle: 0°)

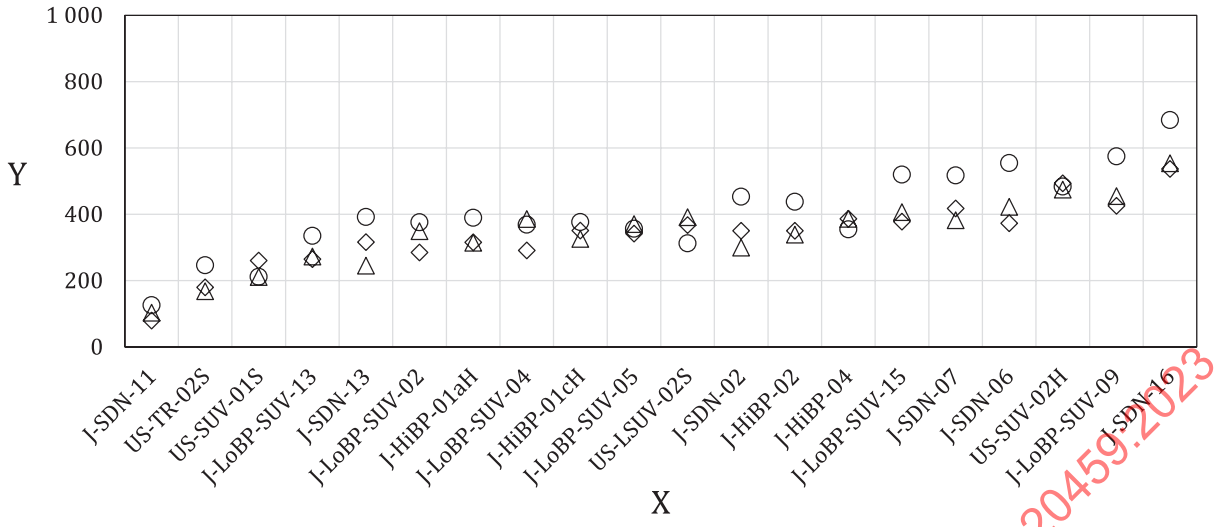

Key

X twenty SCMs in ascending order of the average peak value of the thigh BM of the four HBMs from left to right

Y peak value of the femur BM of the four HBMs [Nm]

○ HBM-A

△ HBM-B

□ HBM-C

◇ HBM-D

Figure A.32 — Peak values of the thigh BM predicted by the four HBMs in impacts with the twenty SCMs (bumper angle: +40°)

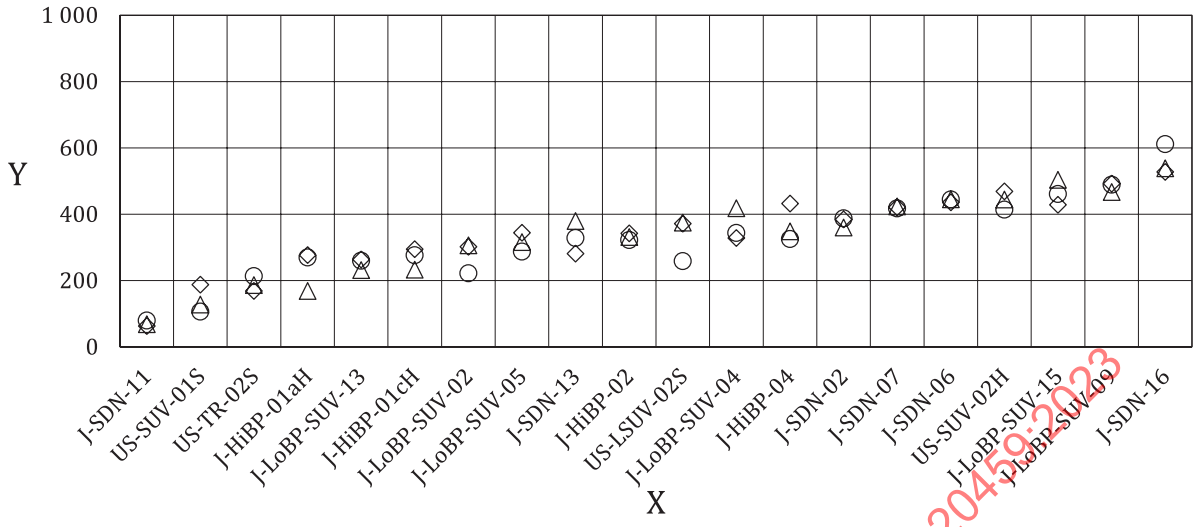

Key

X twenty SCMs in ascending order of the average peak value of the thigh BM of the four HBMs from left to right

Y peak value of the femur BM of the four HBMs [Nm]

○ HBM-A

△ HBM-B

□ HBM-C

◇ HBM-D

Figure A.33 — Peak values of the thigh BM predicted by the four HBMs in impacts with the twenty SCMs (bumper angle: -40°)

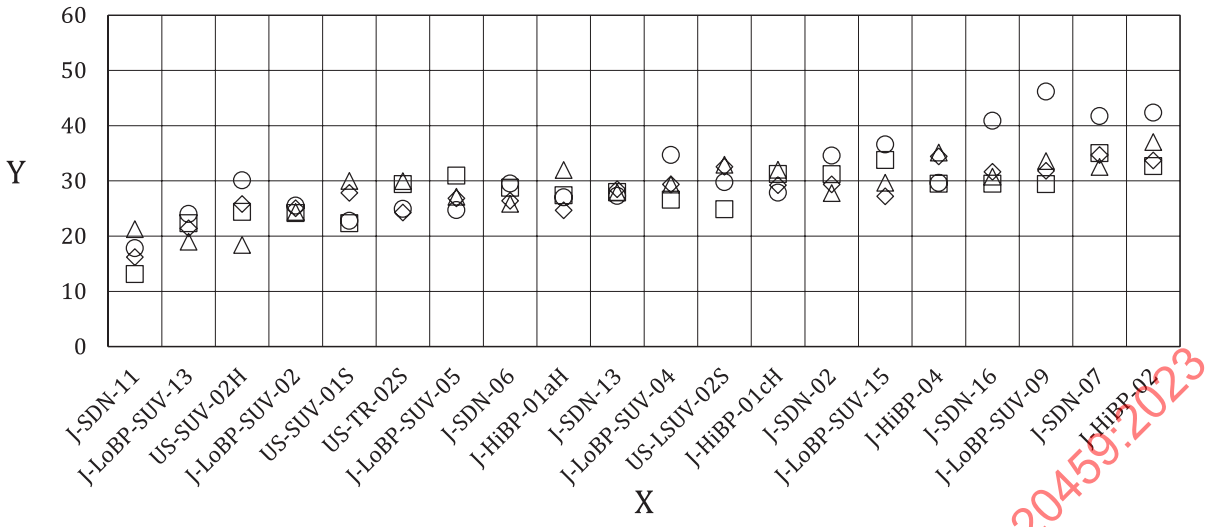

Key

X twenty SCMs in ascending order of average peak value of the knee valgus angle of the four HBMs from left to right

Y peak value of the knee valgus angle of four HBMs [°]

○ HBM-A

△ HBM-B

□ HBM-C

◇ HBM-D

Figure A.34 — Peak values of the knee valgus angle predicted by the four HBMs in impacts with the twenty SCMs (bumper angle: 0°)

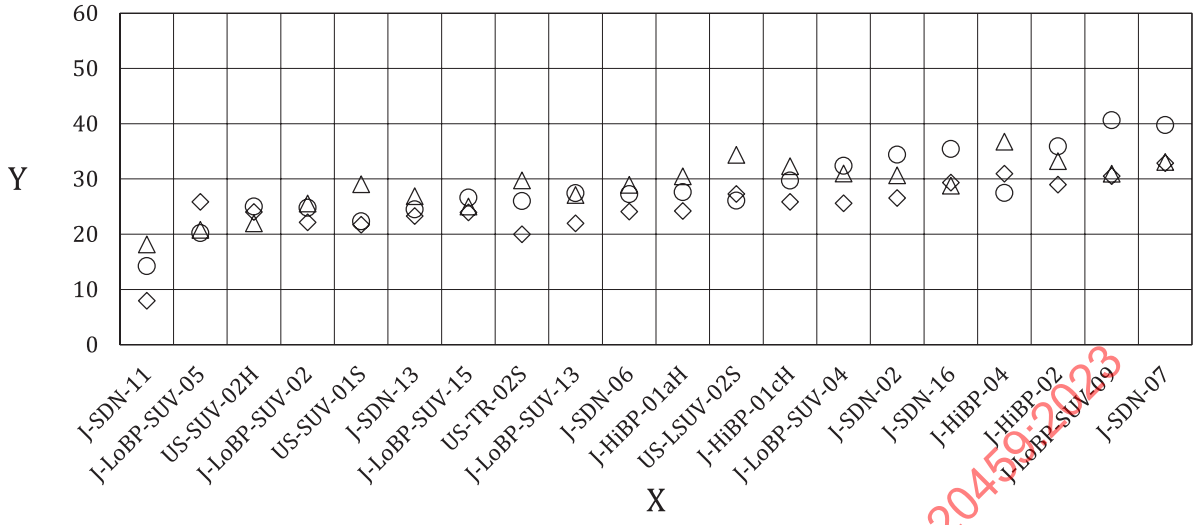

Key

X	twenty SCMs in ascending order of average peak value of the knee valgus angle of the four HBMs from left to right
Y	peak value of the knee valgus angle of four HBMs [°]
○	HBM-A
△	HBM-B
□	HBM-C
◇	HBM-D

Figure A.35 — Peak values of the knee valgus angle predicted by the four HBMs in impacts with the twenty SCMs (bumper angle: +40°)

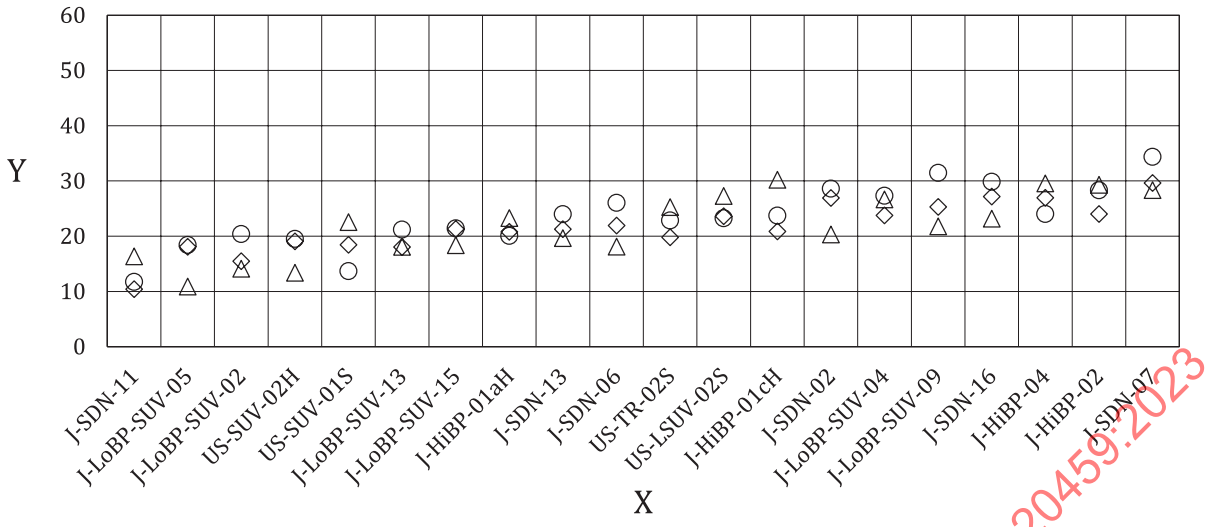

Key

X twenty SCMs in ascending order of average peak value of the knee valgus angle of the four HBMs from left to right

Y peak value of the knee valgus angle of four HBMs [°]

○ HBM-A

△ HBM-B

□ HBM-C

◇ HBM-D

Figure A.36 — Peak values of the knee valgus angle predicted by the four HBMs in impacts with the twenty SCMs (bumper angle: -40°)

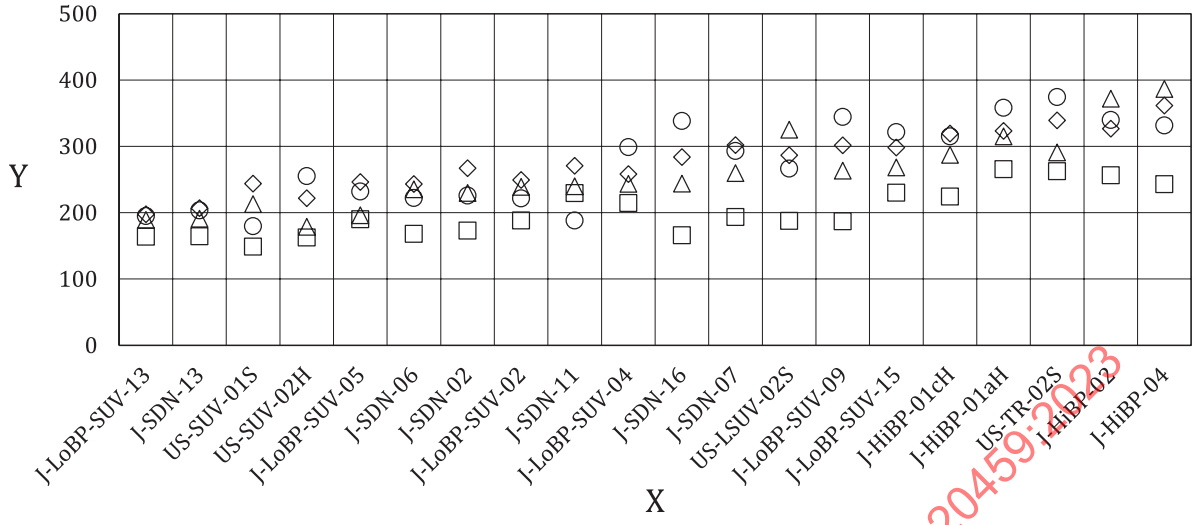

Key

X	twenty SCMs in ascending order of the average peak value of the tibia BM of the four HBMs from left to right
Y	peak value of the tibia BM of the four HBMs [Nm]
○	HBM-A
△	HBM-B
□	HBM-C
◇	HBM-D

Figure A.37 — Peak values of the leg BM predicted by the four HBMs in impacts with the twenty SCMs (bumper angle: 0°)

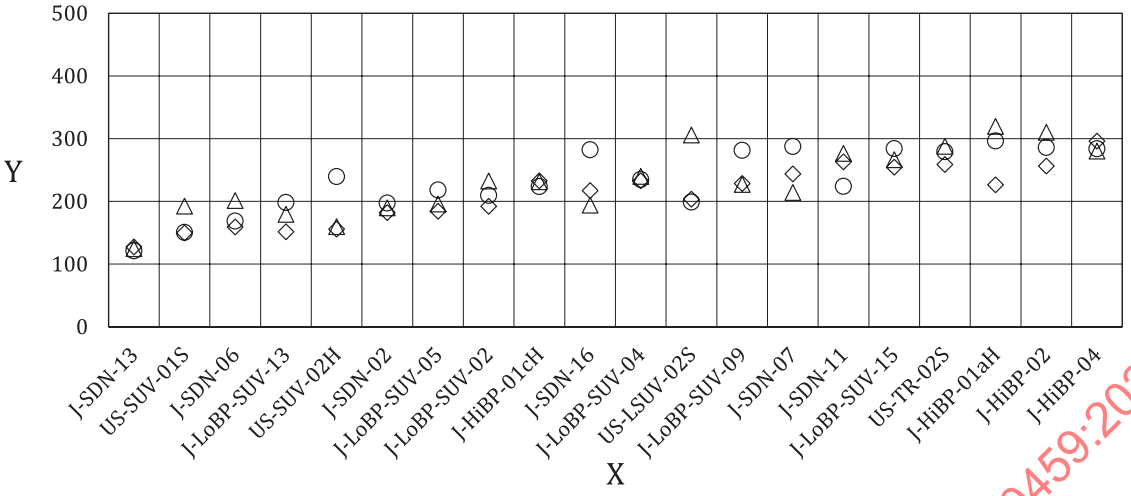

Key

X twenty SCMs in ascending order of the average peak value of the tibia BM of the four HBMs from left to right

Y peak value of the tibia BM of the four HBMs [Nm]

○ HBM-A

△ HBM-B

□ HBM-C

◇ HBM-D

Figure A.38 — Peak values of the leg BM predicted by the four HBMs in impacts with the twenty SCMs (bumper angle: +40°)

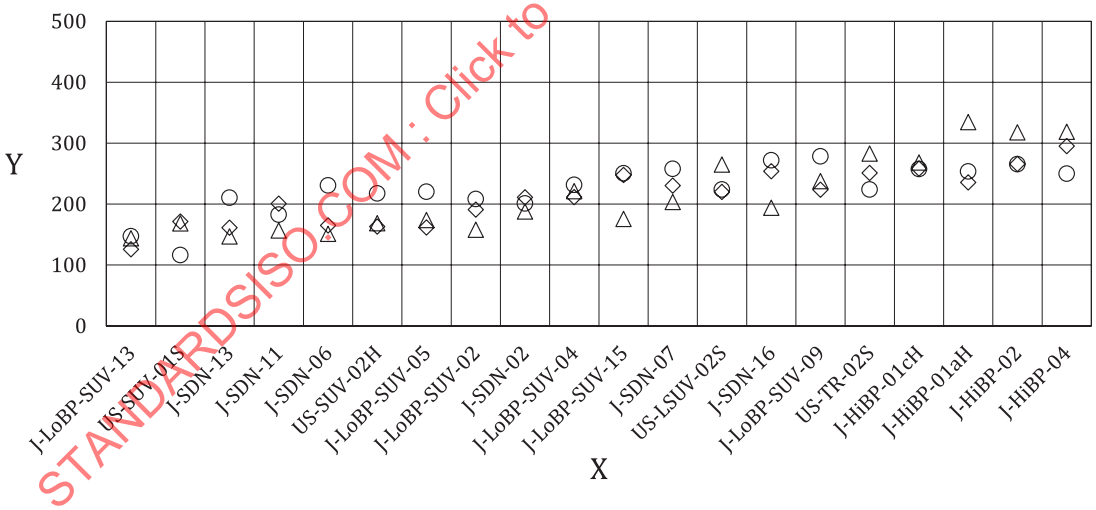

Key

X twenty SCMs in ascending order of the average peak value of the tibia BM of the four HBMs from left to right

Y peak value of the tibia BM of the four HBMs [Nm]

○ HBM-A

△ HBM-B

□ HBM-C

◇ HBM-D

Figure A.39 — Peak values of the leg BM predicted by the four HBMs in impacts with the twenty SCMs (bumper angle: -40°)

A.2.4.2.3 RCM

In order to represent a variety of different combinations of geometric and stiffness characteristics of car front-ends in the global fleet, 94 different RCMs developed by different car manufacturers were used in this analysis. The RCMs were classified into nine categories (Type A-1 through Type F-1 (lower bumper reference line (LBRL) height is less than 425 mm) and Type D-2 through Type F-2 (LBRL height is 425 mm or more) as shown in Table A.15, based on the realistic combination of the BLE height and the LBRL height, as defined in References [1] and [2] to ensure that the distribution of the characteristics is not biased.

Only limited information about each of the RCMs was available due to confidentiality. Table A.16 presents the BLE height and the LBRL height of the 94 RCMs.

Table A.15 — Nine categories of the RCM based on the combination of the BLE height and LBRL height

Category of RCM	BLE height	LBRL height	Number of RCM
Type A-1	Less than 600 mm	less than 425 mm	2
Type B-1	600 mm or more but less than 700 mm	less than 425 mm	13
Type C-1	700 mm or more but less than 800 mm	less than 425 mm	26
Type D-1	800 mm or more but less than 900 mm	less than 425 mm	20
Type E-1	900 mm or more but less than 1 000 mm	less than 425 mm	18
Type F-1	1 000 mm or more	less than 425 mm	9
Type D-2	800 mm or more but less than 900 mm	425 mm or more	1
Type E-2	900 mm or more but less than 1 000 mm	425 mm or more	1
Type F-2	1 000 mm or more	425 mm or more	4
NOTE aPLI TG did not identify any cars with a combination of the BLE height being less than 800 mm and LBRL height being 425 mm or more.			

Table A.16 — BLE height and LBRL height information of 94 RCMs

RCM ID	BLEH [mm]	LBRLH [mm]	RCM ID	BLEH [mm]	LBRLH [mm]	RCM ID	BLEH [mm]	LBRLH [mm]	RCM ID	BLEH [mm]	LBRLH [mm]
RCM1-1	585	199	RCM2-1	817	219	RCM3-1	712	219	RCM4-1	610	163
RCM1-2	894	245	RCM2-2	880	195	RCM3-2	690	221	RCM4-2	827	222
RCM1-3	993	254	RCM2-3	998	201	RCM3-3	747	222	RCM4-3	789	210
RCM1-4	756	244	RCM2-4	731	214	RCM3-4	704	213	RCM4-4	815	229
RCM1-5	696	244	RCM2-5	1 048	382	RCM3-5	556	185	RCM4-5	857	257
RCM1-6	777	241	RCM2-6	600	195	RCM3-6	937	382	RCM4-6	755	195
RCM1-7	947	217	RCM2-7	680	203	RCM3-7	937	356	RCM4-7	887	298
RCM1-8	720	225	RCM2-8	793	250	RCM3-8	929	344	RCM4-8	936	263
RCM1-9	885	256	RCM2-9	880	314	RCM3-9	821	267	RCM4-9	1 093	265
RCM1-10	935	234	RCM2-10	918	302	RCM3-10	926	400	RCM4-10	1 139	363
RCM1-11	724	240	RCM2-11	1 054	332	RCM3-11	850	250	RCM4-11	1 127	311
RCM1-12	657	222	RCM2-12	949	348	RCM3-12	669	214	RCM4-12	1 141	420
RCM1-13	714	233	RCM2-13	852	308	RCM3-13	632	200	RCM4-13	720	220
RCM1-14	763	222	RCM2-14	832	314	RCM3-14	784	218	RCM4-14	812	246
Key BLEH BLE height LBRLH LBRL height											

Table A.16 *(continued)*

RCM ID	BLEH [mm]	LBRLH [mm]	RCM ID	BLEH [mm]	LBRLH [mm]	RCM ID	BLEH [mm]	LBRLH [mm]	RCM ID	BLEH [mm]	LBRLH [mm]
RCM1-15	774	236	RCM2-15	762	224	RCM3-15	962	395	RCM4-15	920	368
RCM1-16	781	237	RCM2-16	746	228	RCM3-16	874	255	RCM4-16	937	297
RCM1-17	868	304	RCM2-17	604	189	RCM3-17	654,4	209,8	RCM4-17	1 049	323
RCM1-18	903	418	RCM2-18	618	205	RCM3-18	853,5	557,9	RCM4-18	1 105	470
RCM1-19	867	273	RCM2-19	703	214	RCM3-19	811,2	270,9	RCM4-19	1 179	470
RCM1-20	921	297	RCM2-20	826	226	RCM3-20	600	205,5	RCM4-20	756	222
			RCM2-21	1 013	226	RCM3-21	730	227	RCM4-21	740	234
			RCM2-22	1 107	485	RCM3-22	678	185	RCM4-22	736	239
			RCM2-23	752	205	RCM3-23	895	313	RCM4-23	732	227
			RCM2-24	911	322	RCM3-24	995	495			
			RCM2-25	1 076	457	RCM3-25	937	311			
			RCM2-26	1 030	330						

Key

BLEH BLE height

LBRLH LBRL height

A.2.4.3 Impact simulation

A.2.4.3.1 Simulation matrix

Due to limitation in the HBM available for a car manufacturer who developed specific RCMs, it was impossible to perform impact simulations in a full factorial simulation matrix. Table A.17 through Table A.20 show the matrix of impact simulations used to develop TFs. Three impact locations (BP-centre, BP-right, BP-left) were used for each of the combinations of the RCM, HBM and aPLI model.

Table A.17 — Matrix of impact simulations (HBM-A)

S-ID	RCM ID	IL	HBM	aPLI model	S-ID	RCM ID	IL	HBM	aPLI model
S1-1-C	RCM1-1	BC	HBM-A	aPLI model (A)	S1-1-L	RCM1-1	BL	HBM-A	aPLI model (A)
S1-2-C	RCM1-2	BC	HBM-A	aPLI model (A)	S1-2-L	RCM1-2	BL	HBM-A	aPLI model (A)
S1-3-C	RCM1-3	BC	HBM-A	aPLI model (A)	S1-3-L	RCM1-3	BL	HBM-A	aPLI model (A)
S1-4-C	RCM1-4	BC	HBM-A	aPLI model (A)	S1-4-L	RCM1-4	BL	HBM-A	aPLI model (A)
S1-5-C	RCM1-5	BC	HBM-A	aPLI model (A)	S1-5-L	RCM1-5	BL	HBM-A	aPLI model (A)
S1-6-C	RCM1-6	BC	HBM-A	aPLI model (A)	S1-6-L	RCM1-6	BL	HBM-A	aPLI model (A)

Key

S-ID simulation ID

IL impact location

BC lateral centre of the bumper test area defined in References [1] and [2]

BR right end of the bumper test area defined in References [1] and [2]

BL left end of the bumper test area defined in References [1] and [2]

Table A.17 *(continued)*

S-ID	RCM ID	IL	HBM	aPLI model	S-ID	RCM ID	IL	HBM	aPLI model
S1-7-C	RCM1-7	BC	HBM-A	aPLI model (A)	S1-7-L	RCM1-7	BL	HBM-A	aPLI model (A)
S1-8-C	RCM1-8	BC	HBM-A	aPLI model (A)	S1-8-L	RCM1-8	BL	HBM-A	aPLI model (A)
S1-9-C	RCM1-9	BC	HBM-A	aPLI model (A)	S1-9-L	RCM1-9	BL	HBM-A	aPLI model (A)
S1-10-C	RCM1-10	BC	HBM-A	aPLI model (A)	S1-10-L	RCM1-10	BL	HBM-A	aPLI model (A)
S1-11-C	RCM1-11	BC	HBM-A	aPLI model (A)	S1-11-L	RCM1-11	BL	HBM-A	aPLI model (A)
S1-12-C	RCM1-12	BC	HBM-A	aPLI model (A)	S1-12-L	RCM1-12	BL	HBM-A	aPLI model (A)
S1-13-C	RCM1-13	BC	HBM-A	aPLI model (A)	S1-13-L	RCM1-13	BL	HBM-A	aPLI model (A)
S1-14-C	RCM1-14	BC	HBM-A	aPLI model (A)	S1-14-L	RCM1-14	BL	HBM-A	aPLI model (A)
S1-15-C	RCM1-15	BC	HBM-A	aPLI model (A)	S1-15-L	RCM1-15	BL	HBM-A	aPLI model (A)
S1-16-C	RCM1-16	BC	HBM-A	aPLI model (A)	S1-16-L	RCM1-16	BL	HBM-A	aPLI model (A)
S1-17-C	RCM1-17	BC	HBM-A	aPLI model (A)	S1-17-L	RCM1-17	BL	HBM-A	aPLI model (A)
S1-18-C	RCM1-18	BC	HBM-A	aPLI model (A)	S1-18-L	RCM1-18	BL	HBM-A	aPLI model (A)
S1-19-C	RCM1-19	BC	HBM-A	aPLI model (A)	S1-19-L	RCM1-19	BL	HBM-A	aPLI model (A)
S1-20-C	RCM1-20	BC	HBM-A	aPLI model (A)	S1-20-L	RCM1-20	BL	HBM-A	aPLI model (A)
S1-1-R	RCM1-1	BR	HBM-A	aPLI model (A)					
S1-2-R	RCM1-2	BR	HBM-A	aPLI model (A)					
S1-3-R	RCM1-3	BR	HBM-A	aPLI model (A)					
S1-4-R	RCM1-4	BR	HBM-A	aPLI model (A)					
S1-5-R	RCM1-5	BR	HBM-A	aPLI model (A)					
S1-6-R	RCM1-6	BR	HBM-A	aPLI model (A)					
S1-7-R	RCM1-7	BR	HBM-A	aPLI model (A)					
S1-8-R	RCM1-8	BR	HBM-A	aPLI model (A)					

Key

S-ID	simulation ID
IL	impact location
BC	lateral centre of the bumper test area defined in References [1] and [2]
BR	right end of the bumper test area defined in References [1] and [2]
BL	left end of the bumper test area defined in References [1] and [2]

Table A.17 *(continued)*

S-ID	RCM ID	IL	HBM	aPLI model	S-ID	RCM ID	IL	HBM	aPLI model
S1-9-R	RCM1-9	BR	HBM-A	aPLI model (A)					
S1-10-R	RCM1-10	BR	HBM-A	aPLI model (A)					
S1-11-R	RCM1-11	BR	HBM-A	aPLI model (A)					
S1-12-R	RCM1-12	BR	HBM-A	aPLI model (A)					
S1-13-R	RCM1-13	BR	HBM-A	aPLI model (A)					
S1-14-R	RCM1-14	BR	HBM-A	aPLI model (A)					
S1-15-R	RCM1-15	BR	HBM-A	aPLI model (A)					
S1-16-R	RCM1-16	BR	HBM-A	aPLI model (A)					
S1-17-R	RCM1-17	BR	HBM-A	aPLI model (A)					
S1-18-R	RCM1-18	BR	HBM-A	aPLI model (A)					
S1-19-R	RCM1-19	BR	HBM-A	aPLI model (A)					
S1-20-R	RCM1-20	BR	HBM-A	aPLI model (A)					

Key

S-ID simulation ID

IL impact location

BC lateral centre of the bumper test area defined in References [1] and [2]

BR right end of the bumper test area defined in References [1] and [2]

BL left end of the bumper test area defined in References [1] and [2]

Table A.18 — Matrix of impact simulations (HBM-B)

S-ID	RCM ID	IL	HBM	aPLI model	S-ID	RCM ID	IL	HBM	aPLI model
S2-1-C	RCM2-1	BC	HBM-B	aPLI model (B)	S2-1-L	RCM2-1	BL	HBM-B	aPLI model (B)
S2-2-C	RCM2-2	BC	HBM-B	aPLI model (B)	S2-2-L	RCM2-2	BL	HBM-B	aPLI model (B)
S2-3-C	RCM2-3	BC	HBM-B	aPLI model (B)	S2-3-L	RCM2-3	BL	HBM-B	aPLI model (B)
S2-4-C	RCM2-4	BC	HBM-B	aPLI model (B)	S2-4-L	RCM2-4	BL	HBM-B	aPLI model (B)
S2-5-C	RCM2-5	BC	HBM-B	aPLI model (B)	S2-5-L	RCM2-5	BL	HBM-B	aPLI model (B)
S2-6-C	RCM2-6	BC	HBM-B	aPLI model (E)	S2-6-L	RCM2-6	BL	HBM-B	aPLI model (E)
S2-7-C	RCM2-7	BC	HBM-B	aPLI model (E)	S2-7-L	RCM2-7	BL	HBM-B	aPLI model (E)
S2-8-C	RCM2-8	BC	HBM-B	aPLI model (E)	S2-8-L	RCM2-8	BL	HBM-B	aPLI model (E)

Key

S-ID simulation ID

IL impact location

BC lateral centre of the bumper test area defined in References [1] and [2]

BR right end of the bumper test area defined in References [1] and [2]

BL left end of the bumper test area defined in References [1] and [2]

Table A.18 *(continued)*

S-ID	RCM ID	IL	HBM	aPLI model	S-ID	RCM ID	IL	HBM	aPLI model
S2-9-C	RCM2-9	BC	HBM-B	aPLI model (E)	S2-9-L	RCM2-9	BL	HBM-B	aPLI model (E)
S2-10-C	RCM2-10	BC	HBM-B	aPLI model (E)	S2-10-L	RCM2-10	BL	HBM-B	aPLI model (E)
S2-11-C	RCM2-11	BC	HBM-B	aPLI model (E)	S2-11-L	RCM2-11	BL	HBM-B	aPLI model (E)
S2-12-C	RCM2-12	BC	HBM-B	aPLI model (E)	S2-12-L	RCM2-12	BL	HBM-B	aPLI model (E)
S2-13-C	RCM2-13	BC	HBM-B	aPLI model (E)	S2-13-L	RCM2-13	BL	HBM-B	aPLI model (E)
S2-14-C	RCM2-14	BC	HBM-B	aPLI model (E)	S2-14-L	RCM2-14	BL	HBM-B	aPLI model (E)
S2-15-C	RCM2-15	BC	HBM-B	aPLI model (E)	S2-15-L	RCM2-15	BL	HBM-B	aPLI model (E)
S2-16-C	RCM2-16	BC	HBM-B	aPLI model (E)	S2-16-L	RCM2-16	BL	HBM-B	aPLI model (E)
S2-17-C	RCM2-17	BC	HBM-B	aPLI model (E)	S2-17-L	RCM2-17	BL	HBM-B	aPLI model (E)
S2-18-C	RCM2-18	BC	HBM-B	aPLI model (C)	S2-18-L	RCM2-18	BL	HBM-B	aPLI model (C)
S2-19-C	RCM2-19	BC	HBM-B	aPLI model (C)	S2-19-L	RCM2-19	BL	HBM-B	aPLI model (C)
S2-20-C	RCM2-20	BC	HBM-B	aPLI model (C)	S2-20-L	RCM2-20	BL	HBM-B	aPLI model (C)
S2-21-C	RCM2-21	BC	HBM-B	aPLI model (C)	S2-21-L	RCM2-21	BL	HBM-B	aPLI model (C)
S2-22-C	RCM2-22	BC	HBM-B	aPLI model (C)	S2-22-L	RCM2-22	BL	HBM-B	aPLI model (C)
S2-23-C	RCM2-23	BC	HBM-B	aPLI model (D)	S2-23-L	RCM2-23	BL	HBM-B	aPLI model (D)
S2-24-C	RCM2-24	BC	HBM-B	aPLI model (D)	S2-24-L	RCM2-24	BL	HBM-B	aPLI model (D)
S2-25-C	RCM2-25	BC	HBM-B	aPLI model (D)	S2-25-L	RCM2-25	BL	HBM-B	aPLI model (D)
S2-26-C	RCM2-26	BC	HBM-B	aPLI model (D)	S2-26-L	RCM2-26	BL	HBM-B	aPLI model (D)
S2-1-R	RCM2-1	BR	HBM-B	aPLI model (B)					
S2-2-R	RCM2-2	BR	HBM-B	aPLI model (B)					
S2-3-R	RCM2-3	BR	HBM-B	aPLI model (B)					
S2-4-R	RCM2-4	BR	HBM-B	aPLI model (B)					
S2-5-R	RCM2-5	BR	HBM-B	aPLI model (B)					
S2-6-R	RCM2-6	BR	HBM-B	aPLI model (E)					
S2-7-R	RCM2-7	BR	HBM-B	aPLI model (E)					
S2-8-R	RCM2-8	BR	HBM-B	aPLI model (E)					
S2-9-R	RCM2-9	BR	HBM-B	aPLI model (E)					
S2-10-R	RCM2-10	BR	HBM-B	aPLI model (E)					
S2-11-R	RCM2-11	BR	HBM-B	aPLI model (E)					
S2-12-R	RCM2-12	BR	HBM-B	aPLI model (E)					
S2-13-R	RCM2-13	BR	HBM-B	aPLI model (E)					
S2-14-R	RCM2-14	BR	HBM-B	aPLI model (E)					
S2-15-R	RCM2-15	BR	HBM-B	aPLI model (E)					
S2-16-R	RCM2-16	BR	HBM-B	aPLI model (E)					
S2-17-R	RCM2-17	BR	HBM-B	aPLI model (E)					
S2-18-R	RCM2-18	BR	HBM-B	aPLI model (C)					
S2-19-R	RCM2-19	BR	HBM-B	aPLI model (C)					
S2-20-R	RCM2-20	BR	HBM-B	aPLI model (C)					

Key

S-ID simulation ID

IL impact location

BC lateral centre of the bumper test area defined in References [1] and [2]

BR right end of the bumper test area defined in References [1] and [2]

BL left end of the bumper test area defined in References [1] and [2]

Table A.18 *(continued)*

S-ID	RCM ID	IL	HBM	aPLI model	S-ID	RCM ID	IL	HBM	aPLI model
S2-21-R	RCM2-21	BR	HBM-B	aPLI model (C)					
S2-22-R	RCM2-22	BR	HBM-B	aPLI model (C)					
S2-23-R	RCM2-23	BR	HBM-B	aPLI model (D)					
S2-24-R	RCM2-24	BR	HBM-B	aPLI model (D)					
S2-25-R	RCM2-25	BR	HBM-B	aPLI model (D)					
S2-26-R	RCM2-26	BR	HBM-B	aPLI model (D)					

Key

S-ID simulation ID

IL impact location

BC lateral centre of the bumper test area defined in References [1] and [2]

BR right end of the bumper test area defined in References [1] and [2]

BL left end of the bumper test area defined in References [1] and [2]

Table A.19 — Matrix of impact simulations (HBM-C)

S-ID	RCM ID	IL	HBM	aPLI model	S-ID	RCM ID	IL	HBM	aPLI model
S3-1-C	RCM3-1	BC	HBM-C	aPLI model (F)	S3-1-L	RCM3-1	BR	HBM-C	aPLI model (F)
S3-2-C	RCM3-2	BC	HBM-C	aPLI model (F)	S3-2-L	RCM3-2	BR	HBM-C	aPLI model (F)
S3-3-C	RCM3-3	BC	HBM-C	aPLI model (F)	S3-3-L	RCM3-3	BR	HBM-C	aPLI model (F)
S3-4-C	RCM3-4	BC	HBM-C	aPLI model (F)	S3-4-L	RCM3-4	BR	HBM-C	aPLI model (F)
S3-5-C	RCM3-5	BC	HBM-C	aPLI model (F)	S3-5-L	RCM3-5	BR	HBM-C	aPLI model (F)
S3-6-C	RCM3-6	BC	HBM-C	aPLI model (F)	S3-6-L	RCM3-6	BR	HBM-C	aPLI model (F)
S3-7-C	RCM3-7	BC	HBM-C	aPLI model (F)	S3-7-L	RCM3-7	BR	HBM-C	aPLI model (F)
S3-8-C	RCM3-8	BC	HBM-C	aPLI model (F)	S3-8-L	RCM3-8	BR	HBM-C	aPLI model (F)
S3-9-C	RCM3-9	BC	HBM-C	aPLI model (F)	S3-9-L	RCM3-9	BR	HBM-C	aPLI model (F)
S3-10-C	RCM3-10	BC	HBM-C	aPLI model (F)	S3-10-L	RCM3-10	BR	HBM-C	aPLI model (F)
S3-11-C	RCM3-11	BC	HBM-C	aPLI model (F)	S3-11-L	RCM3-11	BR	HBM-C	aPLI model (F)
S3-12-C	RCM3-12	BC	HBM-C	aPLI model (F)	S3-12-L	RCM3-12	BR	HBM-C	aPLI model (F)
S3-13-C	RCM3-13	BC	HBM-C	aPLI model (F)	S3-13-L	RCM3-13	BR	HBM-C	aPLI model (F)

Key

S-ID simulation ID

IL impact location

BC lateral centre of the bumper test area defined in References [1] and [2]

BR right end of the bumper test area defined in References [1] and [2]

BL left end of the bumper test area defined in References [1] and [2]

Table A.19 *(continued)*

S-ID	RCM ID	IL	HBM	aPLI model	S-ID	RCM ID	IL	HBM	aPLI model
S3-14-C	RCM3-14	BC	HBM-C	aPLI model (F)	S3-14-L	RCM3-14	BR	HBM-C	aPLI model (F)
S3-15-C	RCM3-15	BC	HBM-C	aPLI model (F)	S3-15-L	RCM3-15	BR	HBM-C	aPLI model (F)
S3-16-C	RCM3-16	BC	HBM-C	aPLI model (F)	S3-16-L	RCM3-16	BR	HBM-C	aPLI model (F)
S3-17-C	RCM3-17	BC	HBM-C	aPLI model (E)	S3-17-L	RCM3-17	BR	HBM-C	aPLI model (E)
S3-18-C	RCM3-18	BC	HBM-C	aPLI model (E)	S3-18-L	RCM3-18	BR	HBM-C	aPLI model (E)
S3-19-C	RCM3-19	BC	HBM-C	aPLI model (E)	S3-19-L	RCM3-19	BR	HBM-C	aPLI model (E)
S3-20-C	RCM3-20	BC	HBM-C	aPLI model (E)	S3-20-L	RCM3-20	BR	HBM-C	aPLI model (E)
S3-21-C	RCM3-21	BC	HBM-C	aPLI model (E)	S3-21-L	RCM3-21	BR	HBM-C	aPLI model (E)
S3-22-C	RCM3-22	BC	HBM-C	aPLI model (E)	S3-22-L	RCM3-22	BR	HBM-C	aPLI model (E)
S3-23-C	RCM3-23	BC	HBM-C	aPLI model (E)	S3-23-L	RCM3-23	BR	HBM-C	aPLI model (E)
S3-24-C	RCM3-24	BC	HBM-C	aPLI model (E)	S3-24-L	RCM3-24	BR	HBM-C	aPLI model (E)
S3-25-C	RCM3-25	BC	HBM-C	aPLI model (E)	S3-25-L	RCM3-25	BR	HBM-C	aPLI model (E)
S3-1-R	RCM3-1	BR	HBM-C	aPLI model (F)					
S3-2-R	RCM3-2	BR	HBM-C	aPLI model (F)					
S3-3-R	RCM3-3	BR	HBM-C	aPLI model (F)					
S3-4-R	RCM3-4	BR	HBM-C	aPLI model (F)					
S3-5-R	RCM3-5	BR	HBM-C	aPLI model (F)					
S3-6-R	RCM3-6	BR	HBM-C	aPLI model (F)					
S3-7-R	RCM3-7	BR	HBM-C	aPLI model (F)					
S3-8-R	RCM3-8	BR	HBM-C	aPLI model (F)					
S3-9-R	RCM3-9	BR	HBM-C	aPLI model (F)					
S3-10-R	RCM3-10	BR	HBM-C	aPLI model (F)					

Key

S-ID simulation ID

IL impact location

BC lateral centre of the bumper test area defined in References [1] and [2]

BR right end of the bumper test area defined in References [1] and [2]

BL left end of the bumper test area defined in References [1] and [2]

Table A.19 *(continued)*

S-ID	RCM ID	IL	HBM	aPLI model	S-ID	RCM ID	IL	HBM	aPLI model
S3-11-R	RCM3-11	BR	HBM-C	aPLI model (F)					
S3-12-R	RCM3-12	BR	HBM-C	aPLI model (F)					
S3-13-R	RCM3-13	BR	HBM-C	aPLI model (F)					
S3-14-R	RCM3-14	BR	HBM-C	aPLI model (F)					
S3-15-R	RCM3-15	BR	HBM-C	aPLI model (F)					
S3-16-R	RCM3-16	BR	HBM-C	aPLI model (F)					
S3-17-R	RCM3-17	BR	HBM-C	aPLI model (E)					
S3-18-R	RCM3-18	BR	HBM-C	aPLI model (E)					
S3-19-R	RCM3-19	BR	HBM-C	aPLI model (E)					
S3-20-R	RCM3-20	BR	HBM-C	aPLI model (E)					
S3-21-R	RCM3-21	BR	HBM-C	aPLI model (E)					
S3-22-R	RCM3-22	BR	HBM-C	aPLI model (E)					
S3-23-R	RCM3-23	BR	HBM-C	aPLI model (E)					
S3-24-R	RCM3-24	BR	HBM-C	aPLI model (E)					
S3-25-R	RCM3-25	BR	HBM-C	aPLI model (E)					

Key

S-ID	simulation ID
IL	impact location
BC	lateral centre of the bumper test area defined in References [1] and [2]
BR	right end of the bumper test area defined in References [1] and [2]
BL	left end of the bumper test area defined in References [1] and [2]

Table A.20 — Matrix of impact simulations (HBM-D)

S-ID	RCM ID	IL	HBM	aPLI model	S-ID	RCM ID	IL	HBM	aPLI model
S4-1-C	RCM4-1	BC	HBM-D	aPLI model (E)	S4-1-L	RCM4-1	BL	HBM-D	aPLI model (E)

Key

S-ID	simulation ID
IL	impact location
BC	lateral centre of the bumper test area defined in References [1] and [2]
BR	right end of the bumper test area defined in References [1] and [2]
BL	left end of the bumper test area defined in References [1] and [2]

Table A.20 *(continued)*

S-ID	RCM ID	IL	HBM	aPLI model	S-ID	RCM ID	IL	HBM	aPLI model
S4-2-C	RCM4-2	BC	HBM-D	aPLI model (E)	S4-2-L	RCM4-2	BL	HBM-D	aPLI model (E)
S4-3-C	RCM4-3	BC	HBM-D	aPLI model (E)	S4-3-L	RCM4-3	BL	HBM-D	aPLI model (E)
S4-4-C	RCM4-4	BC	HBM-D	aPLI model (E)	S4-4-L	RCM4-4	BL	HBM-D	aPLI model (E)
S4-5-C	RCM4-5	BC	HBM-D	aPLI model (E)	S4-5-L	RCM4-5	BL	HBM-D	aPLI model (E)
S4-6-C	RCM4-6	BC	HBM-D	aPLI model (E)	S4-6-L	RCM4-6	BL	HBM-D	aPLI model (E)
S4-7-C	RCM4-7	BC	HBM-D	aPLI model (E)	S4-7-L	RCM4-7	BL	HBM-D	aPLI model (E)
S4-8-C	RCM4-8	BC	HBM-D	aPLI model (E)	S4-8-L	RCM4-8	BL	HBM-D	aPLI model (E)
S4-9-C	RCM4-9	BC	HBM-D	aPLI model (E)	S4-9-L	RCM4-9	BL	HBM-D	aPLI model (E)
S4-10-C	RCM4-10	BC	HBM-D	aPLI model (E)	S4-10-L	RCM4-10	BL	HBM-D	aPLI model (E)
S4-11-C	RCM4-11	BC	HBM-D	aPLI model (E)	S4-11-L	RCM4-11	BL	HBM-D	aPLI model (E)
S4-12-C	RCM4-12	BC	HBM-D	aPLI model (E)	S4-12-L	RCM4-12	BL	HBM-D	aPLI model (E)
S4-13-C	RCM4-13	BC	HBM-D	aPLI model (E)	S4-13-L	RCM4-13	BL	HBM-D	aPLI model (E)
S4-14-C	RCM4-14	BC	HBM-D	aPLI model (E)	S4-14-L	RCM4-14	BL	HBM-D	aPLI model (E)
S4-15-C	RCM4-15	BC	HBM-D	aPLI model (E)	S4-15-L	RCM4-15	BL	HBM-D	aPLI model (E)
S4-16-C	RCM4-16	BC	HBM-D	aPLI model (E)	S4-16-L	RCM4-16	BL	HBM-D	aPLI model (E)
S4-17-C	RCM4-17	BC	HBM-D	aPLI model (E)	S4-17-L	RCM4-17	BL	HBM-D	aPLI model (E)
S4-18-C	RCM4-18	BC	HBM-D	aPLI model (E)	S4-18-L	RCM4-18	BL	HBM-D	aPLI model (E)
S4-19-C	RCM4-19	BC	HBM-D	aPLI model (E)	S4-19-L	RCM4-19	BL	HBM-D	aPLI model (E)
S4-20-C	RCM4-20	BC	HBM-D	aPLI model (E)	S4-20-L	RCM4-20	BL	HBM-D	aPLI model (E)
S4-21-C	RCM4-21	BC	HBM-D	aPLI model (E)	S4-21-L	RCM4-21	BL	HBM-D	aPLI model (E)
S4-22-C	RCM4-22	BC	HBM-D	aPLI model (E)	S4-22-L	RCM4-22	BL	HBM-D	aPLI model (E)
S4-23-C	RCM4-23	BC	HBM-D	aPLI model (E)	S4-23-L	RCM4-23	BL	HBM-D	aPLI model (E)

Key

S-ID	simulation ID
IL	impact location
BC	lateral centre of the bumper test area defined in References [1] and [2]
BR	right end of the bumper test area defined in References [1] and [2]
BL	left end of the bumper test area defined in References [1] and [2]

Table A.20 *(continued)*

S-ID	RCM ID	IL	HBM	aPLI model	S-ID	RCM ID	IL	HBM	aPLI model
S4-1-R	RCM4-1	BR	HBM-D	aPLI model (E)					
S4-2-R	RCM4-2	BR	HBM-D	aPLI model (E)					
S4-3-R	RCM4-3	BR	HBM-D	aPLI model (E)					
S4-4-R	RCM4-4	BR	HBM-D	aPLI model (E)					
S4-5-R	RCM4-5	BR	HBM-D	aPLI model (E)					
S4-6-R	RCM4-6	BR	HBM-D	aPLI model (E)					
S4-7-R	RCM4-7	BR	HBM-D	aPLI model (E)					
S4-8-R	RCM4-8	BR	HBM-D	aPLI model (E)					
S4-9-R	RCM4-9	BR	HBM-D	aPLI model (E)					
S4-10-R	RCM4-10	BR	HBM-D	aPLI model (E)					
S4-11-R	RCM4-11	BR	HBM-D	aPLI model (E)					
S4-12-R	RCM4-12	BR	HBM-D	aPLI model (E)					
S4-13-R	RCM4-13	BR	HBM-D	aPLI model (E)					
S4-14-R	RCM4-14	BR	HBM-D	aPLI model (E)					
S4-15-R	RCM4-15	BR	HBM-D	aPLI model (E)					
S4-16-R	RCM4-16	BR	HBM-D	aPLI model (E)					
S4-17-R	RCM4-17	BR	HBM-D	aPLI model (E)					
S4-18-R	RCM4-18	BR	HBM-D	aPLI model (E)					
S4-19-R	RCM4-19	BR	HBM-D	aPLI model (E)					
S4-20-R	RCM4-20	BR	HBM-D	aPLI model (E)					
S4-21-R	RCM4-21	BR	HBM-D	aPLI model (E)					
S4-22-R	RCM4-22	BR	HBM-D	aPLI model (E)					

Key

S-ID	simulation ID
IL	impact location
BC	lateral centre of the bumper test area defined in References [1] and [2]
BR	right end of the bumper test area defined in References [1] and [2]
BL	left end of the bumper test area defined in References [1] and [2]

Table A.20 *(continued)*

S-ID	RCM ID	IL	HBM	aPLI model	S-ID	RCM ID	IL	HBM	aPLI model
S4-23-R	RCM4-23	BR	HBM-D	aPLI model (E)					

Key

S-ID	simulation ID
IL	impact location
BC	lateral centre of the bumper test area defined in References [1] and [2]
BR	right end of the bumper test area defined in References [1] and [2]
BL	left end of the bumper test area defined in References [1] and [2]

A.2.4.3.2 Simulation model setup

All the impact simulations were performed at the impact speed of 11,1 m/s. Impacts were delivered by the RCMs in the lateral-to-medial direction of either the struck-side lower limb of an HBM or an aPLI model. As the bottom of aPLI corresponds to the sole of the barefoot, the impact height of the aPLI models was set at 25 mm above the ground to compensate for the height of the sole of the shoe. Due to variability in the length of the lower limb of the HBMs used, the impact height of the HBMs were set in such a way that the height of the knee joint surface coincides with that of the aPLI models as shown in Figure A.40. A gravity field was applied entirely to all models. The lower limb orientation of the HBMs was set such that the line connecting the centre of the hip joint and the ankle joint of the struck-side lower limb is vertical to the ground, and the same line on the non-struck side is rotated 20° forward about the hip joint as shown in Figure A.41. The line on the struck-side lower limb was positioned at the impact location on the RCM as illustrated in Figure A.42. Element elimination option of the HBMs representing failure of the tissues were inactivated, except for the fibula, to predict maximum loads on the femur, tibia and MCL, while maintaining realistic loading conditions of the tibia for which injury metrics are set for the aPLI.

The vertical centre line of the femur and tibia bone cores (beams made of glass fiber reinforced plastic representing the bending characteristics of the femur and the tibia installed in the femur and tibia segments of the aPLI as shown in Figure A.43) was positioned vertical to the ground and at the impact location on the RCM as illustrated in Figure A.44.

Injury metrics of the HBMs (femur BM, tibia BM and knee valgus angle) and the aPLI model (femur BM, tibia BM and MCL elongation) were measured by following the same procedure as detailed in A.2.2.2.2 and illustrated in Figure A.45.

The maximum values of the injury metrics for the thigh, leg and knee were recorded and used for the regression analysis to develop TFs.

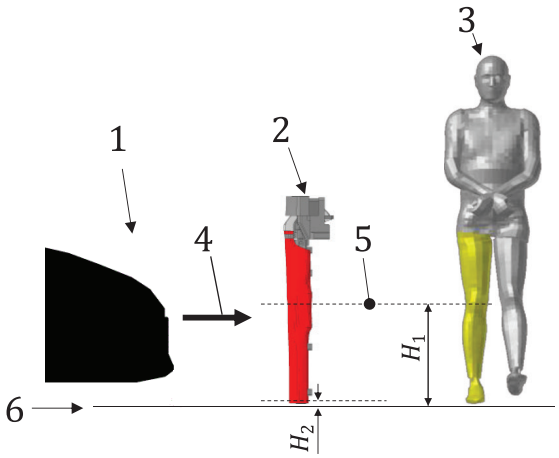

Key

1 SCM
2 aPLI FE model
3 HBM
4 11,1 m/s
5 knee joint
6 ground level
H_1 519 mm
H_2 25 mm

Figure A.40 — RCM versus HBM and aPLI model impact condition

a) Struck-side view **b) Back view**

Key

1 hip-joint centre
2 struck side of vertical lower limb
3 ankle-joint centre
4 line connecting the centre of the hip joint and the ankle joint
5 20°
6 non-struck side of straight lower limb
7 ankle-joint centre

Figure A.41 — Definition of the line connecting the centre of the hip joint and the ankle joint of the HBM

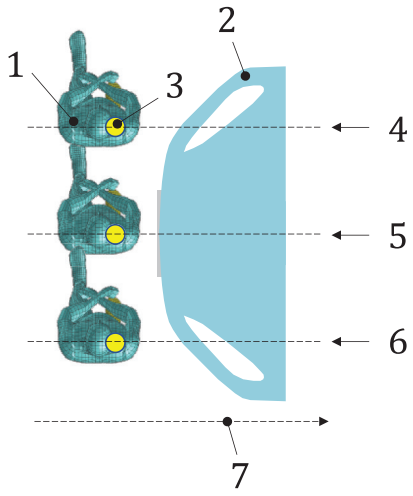

Key

1 HBM
2 RCM
3 vertical centre line of the femur and tibia bone cores
4 BP right
5 BP centre
6 BP left
7 car longitudinal axis

NOTE This is the top view.

Figure A.42 — RCM versus HBM impact locations

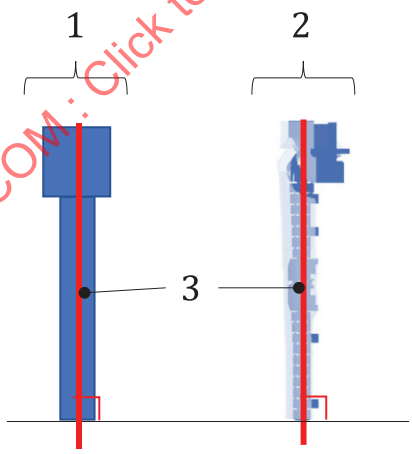

Key

1 Struck-side view
2 perpendicular view to the struck side
3 vertical centre line of the femur and tibia bone cores along the centre of bone core

Figure A.43 — Definition of the vertical centre line of the femur and tibia bone cores for the aPLI

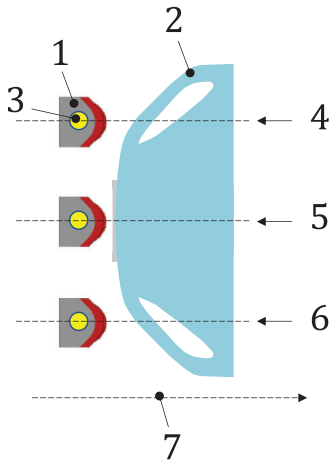

Key

1 aPLI FE model
2 RCM
3 vertical centre line of the femur and tibia bone cores
4 BP right
5 BP centre
6 BP left
7 car longitudinal axis

NOTE This is the top view.

Figure A.44 — RCM versus aPLI model impact locations

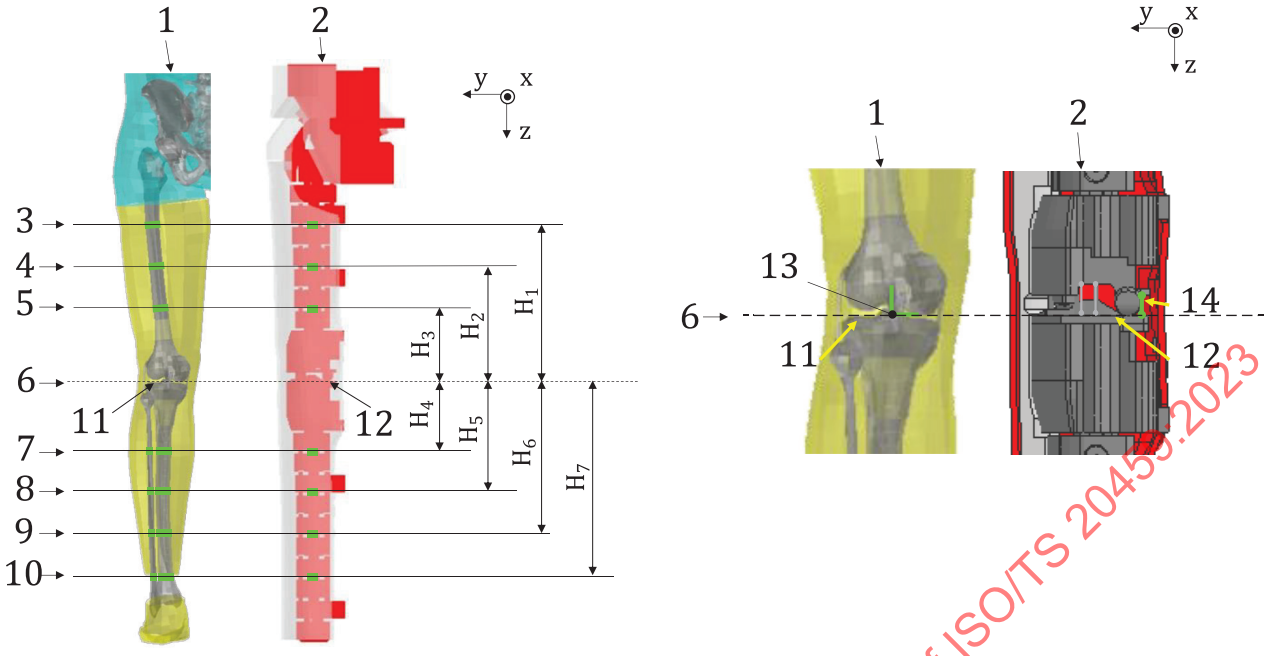

a) Long bones **b) Knee**

Key

1 HBM
2 aPLI FE model
3 BM measurement location (femur-3)
4 BM measurement location (femur-2)
5 BM measurement location (femur-1)
6 knee joint
7 BM measurement location (tibia-1)
8 BM measurement location (tibia-2)
9 BM measurement location (tibia-3)
10 BM measurement location (tibia-4)
11 tibial plateau
12 flat surface of tibial plateau
13 knee valgus angle measured at knee-joint centre
14 MCL elongation
H_1 297 mm
H_2 217 mm
H_3 137 mm
H_4 134 mm
H_5 214 mm
H_6 294 mm
H_7 374 mm

Figure A.45 — Measurement location of the peak value of injury metrics

A.2.4.4 Results

A.2.4.4.1 Thigh

The TF for the thigh defines the relationship between the maximum values of the femur BM from the aPLI models and those from the HBMs obtained from the impact simulations.

Figure A.46 presents the TF for the thigh with the individual data points plotted. The horizontal axis represents the maximum value of the femur BM of the aPLI models, and the vertical axis represents the maximum value of that of the HBMs. As shown in Figure A.46, the slope of the TF is 1,04. Tabulated data are provided at:

https://standards.iso.org/iso/ts/20459/ed-1/en

The time history plots of all of the three injury metrics of the femur for the aPLI models and the HBMs can be found in C.2.

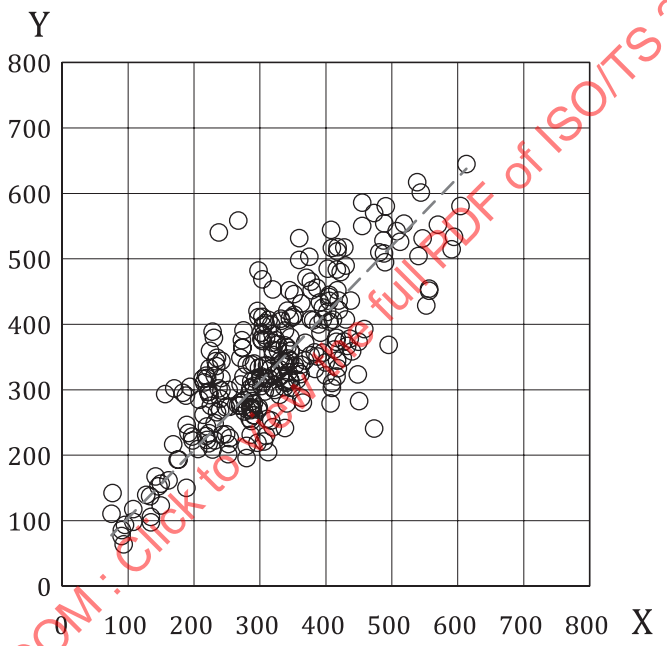

Key

X	femur BM of the six aPLI models
Y	femur BM of the four HBMs
○	data
– – –	transfer function for thigh (C_{Slope} is 1,04)

Figure A.46 — TF for the thigh

A.2.4.4.2 Leg

The TF for the leg defines the relationship between the maximum values of the tibia BM from the aPLI models and those from the HBMs obtained from the impact simulations.

Figure A.47 presents the TF for the leg with the individual data points plotted. The horizontal axis represents the maximum value of the tibia BM of the aPLI models, and the vertical axis represents the maximum value of the tibia BM of the HBMs. As shown in Figure A.47, the slope of the TF is 0,881. Tabulated data are listed provided at:

https://standards.iso.org/iso/ts/20459/ed-1/en

The time history plots of all of the four injury metrics of the tibia for the aPLI models and the HBMs can be found in C.2.

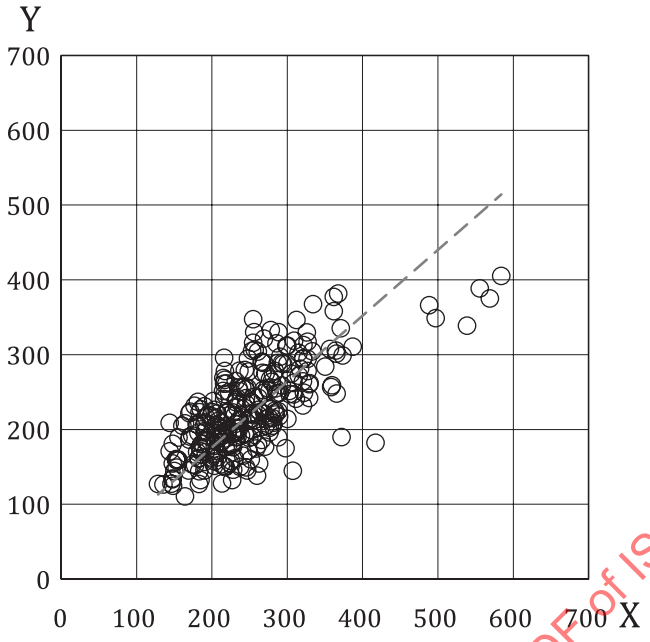

Key

○	data
– – –	transfer function for leg (C_{Slope} is 0,881)
X	tibia BM of the six aPLI models
Y	tibia BM of the four HBMs

Figure A.47 — TF for the leg

A.2.4.4.3 Knee

The TF for the knee defines the relationship between the maximum values of the MCL elongation from the aPLI models and the maximum values of the knee valgus angle from the HBMs obtained from the impact simulations.

Figure A.48 presents the TF for the knee with the individual data points plotted. The horizontal axis represents the maximum value of the MCL elongation of the aPLI models, and the vertical axis represents the maximum value of the knee valgus angle of the HBMs. As shown in Figure A.48, the slope of the TF is 1,14. Tabulated data are provided at:

https://standards.iso.org/iso/ts/20459/ed-1/en

The time history plots of the injury metrics of the knee for the aPLI models and the HBMs can be found in C.2.

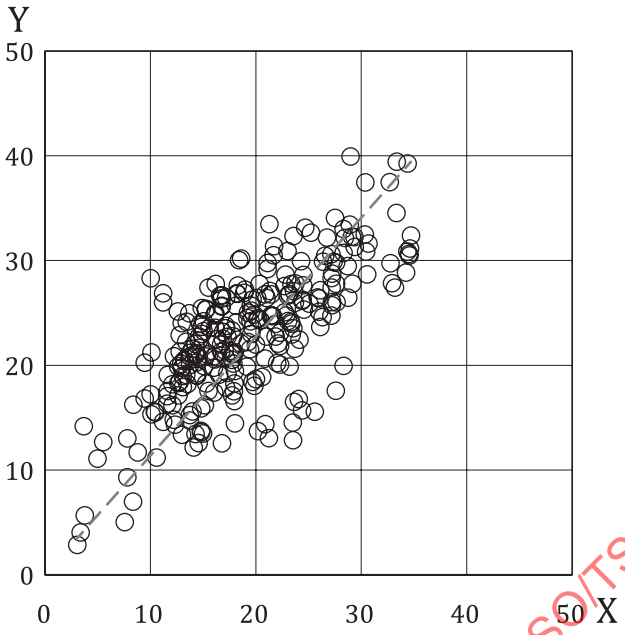

Key

X	MCL elongation of the six aPLI models
Y	knee valgus angle of the four HBMs
○	data
– – –	transfer function for knee (C_{Slope} is 1,14)

Figure A.48 — TF for the knee

A.2.5 Development of IPFs for the aPLI in the load case specified in the STP

A.2.5.1 General

Injury values of human IPFs in the load case specified in the STP (human IPFs-STP) developed in A.2.3 are to be converted to injury values of the aPLI using the TFs determined in A.2.4 to develop IPFs for the aPLI in the load case specified in the STP (aPLI IPFs-STP). The aPLI IPFs-STP are validated against real-world accident data (see A.2.6) and are subjected to further theoretical and/or empirical adjustment (Annex B).

A.2.5.2 Methodology

The injury metric for human in the formula of human IPFs-STP developed in A.2.3 is converted by using Formula (A.8):

$$x_{\text{human}} = C_{\text{Slope}} \times x_{\text{aPLI}} \tag{A.8}$$

where

x_{human} is the value of the injury metric for human;

C_{Slope} is the slope of the TF determined for the corresponding injury metric in A.2.4;

x_{aPLI} is the value of the injury metric for the aPLI.

A.2.5.3 Results

A.2.5.3.1 Thigh

Figure A.49 presents the aPLI IPF-STP for the thigh with the 95 % confidence interval. The injury probability function is shown in a solid line and the 95 % confidence interval shown in dotted lines. The horizontal axis represents the femur BM measured by the aPLI, and the vertical axis represents the probability of injury in the load case specified in the STP.

The aPLI IPF-STP for the thigh is given by Formula (A.9):

$$P = 1 - \exp\left\{-\left(\frac{C_{\text{Slope}} \times x_{\text{aPLI}}}{C_{\text{Scale}}}\right)^{C_{\text{Shape}}}\right\} \quad \text{(A.9)}$$

where

P is the injury probability for the femur shaft of human;

C_{Scale} is the parameter determined for the Weibull distribution for the human IPF for the femur shaft as described in A.2.3.4.1;

C_{Shape} is the parameter determined for the Weibull distribution for the human IPF for the femur shaft as described in A.2.3.4.1;

C_{Shape} is the slope of the TF for the thigh as described in A.2.4.4.1;

x_{aPLI} is the femur BM measured by the aPLI in Nm.

The parameters needed to define the aPLI IPF-STP for the femur shaft are described in Table A.21.

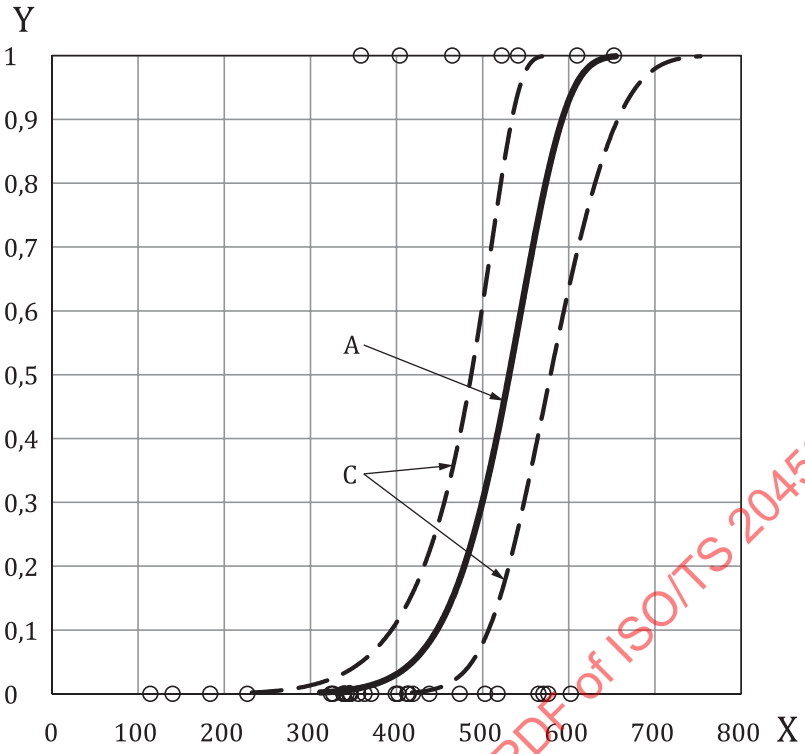

Key

X	aPLI femur BM [Nm]
Y	injury probability for the femur shaft in the load case specified in STP
A	aPLI IPF for femur shaft in the load case specified in STP
C	95 % confidence interval
◯	observed data

Figure A.49 — aPLI IPF-STP (femur shaft)

Table A.21 — Parameters of the aPLI IPF-STP (femur shaft)

C_{Scale}	C_{Shape}	C_{Slope}
571	11,0	1,04

A.2.5.3.2 Leg

Figure A.50 presents the aPLI IPF-STP for the leg with a 95 % confidence interval. The injury probability function is shown in a solid line and the 95 % confidence interval shown in dotted lines. The horizontal axis represents the tibia BM measured by the aPLI, and the vertical axis represents the probability of injury in the load case specified in the STP.

The aPLI IPF-STP for the leg is given by Formula (A.10):

$$P = 1 - \exp\left\{-\left(\frac{C_{Slope} \times x_{aPLI}}{C_{Scale}}\right)^{C_{Shape}}\right\} \quad \text{(A.10)}$$

where

P is the injury probability for the tibia shaft of human;

C_{Scale} is the parameter determined for the Weibull distribution for the human IPF for the tibia shaft as described in A.2.3.4.2;

C_{Shape} is the parameter determined for the Weibull distribution for the human IPF for the tibia shaft as described in A.2.3.4.2;

C_{Slope} is the slope of the TF for the leg as described in A.2.4.4.2;

x_{aPLI} is the tibia BM measured by the aPLI in Nm.

The parameters needed to define the aPLI IPF-STP for the tibia shaft are described in Table A.22.

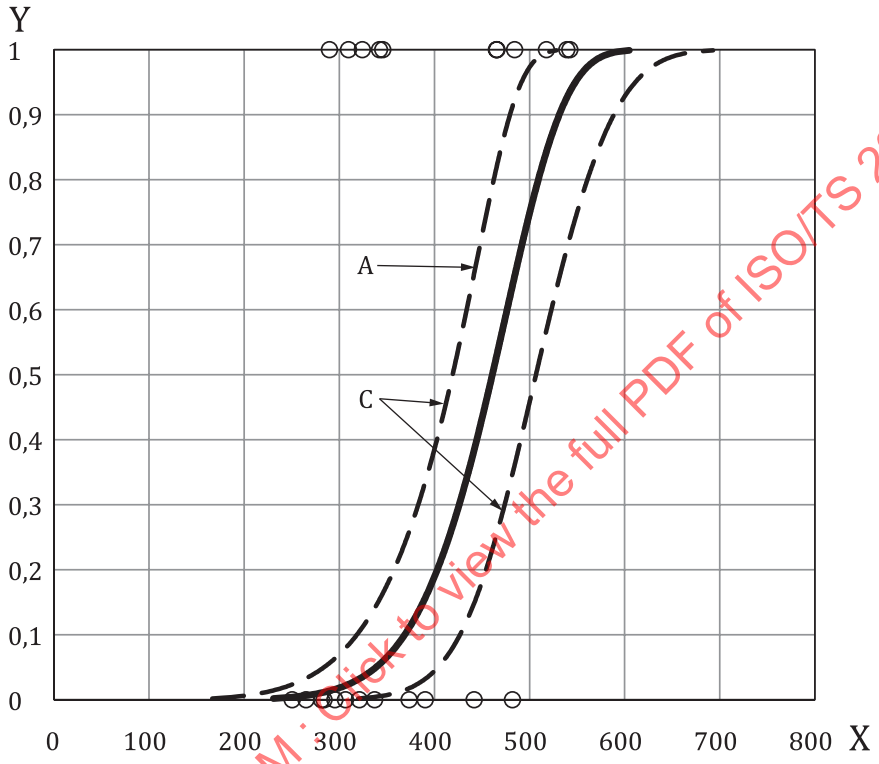

Key

X aPLI tibia BM [Nm]

Y injury probability for the tibia shaft in the load case specified in STP

A aPLI IPF for tibia shaft in the load case specified in STP

C 95 % confidence interval

◯ observed data

Figure A.50 — aPLI IPF-STP (tibia shaft)

Table A.22 — Parameters of the aPLI IPF-STP (tibia shaft)

C_{Scale}	C_{Shape}	C_{Slope}
424	8,45	0,881

A.2.5.3.3 Knee

Figure A.51 presents the aPLI IPF-STP for the knee with a 95 % confidence interval. The injury probability function is shown in a solid line and the 95 % confidence interval shown in dotted lines. The horizontal axis represents the MCL elongation measured by the aPLI, and the vertical axis represents the probability of injury in the load case specified in the STP.

The aPLI IPF-STP for the knee is given by Formula (A.11):

$$P = \frac{1}{C_\sigma \sqrt{2\pi}} \int_0^{C_{Slope} \times x_{aPLI}} \frac{1}{t} \exp\left\{ \frac{-\left(\ln t - C_\mu\right)^2}{2{C_\sigma}^2} \right\} dt \quad \text{(A.11)}$$

where

P is the injury probability for the MCL of human;

C_σ is the parameter determined for the Log-Normal distribution for human IPFs for the MCL as described in A.2.3.4.3;

C_σ is the parameter determined for the Log-Normal distribution for human IPFs for the MCL as described in A.2.3.4.3;

C_{Slope} is the slope of the TF for the knee as described in A.2.4.4.3;

x_{aPLI} is the MCL elongation measured by the aPLI in mm.

The parameters needed to define the aPLI IPF-STP for the MCL are described in Table A.23.

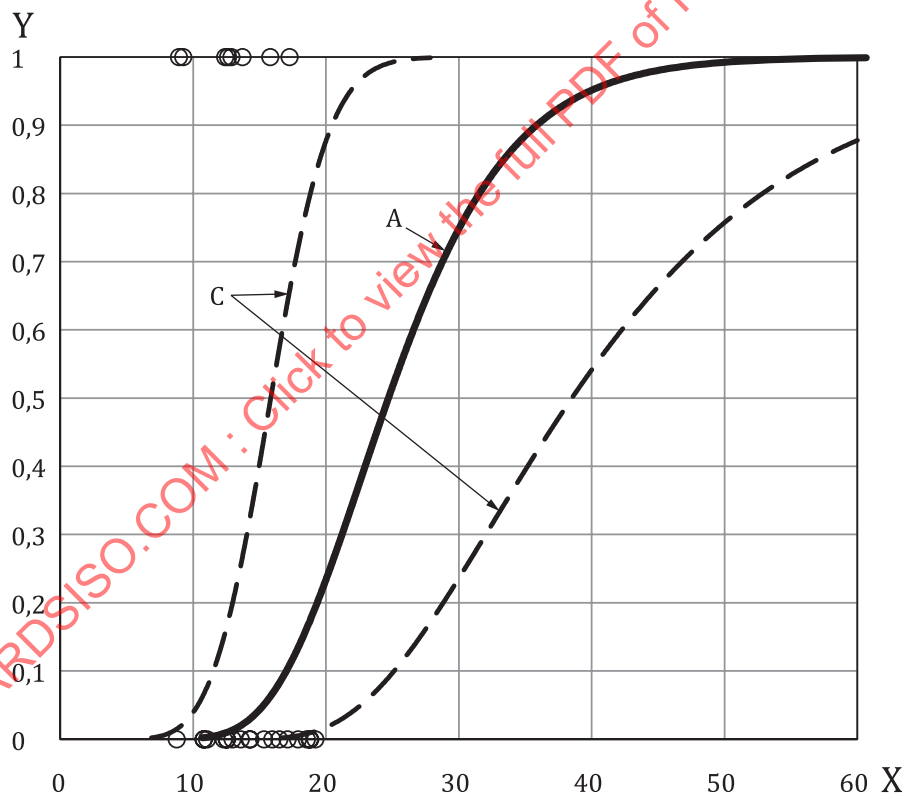

Key

X aPLI MCL elongation [mm]

Y injury probability for the MCL in the load case specified in STP

A aPLI IPF for MCL complete rupture in the load case specified in STP

C 95 % confidence interval

◯ observed data

Figure A.51 — aPLI IPF-STP (MCL)

Table A.23 — Parameters of the aPLI IPF-STP (MCL)

C_{μ}	C_{σ}	C_{Slope}
3,34	0,291	1,14

A.2.6 Validation of the aPLI IPFs-STP

A.2.6.1 General

Validation of the aPLI IPFs-STP against accident data and adjustment of the IPFs, whenever needed, is crucial to ensure that the probability of injury predicted by the IPFs reasonably represents morbidity in the real-world accidents. At the same time, it is also a challenging work due to essentially large variability in the parameters describing both the load case in the accident and human impact response and tolerance. For this reason, two groups under the aPLI TG (Group A and B) individually validated the aPLI IPFs-STP developed in A.2.5 with respect to real-world relevance to clarify the need for the adjustment to the real-world data, and adjusted the IPFs that were found to show discrepancy from the field data as detailed in Annex B.

Group A validated the aPLI IPFs-STP by comparing the morbidity and the number of injuries predicted by the aPLI IPFs-STP against those calculated from accident data. In contrast, Group B developed a methodology which is based on the comparison of test data from real car aPLI tests with accident data. Detailed methodology and results of the validation conducted by Group A and B are described in A.2.6.2 and A.2.6.3, respectively.

A.2.6.2 Validation (Group A)

A.2.6.2.1 Methodology

First, an accident database was investigated and the data were filtered to extract specific accidents of interest, and the number of injuries in question and the morbidity were calculated for this mother group. Second, the morbidity for the corresponding load cases to those of the filtered accident data was estimated from the aPLI IPFs-STP, and the number of injuries was estimated using the exposure from the accident data. Finally, the observed and predicted number of injuries in the specific load cases of interest were compared to validate the aPLI IPFs-STP and clarify the need for further adjustments.

A.2.6.2.1.1 Observed number of injuries and morbidity

Group A used a German pedestrian accident database called the German In-Depth Accident Study (GIDAS) database version 12/2018 to validate the aPLI IPFs-STP determined in A.2.5. This database was chosen because it contains detailed pedestrian accident information, including extensive scene and vehicle inspection and injury description, comprising one of the most useful databases in terms of both quantity and quality. The following selection criteria was applied to the GIDAS database to filter the cases relevant to the pedestrian load cases represented by the aPLI STP:

— pedestrian age of 16 years old and older;

— pedestrians involved in a collision against a single vehicle;

— pedestrians hit while standing, walking or running;

— pedestrians not run over by a vehicle;

— no extreme sideswipes were included, such as a pedestrian being struck by a side mirror;

— pedestrian collision against a forward-driving M1/N1 vehicle;

— frontal collision of the vehicles against the pedestrians;

— impact speed up to 65 km/h;

— impact angle: 0° and ±30° including symmetric angles;

— vehicles with no roll over;

— no sliding of the vehicles/driver loss of control prior to the accident.

The pedestrian subsystem test procedure to be used with an aPLI specifies the impact speed of 40 km/h (see References [1] and [2]). However, comparison of predicted and observed number of injuries and morbidity at this specific impact speed would diminish the number of data from the accident database and thus statistical significance of the validation results. Consequently, it was decided to compare the number of injuries and the morbidity for the impact speed range of (0-65) km/h by estimating the trend of the maximum values of aPLI injury metrics against impact speed by means of computational impact simulations. The upper limit of the impact speed range was set at 65 km/h because both observed and predicted morbidity were found to be small up to 40 km/h, while the number of accident cases was found to be minimal above 65 km/h. In this speed range, the total number of filtered accident cases comprising the mother group was 1 183.

In order to compare predicted and observed number of injuries and morbidity for injuries predicted by the aPLI injury metrics, the comparisons were made for femur shaft fracture, tibia shaft fracture and MCL complete failure. The number of injuries was obtained by further filtering the cases with the pedestrian sustaining the following injuries with the AIS code (AIS 2005 update 2008 codes[34]) described in Table A.24. The AIS code consists of six digits left of the decimal point (pre-dot code) and one digit right to the decimal point (post-dot code). The initial digit represents the body region and 8 corresponds to the lower extremity. The following digit represent the type of anatomic structure, with 4 and 5 corresponding to “organs (including muscles/ligaments)” and “skeletal (including joints)”, respectively. The post-dot code of 2 and 3 represents moderate and serious injury, respectively. With regards to femur and tibia shaft fracture, there were directly corresponding AIS codes as shown in Table A.24. On the contrary, due to there being no AIS code which corresponded to complete MCL rupture directly, the AIS code for collateral ligament complete rupture was used as shown in Table A.24. As the number of injuries was simply counted by the number of these AIS codes, multiple injuries to a single pedestrian were counted for each of the filtered injuries. The morbidity was calculated by simply dividing the number of corresponding injuries with the number of pedestrians in the mother group. The data were grouped by the representative impact speed with 5 km/h increments by assigning the data with the representative impact speed ±2,5 km/h.

Table A.24 — AIS codes used for filtering

Injured body part	AIS code (AIS 2005 update 2008 codes)				
	Body region (1 digit)	Type of anatomic structure (1 digit)	Specific anatomic structure (2 digit)	Level (2 digit)	AIS severity (1 digit)
Femur shaft	8	5	32	any (21, 22, 51, 52, 61, 62, 71, 72)	3
Tibia shaft	8	5	42	any (21, 51, 61, 71)	2
				any (22, 52, 62, 72)	3
Knee ligaments	8	4	04	07	2

A.2.6.2.1.2 Predicted number of injuries and morbidity

The morbidity was estimated for each of the injuries in question from the injury values measured by the aPLI and the aPLI IPFs-STP. As 87,9 % of vehicles involved in the cases of the mother group were sedans, the mean of the maximum injury values of aPLI injury metrics were calculated from the round robin test results for German sedans to represent the injury values at 40 km/h. Due to the lack of experimental data for other impact speeds, computer simulations were run using a sedan type generic vehicle model[35] and the aPLI model (A) described in A.2.4.2.1. Simulations were run at the impact speeds up to 65 km/h, including 40 km/h, at 5 km/h increments. All the injury values were normalised by that at 40 km/h, and the injury values at 40 km/h determined from the experimental data were multiplied by the normalised injury values to estimate the injury values at the impact speeds other than 40 km/h.

The morbidity was estimated for each impact speed by applying the estimated aPLI injury values to the aPLI IPFs-STP. The number of injuries was then predicted for each of the impact speeds by multiplying the number of pedestrians in the corresponding impact speed range by the estimated morbidity.

Table A.25 — Frequency of car type in the GIDAS database filtered for the current study

Vehicle type	Frequency
Very small cars	6,3 %
Sedan	87,9 %
Small cars	20,6 %
Lower middle-class cars	36,3 %
Middle-class cars	24,1 %
Upper middle-class cars	6,4 %
Upper-class cars	0,4 %
SUV	2,3 %
Sports cars	0,5 %
Mini vans	0,6 %
Large vans	2,3 %
Passenger car without further information	0,1 %

A.2.6.2.1.3 Comparison between observation and prediction

The number of injuries and the morbidity were obtained from the accident database, or estimated by the aPLI injury values, for the impact speeds up to 65 km/h at 5 km/h increments. Due to the small number of injuries in the filtered datasets, the observed and predicted number of injuries for each of the representative impact speed were summed up to 65 km/h for comparison purposes. The morbidity was compared as a function of the impact speed to evaluate the trend of the probability of injury over the impact speed.

A.2.6.2.2 Results

A.2.6.2.2.1 Observed number of injuries and morbidity

Table A.26 shows the number of pedestrians in the mother group by the representative speed. Figure A.52 presents the number of injuries by the representative impact speed, along with the morbidity by the representative impact speed for the thigh (femur fracture), the leg (tibia fracture) and the knee (complete MCL failure). The morbidity tended to get larger as the impact speed goes up.

The total number of injuries was 7, 63 and 11 for the thigh (femur shaft fracture), the leg (tibia shaft fracture) and the knee (complete MCL failure), respectively.

Table A.26 — Number of pedestrians in the mother group by the representative speed

Impact speed (km/h)	0	5	10	15	20	25	30	35	40	45	50	55	60	65
Number of pedestrians	6	70	98	131	172	131	152	92	135	89	65	18	20	15

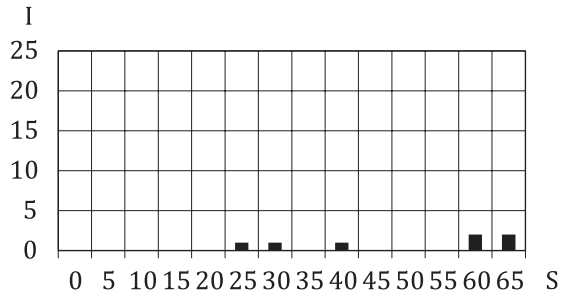

a) Femur shaft - Number of injuries

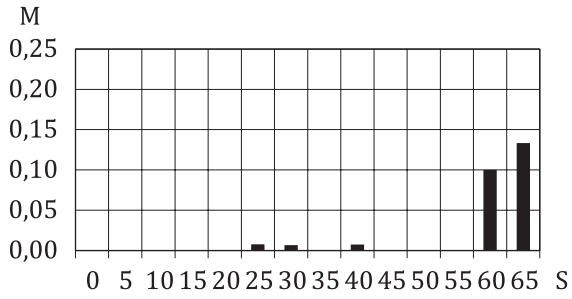

b) Femur shaft - Morbidity

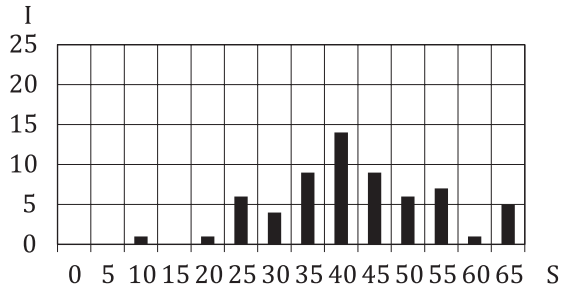

c) Tibia shaft - Number of injuries

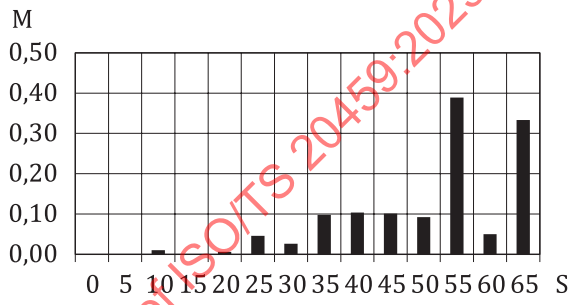

d) Tibia shaft - Morbidity

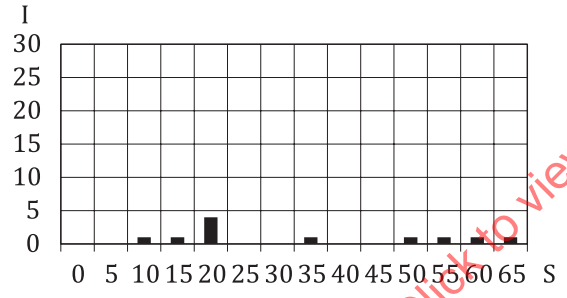

e) MCL - Number of injuries

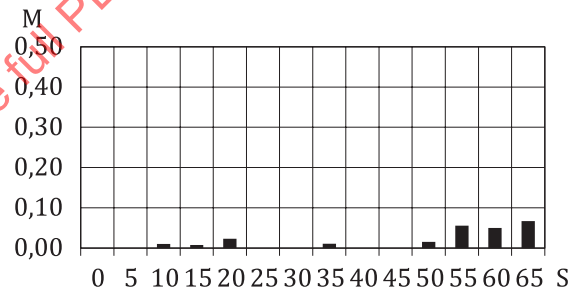

f) MCL - Morbidity

Key

I number of injuries (-)
M morbidity (-)
S impact speed [km/h]

Figure A.52 — Number of injury and morbidity by impact speed obtained from the accident database

A.2.6.2.2.2 Predicted number of injuries and morbidity

Figure A.53 shows the maximum injury values predicted by the computational impact simulations using the sedan type generic vehicle model and the aPLI model (A) normalised by the values at 40 km/h for the thigh (femur shaft fracture), the leg (tibia shaft fracture) and the knee (complete MCL failure). The injury values tended to get larger as the impact speed goes up, except the femur BM at higher speeds exhibiting saturation due to the change of the car front shape at the thigh impact area from a pontoon type to a flat type which causes less bending of the femur as it supports the thigh over a wide range in the longitudinal direction due to the flat surface. The mean injury values at 40 km/h obtained from the round robin tests on German sedans were 283 Nm, 233 Nm and 14,8 mm for the thigh (femur BM), the leg (tibia BM) and the knee (MCL elongation), respectively. Those values were multiplied by the normalised injury values presented in Figure A.53 to estimate the injury values as functions of the

impact speed shown in Figure A.54. Figure A.55 shows the estimated morbidity by the impact speed calculated by applying the injury values shown in Figure A.54 to the aPLI IPFs-STP determined in A.2.5.

The predicted total number of injuries was 1, 4 and 47 for the thigh (femur shaft fracture), the leg (tibia shaft fracture) and the knee (complete MCL failure), respectively.

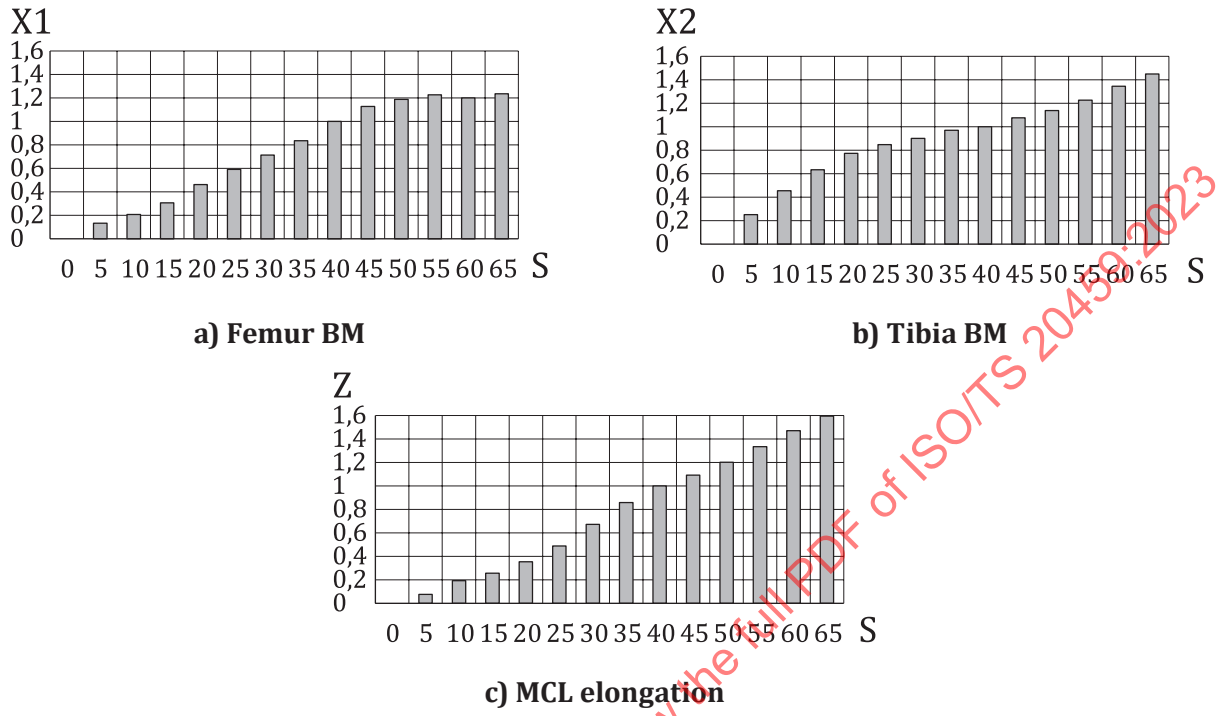

a) Femur BM

b) Tibia BM

c) MCL elongation

Key

X1 normalized aPLI femur BM (-)
X2 normalized aPLI tibia BM (-)
Z normalized aPLI MCL elongation (-)
S impact speed [km/h]

Figure A.53 — Maximum injury values of aPLI by impact speed normalised by those at 40 km/h obtained from computational impact simulations

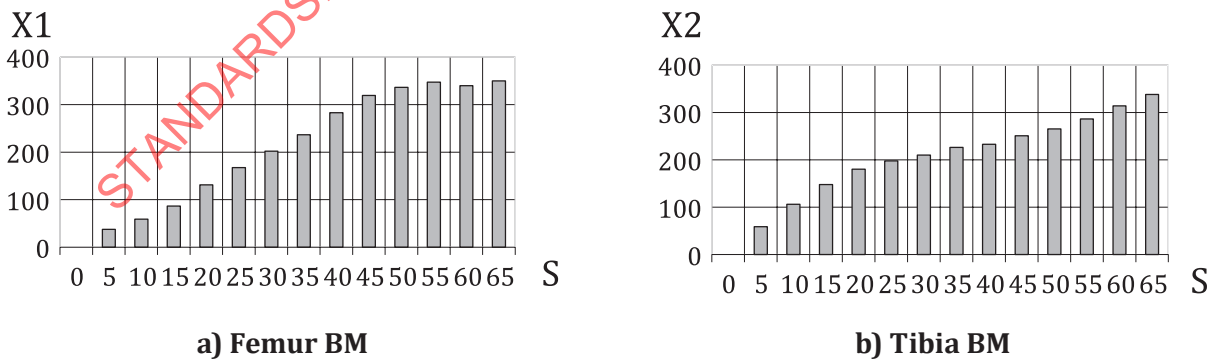

a) Femur BM

b) Tibia BM

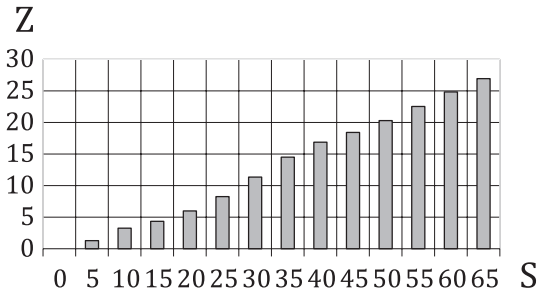

c) MCL elongation

Key

X1 aPLI femur BM [Nm]
X2 aPLI tibia BM [Nm]
Z aPLI MCL elongation [mm]
S impact speed [km/h]

Figure A.54 — Maximum injury values of aPLI by impact speed estimated from the combination of experimental data and computational prediction

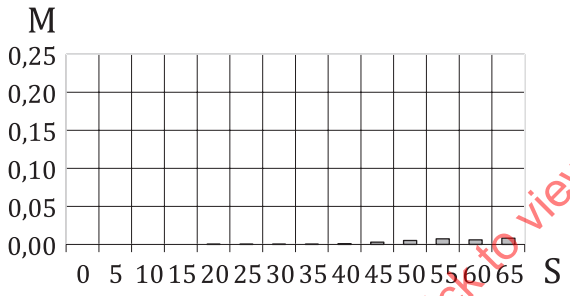

a) Femur shaft

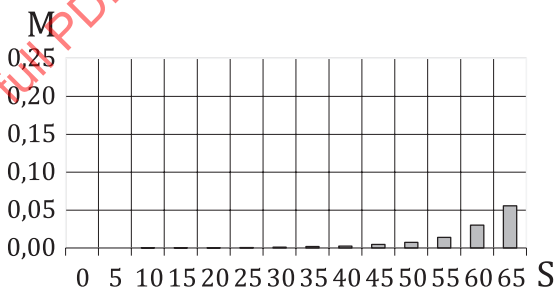

b) Tibia shaft

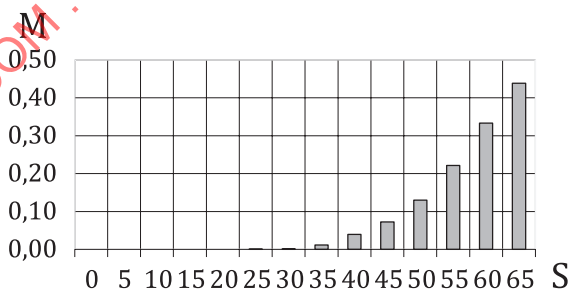

c) MCL

Key

M morbidity (-)
S impact speed [km/h]

Figure A.55 — Predicted morbidity by impact speed

A.2.6.2.2.3 Comparison between observation and prediction

Table A.27 compares the observed and predicted number of injuries for the thigh (femur shaft fracture), the leg (tibia shaft fracture) and the knee (complete MCL failure). The percentage of the difference of morbidity between the field observation and the prediction relative to the number of pedestrians in

the mother group (1 194) was 0,5 %, 5,3 % and 2,4 % for the thigh, the leg and the knee, respectively, as shown in Table A.28. Due to significantly small number of injuries and the overall morbidity for the thigh, it was decided not to further consider adjustment to the real-world accident data as the difference was deemed much less than the variability of human biomechanical data and thus further modifications are not justified. Since the percentage of the difference of morbidity was 2 % or more for the leg and the knee, it was decided to adjust the aPLI IPF-STP for these injuries to enhance relevance of the IPFs to the real-world accidents. It is important to note that the number of leg injury (tibia fracture) was underestimated, while the number of knee injury (complete MCL failure) was overestimated.

Table A.27 — Comparison between observed and predicted number of injuries

Number of injuries	Thigh	Leg	Knee
Accident data	7	63	11
Prediction	1	3	39
(difference to accident data)	(-6)	(-60)	(+28)

Table A.28 — Comparison between observed and predicted morbidity

Dimensions in percentages

Morbidity	Thigh	Leg	Knee
Accident data	0,6	5,6	0,9
Prediction	0,1	0,3	3,3
(difference to accident data)	(-0,5)	(-5,3)	(+2,4)

A.2.6.3 Validation (Group B)

A.2.6.3.1 Methodology

The aim of the developed "cross-check-value" methodology was to cross-check impactor output and potential thresholds with real-life accident injury data. Based on this a direct comparison between impactor measurements and accident data should be created without the usage of any PMHS test data or computational simulations.

A.2.6.3.1.1 General description

Figure A.56 presents a schematic overview about the "cross-check-value" methodology.

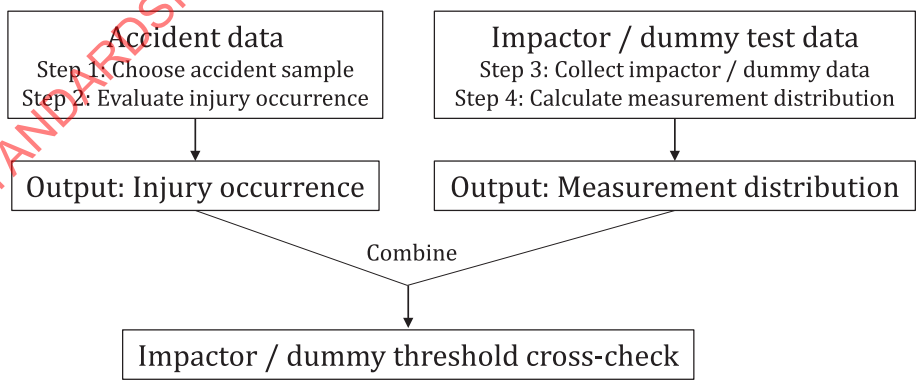

Figure A.56 — Schematic overview of "cross-check-value" methodology

In a first step a suitable sample of accident data is needed. These data set shall be representative for the investigated load case and shall contain detailed information about the accident like vehicle type, vehicle speed, detailed injury description (preferably AIS codes), etc. To create the sample out of an accident database it is recommended to use as many filters as necessary to qualify (comparison with impactor/

dummy test setup) but as few filters as possible to maintain statistical value and representativeness. This sample is considered as the 100 % of all injured persons for this specific type of accident.

Next step deals with the evaluation of the injury occurrence within the sample data set. This shall be done individually for each specific injury and the injury shall be measurable by the investigated impactor / dummy test. Following it shall be evaluated how many persons within the sample data sustained the investigated injury. It is not relevant how the injury was caused.

In step three a sufficient (as large as possible) number of impactor / dummy tests shall be conducted or collected. It is important to use different type of vehicles (sedan, SUV, sportscars) that are representative of the accident data sample with which they are to be compared. Furthermore, the test data should match the boundary conditions of the accident sample as closely as possible.

The task in the fourth step is to calculate the measurement distribution from the impactor data for each injury. In most of the cases it is advisable to assume that the variable follows a normal distribution.

Finally, the accident data and impactor / dummy test data shall be merged. For this combination the key assumption is that the test data represent the accident sample. Furthermore, the methodology implies that a higher impactor measurement means a higher injury risk for real humans. Following these assumptions, the injury occurrence can be matched with the test data distribution. To compare the test and accident data sets, the portion above the injury occurrence value of the normal distribution shall be calculated. Then the impactor measure value for which the cumulative probability is corresponding to the occurrence value shall be calculated.

A.2.6.3.1.2 Limitations of the methodology

The “cross-check-value” methodology delivers impactor-specific values which give an indication of injury risk in real-life accidents and can be used to cross-check impactor-specific injury risk curves or thresholds.

The quality of the cross check depends on:

— the capability of the dummy / impactor to capture the real human injury mechanism;

— the total number of accidents included, and total number of tests included;

— the comparability between tests and accidents of the tested vehicles, impact speeds, etc.

The cross-check value cannot be used as a substitute for injury risk functions, because it captures human diversity only indirectly and not complete. Injury risk functions from current methods are still needed.

The “cross-check-value” only serves as a plausibility check against real-life accidental injuries.

A.2.6.3.2 Results

Group B used the methodology described above to “cross-check” the output of real car tests during the aPLI round robin test with the aPLI version SBL-A with the GIDAS data base (version 12/2017).

A.2.6.3.2.1 Accident sample

In order to create a suitable sample data set, only completely reconstructed and finally closed cases in GIDAS were considered. Furthermore, any cases with non-motorized conveyances (e.g. wheelchairs, stroller, sport equipment) were excluded. This was done to keep out cases which differs too much from the STP. The main filter used for the resulting cases was “pedestrians hit by a passenger car front that were standing / walking / running”. It was explicitly decided to not use further filters, e.g. regarding vehicle speed or model year, pedestrian size or age, or injury causation to keep the sample size as large and multifaceted as possible.

The resulting sample size was n = 1 853 pedestrians. This sample is considered as 100 % of all pedestrians in real-life accidents (with the chosen boundary conditions).

A.2.6.3.2.2 Injury occurrences

According to the second step to create the "cross-check values", the injury occurrences for tibia, MCL and femur were evaluated within the sample data set. Since the aPLI is only able to measure bone bending moments and MCL elongations, only the corresponding injuries could be evaluated. Table A.29 shows the evaluation results. It shall be mentioned that for the knee ligament injuries the AIS coding does not allow distinguishing between MCL and LCL, so here, all knee ligament injuries are included as a worst-case approach.

Table A.29 — Evaluated injury occurrences for tibia, femur and MCL

Injury	aPLI measure	AIS code	Occurrence
Tibia shaft fracture	Tibia bending moment	AIS 8532xx.3	5,2 %
Knee ligament injury	MCL elongation	AIS 8404/5xx.2	1,3 %
Femur shaft fracture	Femur bending moment	AIS 8542xx.x	1,3 %

A.2.6.3.2.3 Test data

Group B chose the aPLI round robin test with the aPLI version SBL-A as an adequate test set for step three to evaluate the “cross-check-value”. These test set contains n= 101 aPLI tests (SBL-A version) against 17 different real car models from the European fleet. The tests were conducted to the vehicle centre line as well as the end of bumper test area (defined in Reference [1]). All these vehicles fulfil the requirements of Reference [1] regarding testing with the FlexPLI.

A.2.6.3.2.4 Measurement distribution of test data

As described in step four, the measurement distribution from the aPLI tests has been calculated. It has been assumed that the variable follows a normal distribution. The resulting mean values (μ) and standard deviations (σ) are shown in Table A.30.

Table A.30 — Evaluated injury occurrences for tibia, femur and MCL

	Max. tibia	Max. femur	Max. MCL
Mean value (μ)	271,7 Nm	373,1 Nm	25,4 mm
standard deviation (σ)	69,4 Nm	89,1 Nm	5,8 mm

A.2.6.3.2.5 Combination of accident and test data set

Figure A.57 through Figure A.59 shows the results of combination for tibia, MCL and femur values and the resulting “cross-check-values”. For visualization purposes, both the actual impactor test data and the normal distribution were plotted in one diagram. The “cross-check-value” was fitted-in as a vertical dotted line.

A comparison between the “cross-check-values” and the corresponding aPLI IPF-STP for leg, knee and thigh was made and a high discrepancy between injury risk level determined by the aPLI IPF-STP and the accident occurrences was observed. Table A.31 lists the “cross-check-values” and the injury occurrence in comparison to the injury risk determined with the aPLI IPF-STP for tibia, MCL and femur.

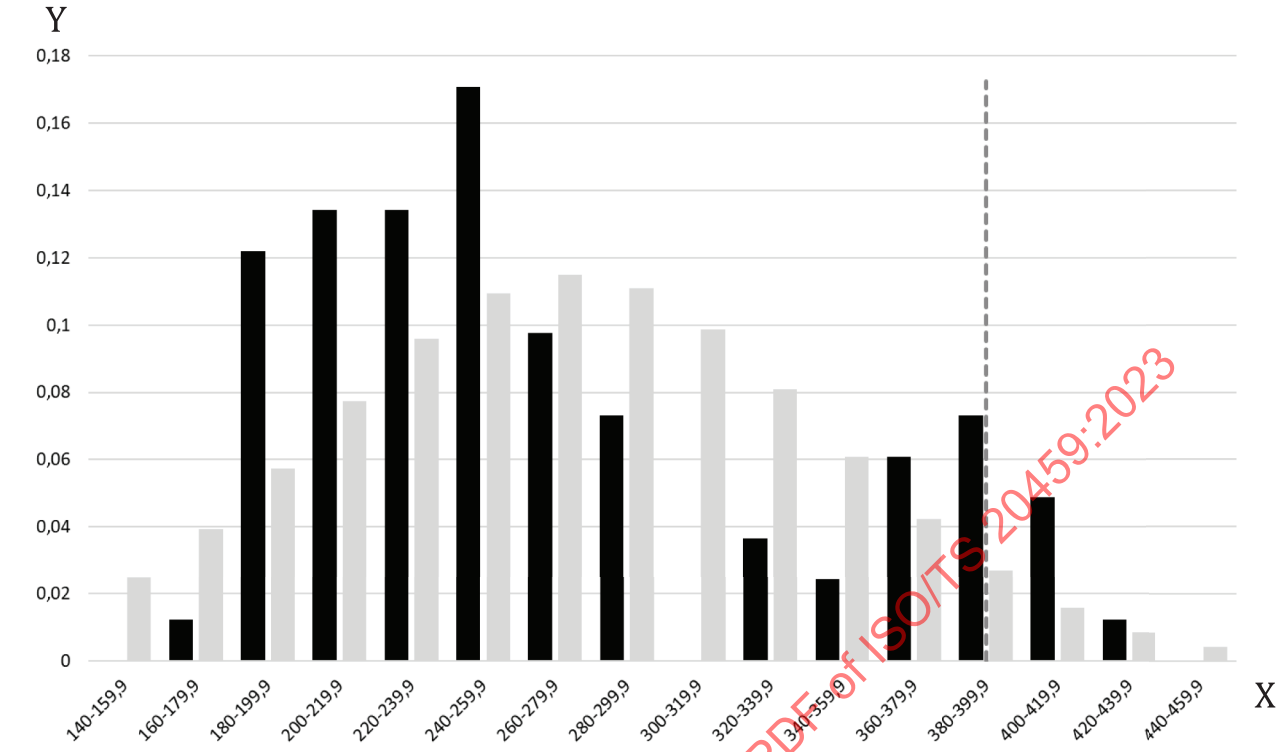

Key

X maximum tibia BM out of four measured [Nm]

Y normalized frequency (-)

aPLI test results

fitted normal distribution from aPLI test results

cross-check-value

Figure A.57 — "Cross-check-value" methodology results of combination for tibia

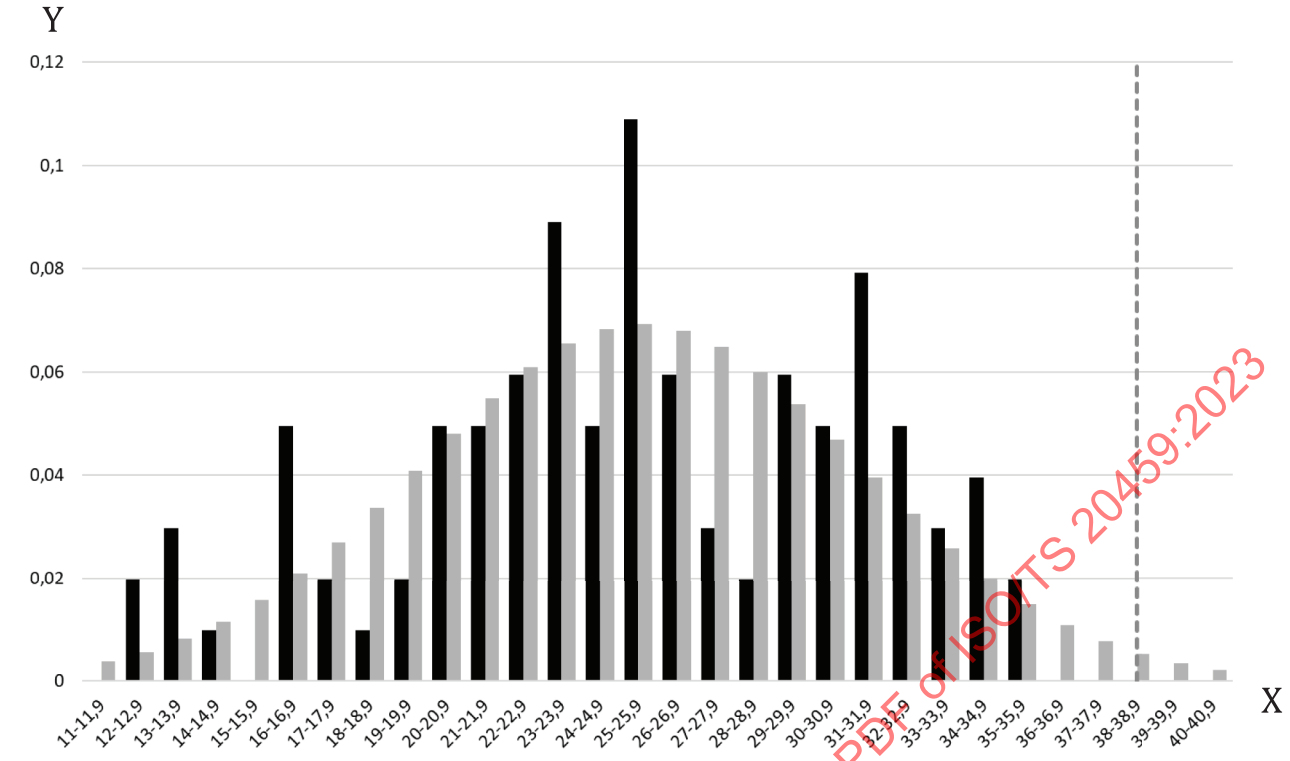

Key

X	maximum MCL elongation [mm]
Y	normalized frequency (-)
■	aPLI test results
■	fitted normal distribution from aPLI test results
⋮	cross-check-value

Figure A.58 — "Cross-check-value" methodology results of combination for MCL

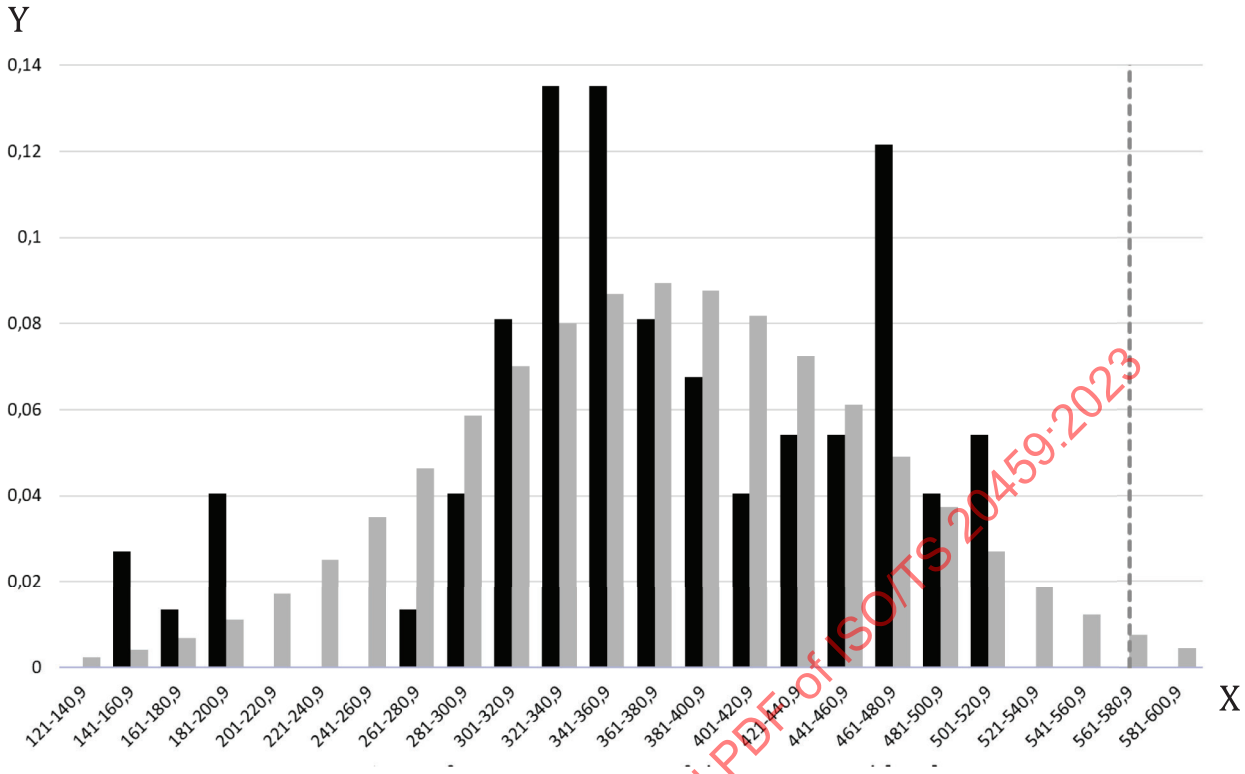

Key

X	maximum femur BM out of three measured [mm]
Y	normalized frequency (-)
■	aPLI test results
■	fitted normal distribution from aPLI test results
⋮	cross-check-value

Figure A.59 — "Cross-check-value" methodology results of combination for femur

Table A.31 — Evaluated injury occurrences for tibia, femur and MCL

	Cross-check value	Injury occurrence (accident data)	Injury risk from aPLI IPF-STP
Femur	571,5 Nm	1,3 %	>90 %
MCL	38,2 mm	1,3 %	>80 %
Tibia	384,7 Nm	5,2 %	<20 %

A.2.6.3.2.6 Discussion

It shall be taken into account that only preliminary IPF-STPs for the aPLI were available when Group B conducted this study. Furthermore, all studies dealt with the aPLI version SBL-A. Unfortunately, for the SBL-B version of the aPLI there are no sufficient test data available to update the study.

Nevertheless, the results led to the conclusion, that the root cause of such high differences between the accident occurrence and the injury risk level resulting from the aPLI IPF-STP needed to be investigated further.

A.2.6.4 Conclusion

The results of the validation of the aPLI IPFs-STP done by Group A demonstrated that the aPLI IPF-STP for the leg and the knee need to be adjusted due to the significant difference between the observation and the prediction (5,3 % and 2,4 % for the leg and the knee, respectively). No adjustment will be applied to the aPLI IPF-STP for the thigh.

The studies of Group B show high discrepancies between the "theoretical" injury risk based on the aPLI IPF-STP and the "real" injury risk, based on accident data to suffer lower limb injuries, which are addressed by the aPLI.

Consequently, both groups decided to analyse the cause of the discrepancy between the accident data and the prediction from the aPLI injury values. The methodology and the results of the adjustment of the aPLI IPFs-STP to accident data are summarised in Annex B.

Annex B
(informative)

Adjustment of IPFs for real-world relevance

B.1 Background

As stated in A.1.1, IPFs for the aPLI would require adjustment of IPFs to match field observations, if the load case specified by the STP does not represent real-world accidents. The IPFs for the FlexPLI were developed to predict injury probability to a pedestrian when the pedestrian is subjected to a car impact in a load case specified in the STP. In contrast, car-pedestrian impacts in real-world accidents involve a wide variety of different load cases. This may result in an inconsistency between the probability of injury predicted from the results of a subsystem test and the frequency of injury in real-world accidents. However, the real-world relevance of the IPFs for the FlexPLI were not validated against accident data. As the STP has been implemented in consumer information tests and regulatory tests, car safety measures to protect pedestrians are developed primarily based on such test results. If there is a large discrepancy between the predicted injury probability and actual frequency of injury, the car safety measures may not be sufficiently effective due to this bias.

The results of the validation of the real-world relevance of the aPLI IPFs-STP described in A.2.6 showed that a significant difference was seen between the number of injuries from the accident data and the number of injuries predicted by applying the aPLI injury values to the aPLI IPFs-STP specifically for the knee and the leg. Based on the results, adjustment of the IPFs to accident data was investigated. Due to the challenging nature of the work from essentially large variability in the parameters describing both the load case in the accident and human impact response and tolerance, two groups under the aPLI TG (Group A and B; see A.2.6.1) individually worked on the adjustment to the real-world data.

This annex describes presumed factors of reduced real-world relevance of the IPFs (B.2), adjustment of the IPFs by means of quantifying the influences of such factors using computational HBM impact simulations (theoretical adjustment, see B.3) and further adjustment of the IPFs, as needed, such that the predicted number of injuries matches the number of injuries from the accident data (empirical adjustment, see B.4).

B.2 Factors of reduced real-world relevance

B.2.1 General

Presumed factors responsible for the discrepancy of the observed and predicted number of injuries were investigated by each of the two groups. Group A started by evaluating representativeness of each of the conditions included in the STP, and focused on the influence of the anatomical structure and functions of the relevant human body regions. Group B investigated the effect of the lower limb muscles and the impact direction on the knee lateral bending and the MCL elongation during vehicle-to-pedestrian impacts.

B.2.2 Presumed factors (Group A)

The load case defined by the STP (References [1] and [2]) includes the impact speed, the pedestrian height and weight (as represented by the impactors), the impact angle and the posture of the lower limb. More than 70 % of all pedestrian lower limb injuries occur at the impact speed of 40 km/h and below[36]. The pedestrian height (175,1 cm) and the weight (76,5 kg) represented by the legforms are taken from the anthropometric data of a 50th percentile adult male (Reference [3]). The impact angle specified in the STP represents impact of a vehicle's front-end against the lateral aspect of the pedestrian's lower limb. According to the accident data, impacts delivered to the lower limb of a pedestrian in the

direction lateral to the pedestrian lower limb ±30° accounts for 74 % of accident cases[37]. Based on this evaluation of the representativeness of the load case against the real-world situation, these conditions were deemed representative of the accidents. In contrast, the posture of the lower limb with the knee fully extended and the entire lower limb perpendicular to the ground does not represent any phase of the gait cycle (Figure B.1). Because of this apparent discrepancy, it was decided to focus on the influence of the lower-limb posture.

Due to the anatomic structure of the knee (Figure B.2), the MCL is stretched only when the knee is fully extended, and is relaxed when the knee is flexed[38]. Due to the slack of the MCL with the knee flexed, and the angle of the entire lower limb relative to the ground, the MCL is less susceptible to knee bending, compared to the STP that represents no slack of the MCL with the lower limb perpendicular to the ground. The difference of the angle of the leg may result in different loading to the tibia as well.

Although the representation of the impact angle with the lateral impact used in the STP represents the majority of accidents, the loading to the lower limb may be influenced by the impact angle. Specifically, the MCL is attached to the medial side of the distal femur (femoral condyle) and the proximal tibia (tibial plateau), and the centre of rotation of the knee in lateral bending is the lateral side of the femoral condyle (Figure B.3); in the case of the valgus bending of the struck-side lower limb, the radius of rotation would be the largest in a pure lateral bending.

In addition to the influence of the lower-limb posture and the impact angle, the muscle tone may also be a factor. In the biomechanical testing from which biomechanical data were obtained and the human IPFs were developed, cadaveric specimens with no muscle tone were used. In contrast, the muscles around the knee are active while standing or walking[39] and the stiffness of the knee in lateral bending would be influenced, although the muscle forces would pose minimal influences on the loading to the bones with much stiffer material properties compared to the MCL.

Consequently, Group A quantitatively analysed the effects of the lower-limb posture, the impact angle and the muscle tone to adjust the aPLI IPFs-STP for the leg and the knee.

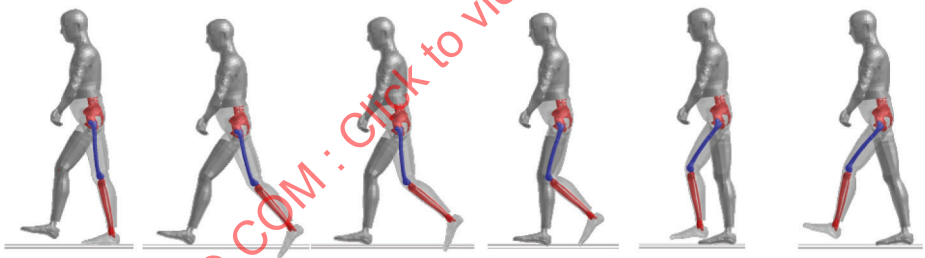

a) Six representative walking posture in a gait cycle

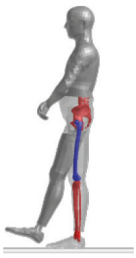

b) Lower-limb posture represented by the STP

Figure B.1 — Comparison of lower-limb posture between the gait cycle and the STP

a) Fully extended knee **b) Flexed knee**

Key

1 MCL tends to be stretched

2 MCL tends to be slack

Figure B.2 — Difference of MCL condition by the knee posture

Key

1 MCL stretch

2 centre of rotation

Figure B.3 — Centre of rotation in lateral bending

B.2.3 Presumed factors (Group B)

Presumed factors analysed by Group B were comparable with those of Group A which are described in B.2.2.

Group B focused on investigating the effect of the lower limb muscles and the impact angle on the knee valgus angle and MCL elongation based on computer simulation analysis to adjust the aPLI IPFs-STP for the knee theoretically.

B.3 Theoretical adjustment

B.3.1 General

Each of the two groups first aimed to quantify the influence of the presumed factors by means of computational pedestrian impact simulations using HBMs. Next, the aPLI IPFs-STP were adjusted by reflecting the results of the computational analysis and the adjusted IPFs were evaluated using the methodology described in A.2.6.2 for Group A and A.2.6.3 for Group B, respectively.

B.3.2 Analysis (Group A)

B.3.2.1 General

In this analysis, the influence of the lower-limb posture, the impact angle and the muscle tone were quantified by means of computational impact simulations using an HBM. The influence of the muscle tone was considered only for the knee (complete MCL failure), considering the magnitude of the muscle forces and the tolerance of bones in compression.

Impact simulations using an HBM were performed by varying the lower-limb posture and the impact angle to estimate the sensitivity of these factors. The weighted average of the maximum injury values (tibia BM and MCL elongation) were compared with those obtained from an impact simulation where the lower-limb posture and the impact angle comply with the STP to calculate the ratio of the weighted average of the maximum injury values to those with the lower-limb posture specified in the STP defined as a correction factor.

Next, the influence of the muscle tone around the knee joint was taken into consideration. The muscle tone appears to increase the valgus bending stiffness of the knee joint and thus reduces MCL elongation in car-pedestrian collisions. Based on this assumption, the increase of the knee valgus bending stiffness was estimated from the literature and a correction factor was determined for the influence of the muscle tone by the reciprocal of the stiffness increase ratio.

The correction factors were used to adjust the aPLI IPFs-STP, and the modified IPFs were validated against accident data using the methodology specified in A.2.6.2.1.

B.3.2.2 Impact simulation

B.3.2.2.1 Simulation model

The HBM-A, as defined in A.2.4.2.2, and a SCM which mimics a representative car in the GIDAS database were used in this analysis. A SCM as opposed to RCM was used to save computational time. The SCM was developed in several steps. First, GIDAS database was investigated to determine the representative car type. The same case selection criteria as those applied in B.1 was used to confirm that the most frequent type of car is a sedan (Table A.25). Second, the representative sedan shape was determined from Reference [35]. Figure B.4 shows the representative sedan shape of the mid-section in the longitudinal vertical plane. Third, a SCM that comprises the three discrete rigid components for BLE, BP and SP was developed to represent the sedan shape. These components translate in the opposite direction of car travel with specified non-linear spring characteristics, except for the BLE modelled using shell elements (Figure B.5). This modelling strategy was necessary because BLE tends to be subjected to a combined longitudinal and vertical force due to contact with the lower limb of a pedestrian in impacts against sedans. The geometric and stiffness characteristics of the SCM are described in Figure B.6 and Figure B.7 along with Table B.1, respectively. The SCM was validated by comparing the kinematics and the time histories of the thigh, leg and knee injury metrics from the HBM-A with the lower-limb posture representing that specified in the STP between the SCM and an RCM with a similar shape as described in Figure B.8 and Figure B.9, respectively.

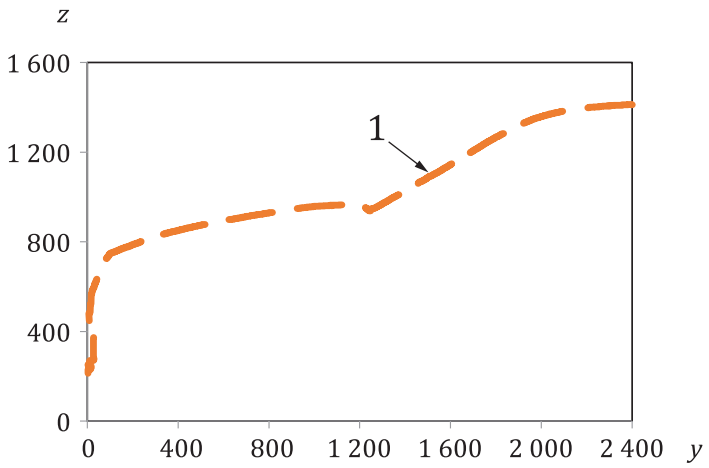

Key

y coordinate in car longitudinal direction [mm]

z coordinate in vertical direction [mm]

1 representative outer contour of the centre section of sedan[35]

NOTE 1 y=0 corresponds to the frontal end of BP.

NOTE 2 z=0 corresponds to the ground.

Figure B.4 — Representative car shape for sedan

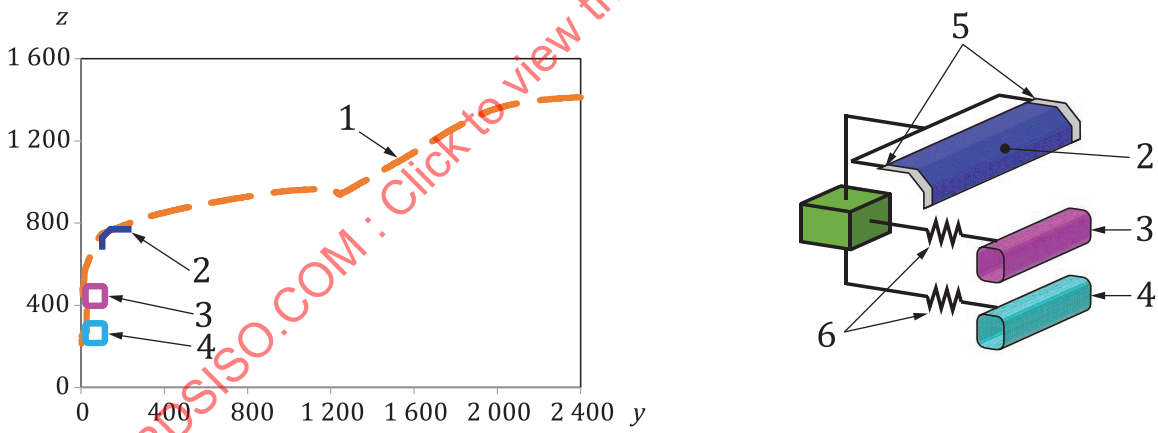

a) Comparison between outer contour of vehicle centre and SCM (side view) **b) Structure of the SCM (oblique view)**

Key

y coordinate in car longitudinal direction [mm]

z coordinate in vertical direction [mm]

1 representative outer contour of centre section of sedan[35]

2 BLE of SCM

3 BP of SCM

4 SP of SCM

5 rigidly constrained lateral edge of BLE of SCM

6 transrational joint and linear spring representing stiffness of corresponding vehicle part

NOTE 1 y=0 corresponds to the frontal end of BP.

NOTE 2 z=0 corresponds to the ground.

Figure B.5 — SCM with representative car shape for sedan with simple structures

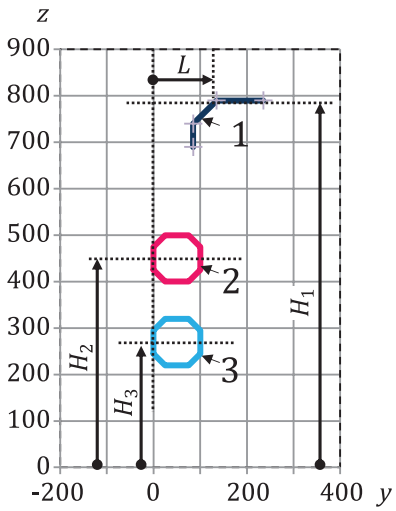

Key

y coordinate in car longitudinal direction [mm]
z coordinate in vertical direction [mm]
1 BLE
2 bumper
3 spoiler
H_1 BLE height: 790 [mm]
H_2 BP centre height: 450 [mm]
H_3 SP centre height: 270 [mm]
L bonnet lead: 135 [mm]

NOTE 1 y=0 corresponds to the frontal end of BP.

NOTE 2 z=0 corresponds to the ground.

Figure B.6 — Geometric characteristics of the SCM

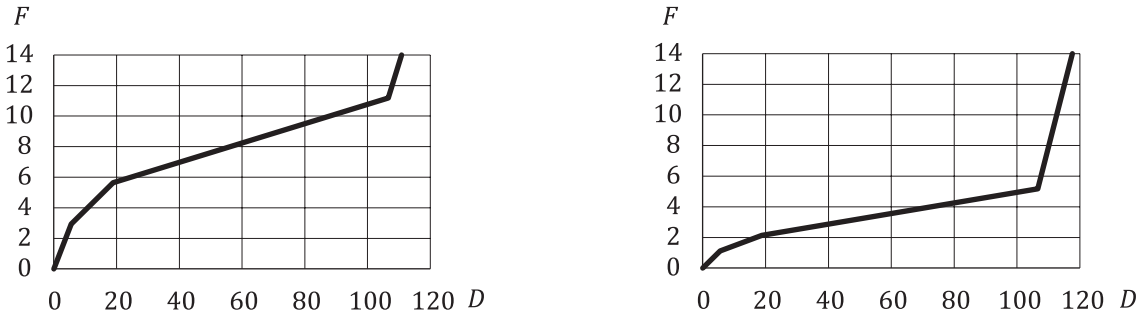

a) BP **b) SP**

Key

F force [kN]

D deflection [mm]

Figure B.7 — Stiffness characteristics of the SCM

Table B.1 — Stiffness characteristics of the SCM (tabulated data)

BP		SP	
D	**F**	**D**	**F**
0,0	0,0	0,0	0,0
5,6	2,9	5,6	1,1
18,9	5,6	18,8	2,1
106,6	11,2	106,6	5,2
150,0	40,0	150,0	40,0
Key			
D deflection [mm]			
F force [kN]			

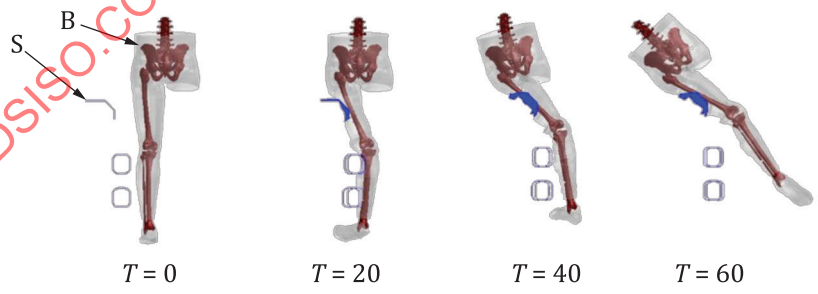

a) SCM and baseline HBM impact

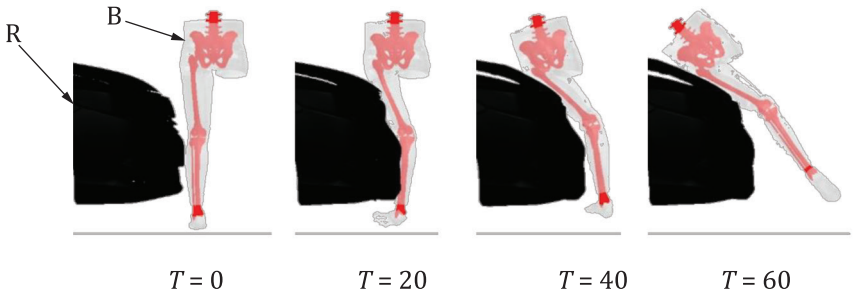

b) RCM and baseline HBM impact

Key

B baseline HBM
R RCM
S SCM
T time [ms]

NOTE Baseline HBM is invisible except for a lower limb on the struck side and hip.

Figure B.8 — Validation results of the SCM by the comparison of the baseline HBM responses in impact with the SCM and an RCM which has comparable shape with that of representative sedan (kinematics)

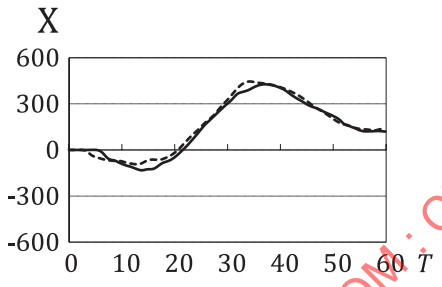

a) Femur-3 BM

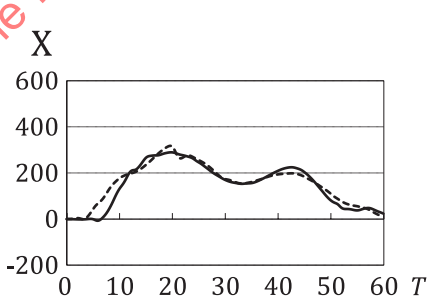

e) Tibia-1 BM

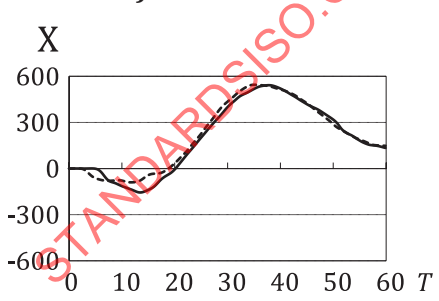

b) Femur-2 BM

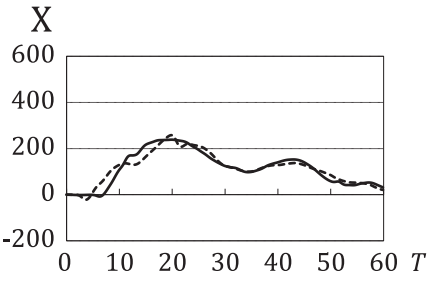

f) Tibia-2 BM

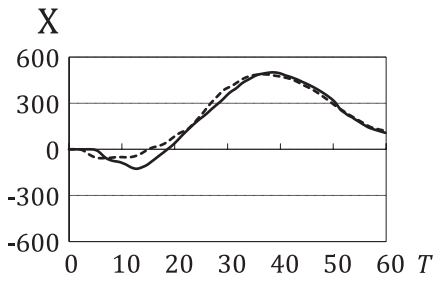

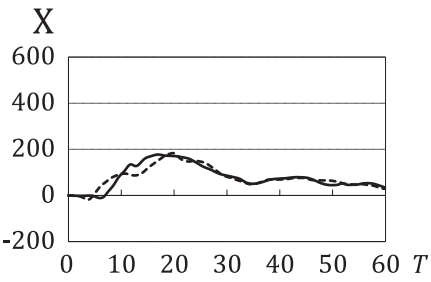

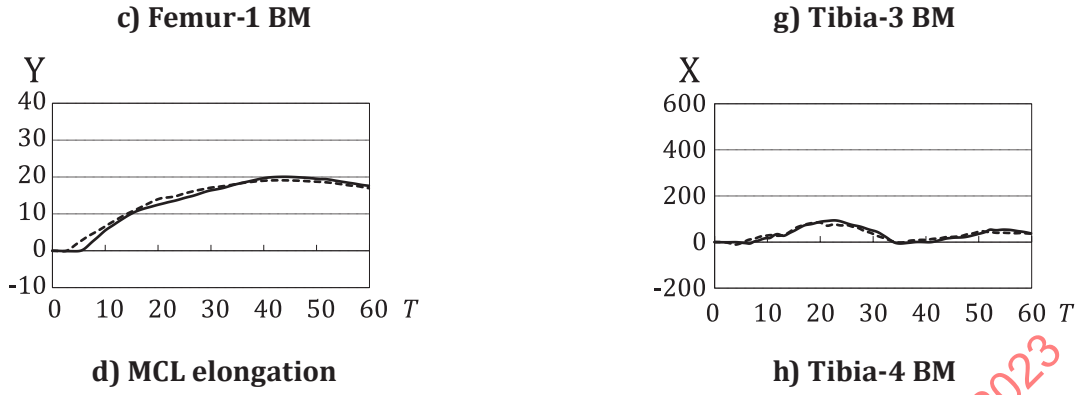

Key

X	BM [Nm]
Y	elongation [mm]
T	time [ms]
———	SCM
- - - - - - -	RCM

Figure B.9 — Validation results of the SCM by the comparison of the baseline HBM responses in impact with the SCM and an RCM which has comparable shape with that of representative sedan (time history plot of injury measures)

B.3.2.2.2 Model setup

The HBM-A defined in A.2.4.2.2 was used in this analysis. The baseline lower-limb posture of the HBM-A was set such that the line connecting the centre of the hip joint and the ankle joint of the struck-side lower limb is vertical to the ground, and the same line on the non-struck side is rotated 20° forward about the hip joint as shown in Figure B.10 (baseline posture). The lower-limb posture of the HBM-A was varied and six representative lower-limb postures (postures A through F) were defined to represent a gait cycle of a pedestrian as shown in Figure B.11. Due to the importance of the knee flexion angle that determines the initial slack of the MCL and thus significantly influences its maximum elongation, representative lower-limb postures were determined by dividing the range of the knee flexion angle of approximately 0° to 60° obtained from Reference [40] at approximately 20° increments as shown in Figure B.12. Only 40 % to 90 % of the gait cycle was simulated and other two postures at the knee flexion angle of 20° were assigned to posture F because of the similarity of the hip joint angle. The duration of each posture was determined by the middle points of the percent of the gait cycle to the adjacent postures, and the frequency of each of the six lower-limb postures was determined proportional to the duration as shown in Table B.2. The element elimination option of the HBM-A representing failure of the tissues were inactivated, except for the fibula, to predict maximum loads on the femur, tibia and MCL, while maintaining realistic loading conditions of the tibia for which injury metrics are set for the HBM-A.

Injury metrics for the knee (MCL elongation) and the leg (tibia BM) of the HBM-A were measured at the location illustrated in Figure A.45. The maximum values of the MCL elongation and the tibia BM were recorded and used to determine the theoretical correction factors.

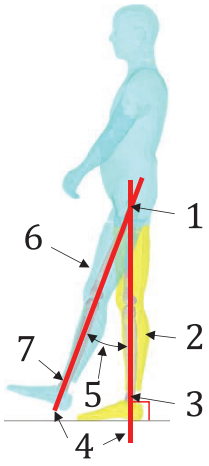

a) Struck-side view

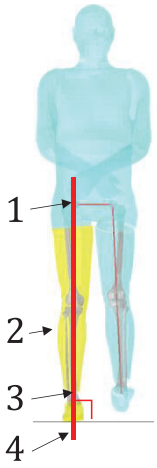

b) Back view

Key

1 hip-joint centre
2 struck side of vertical lower limb
3 ankle-joint centre
4 line connecting the centre of the hip joint and the ankle joint
5 20°
6 non-struck side of straight lower limb
7 ankle-joint centre

Figure B.10 — Baseline lower-limb posture of the HBM

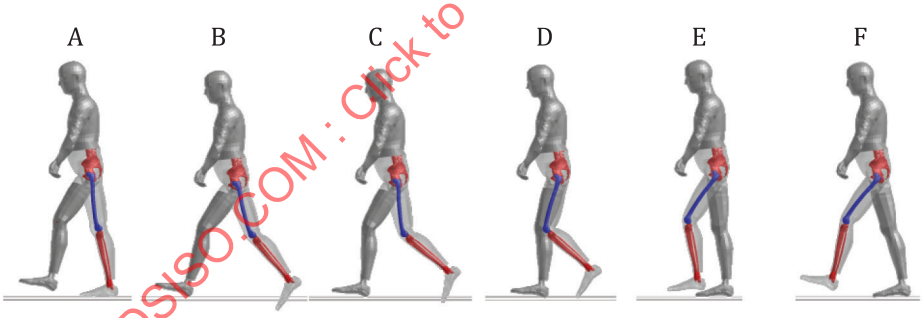

Key

A lower-limb posture at minimum knee flexion angle in one gait cycle
B, F lower-limb postures at one third of maximum knee flexion angle in one gait cycle
C, E lower-limb postures at two thirds of maximum knee flexion angle in one gait cycle
D lower-limb posture at maximum knee flexion angle in one gait cycle

Figure B.11 — Six representative walking postures in a gait cycle

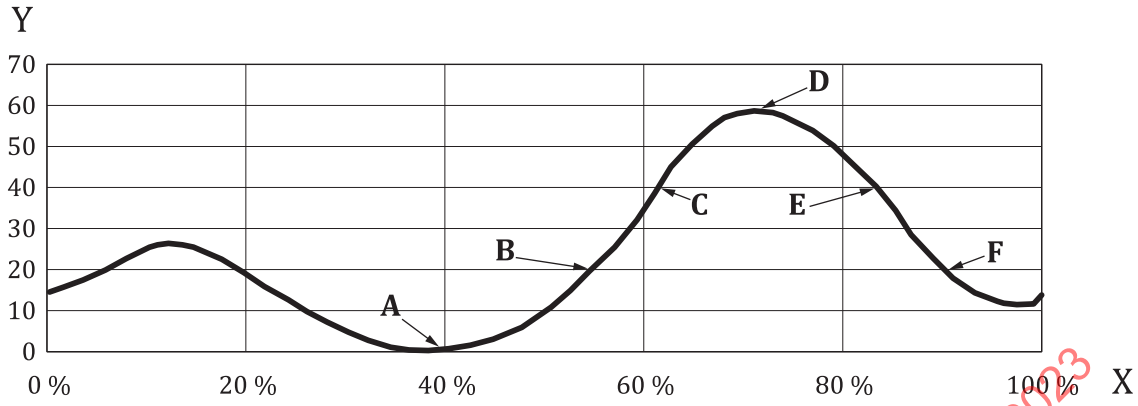

Key

X	percent of gait cycle
Y	knee flexion angle [°], and its polarity is defined in Figure B.13
A	lower-limb posture at minimum knee flexion angle in one gait cycle
B, F	lower-limb postures at one third of maximum knee flexion angle in one gait cycle
C, E	lower-limb postures at two thirds of maximum knee flexion angle in one gait cycle
D	lower-limb posture at maximum knee flexion angle in one gait cycle

Figure B.12 — Knee flexion angle of the six representative lower-limb postures of the HBM

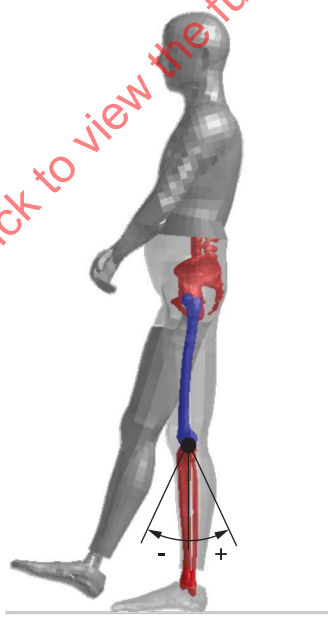

Figure B.13 — Polarity of the knee flexion angle

Table B.2 — Frequency of the six representative lower-limb postures in a gait cycle

Dimensions in percentages

ID of six representative lower-limb posture	Duration-based frequency
A	32,5
B	11,5
C	8,0
D	11,5

Table B.2 *(continued)*

ID of six representative lower-limb posture	Duration-based frequency
E	9,5
F	27,0

Table B.3 shows the impact simulation matrix for the baseline and other six postures of the HBM. The impact speed was set at 11,1 m/s for all postures. Since the baseline posture was used to represent the load case specified in the STP, only one impact simulation was performed in the lateral-to-medial impact direction defined as 0°. The GIDAS database classifies the impact angle at the 30° increment, and it showed that the accidents with the impact angle between ±30° accounts for approximately three fourths of all the accidents as shown in Table B.4. For this reason, the impact angle was varied between ±45° at the 15° increments. The mean of the maximum MCL elongation and the maximum tibia BM at the impact angle of 0° and ±30° were estimated by the weighted average of the simulation results. The average maximum MCL elongation and the maximum tibia BM at 0° was calculated from the weighted average of the simulation results at 0°, +15° and -15° with the weighting factor of 0,50, 0,25 and 0,25, respectively. The same procedure was also applied to estimate the mean of the maximum MCL elongation and the maximum tibia BM at ±30°.

Table B.3 — Computer simulation matrix for baseline and other six postures of the HBM

Simulation ID	Lower-limb posture	Impact angle
Baseline	STP	0°
Real-world	A through F	±45° at 15° increments
NOTE 1 Definition of lower-limb posture is shown in Table B.11.		
NOTE 2 Polarity of impact angle is shown in Figure B.14.		

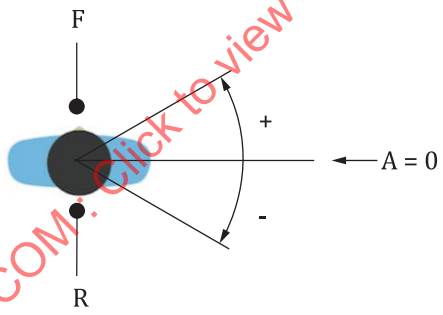

Key

A impact angle [°]
F frontal side of pedestrian
R rear side of pedestrian

Figure B.14 — Polarity of impact angle

Table B.4 — Frequency of the car impact angle from the GIDAS database

Impact angle [°]	Frequency [%]	
	Each	Subtotal
+90	7,8	-
+60	7,6	-
NOTE 1 For the polarity of impact angle, see Figure B.14.		
NOTE 2 Frequency data for 0°, +30°, +60°, -30°, -60° include frequency for impact directions symmetric with respect to anterior-posterior direction.		

Table B.4 *(continued)*

Impact angle [°]	Frequency [%]	
	Each	Subtotal
+30	12,3	
0	57,0	74,4
-30	5,1	
-60	1,4	-
-90	1,5	-

NOTE 1 For the polarity of impact angle, see Figure B.14.

NOTE 2 Frequency data for 0°, +30°, +60°, -30°, -60° include frequency for impact directions symmetric with respect to anterior-posterior direction.

B.3.2.2.3 Calculation of the weighted average of the injury values

For each of the six representative lower-limb postures illustrated in Figure B.12, the individual weighted average of the maximum MCL elongation and the maximum tibia BM for the impact angles of 0°, +30° and -30° were calculated using the weighting factors of 0,766, 0,165, 0,069, respectively, determined from the frequency of accidents shown in Table B.2 to calculate the values that represent the six lower-limb postures. The overall weighted average of the representative values was calculated with the weighting factor assigned to each of the six lower-limb postures based on the proportion of the duration represented by the posture in one gait cycle. The factors were determined as 0,325, 0,115, 0,080, 0,115, 0,095 and 0,270 for the lower-limb postures A through F, respectively, from the duration between the middle points to the two adjacent postures. The correction factor of the MCL elongation and the tibia BM were calculated by dividing the overall weighted average of the maximum MCL elongation and the maximum tibia BM by the maximum MCL elongation and the maximum tibia BM from the impact simulation in the baseline posture and impact angle.

B.3.2.2.4 Simulation results

Figure B.15 shows the individual weighted average of the maximum MCL elongation and the maximum tibia BM for each of the six lower-limb postures. Apparently, all walking postures in the real world (A through F) lead to smaller maximum values compared to the baseline posture with the struck-side lower limb in the upright position as specified in the STP. The fact that any of the individual weighted averages of the maximum MCL elongation and the maximum tibia BM for different lower-limb postures in a gait cycle is smaller than the value predicted by the baseline model suggests that the baseline posture specified in the STP is not a representative of various lower-limb postures in a gait cycle.

As shown in Table B.5 and Table B.6, the overall weighted average of the maximum MCL elongation and the maximum tibia BM for all lower-limb postures was found to be smaller by 29 % and 8 % than that of the baseline posture, respectively. This resulted in the correction factor of 0,72 and 0,90 for the MCL elongation and the tibia BM, respectively. However, it was decided not to apply the correction factor for the tibia BM because the influence was less than 10 %, which corresponds to only 0,5 % of the difference between the field observation and the prediction relative to the number of pedestrians in the mother group (A.2.6.2.2.3) and thus modification to the IPF is not justified.

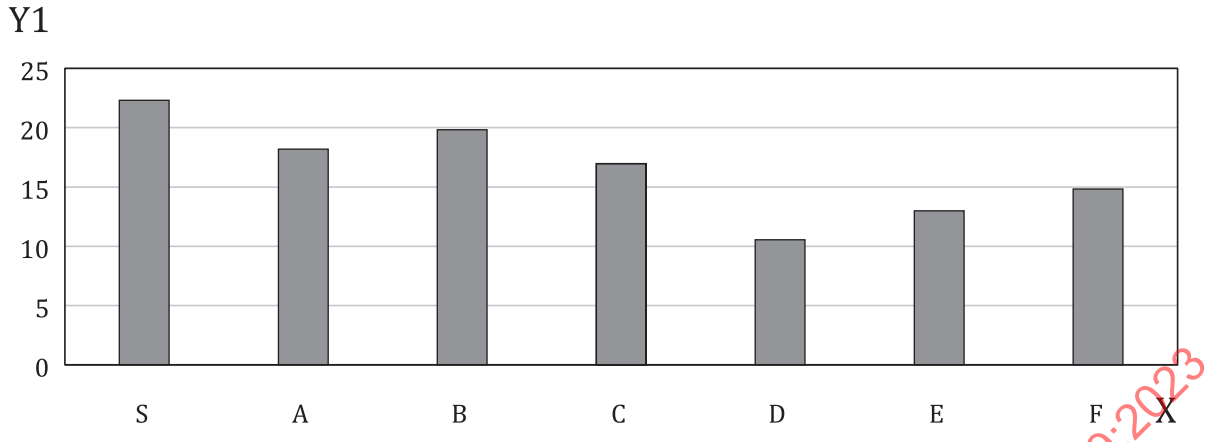

a) Weighted average of the maximum MCL elongation

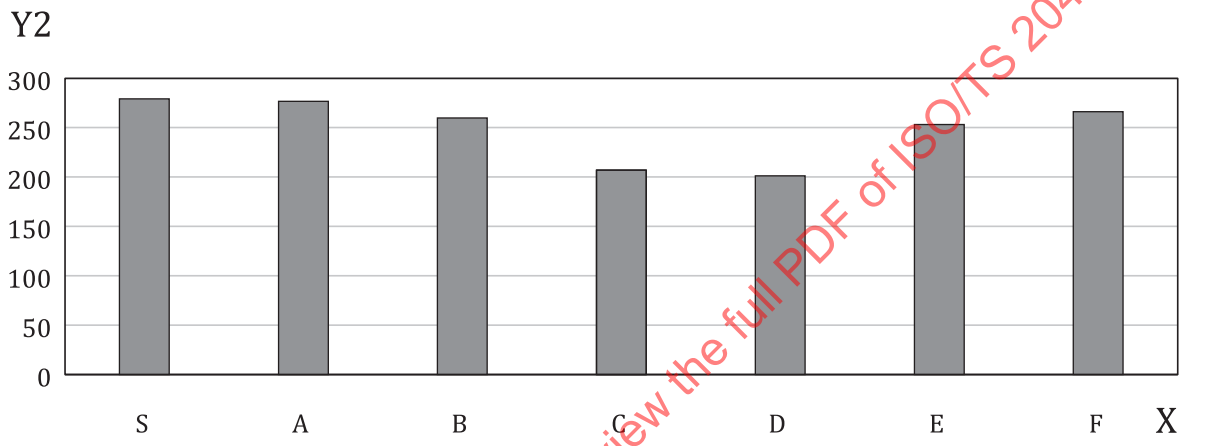

b) Weighted average of the maximum tibia BM

Key

X	ID of lower-limb posture
Y1	weighted average of maximum MCL elongation [mm]
Y2	weighted average of maximum tibia BM [mm]
A through F	representative of lower-limb posture in one gait cycle (see Figure B.11)
S	lower-limb posture in STP

Figure B.15 — Weighted average of the maximum MCL elongation and tibia BM by lower-limb posture

Table B.5 — Overall weighted mean of the maximum MCL elongation and correction factor

Lower-limb posture	MCL elongation [mm]	Correction factor
Baseline	22,3	-
Real-world (A, B, C, D, E, F)	16,0 (overall weighted mean)	0,72

Table B.6 — Overall weighted mean of the maximum tibia BM and correction factor

Lower-limb posture	Tibia BM [Nm]	Correction factor
Baseline	297	-

Table B.6 *(continued)*

Lower-limb posture	Tibia BM [Nm]	Correction factor
Real world (A, B, C, D, E, F)	255 (overall weighted mean)	0,92

B.3.2.3 Influence of the muscle tone

In addition to the influence of lower-limb posture on MCL elongation quantified by means of computer simulations using an HBM (B.3.2.2), the influence of the muscle tone around the knee joint was estimated from the literature.

In Reference [41] the contribution of the musculature around the knee joint was estimated by means of a volunteer test using 10 human subjects and a biomechanical model adjusted for each of the human subjects. Depending on the magnitude of the muscle contribution to pure varus and valgus moments, they grouped the 10 subjects into two. The first group consisting of 8 out of 10 subjects showed that the total muscle contribution to the pure valgus moment was (10 ± 6,3) %, while the second group, consisting of the remaining 2 subjects, showed a 53 % contribution. The results of the group involving the majority of the subjects was used and the correction factor was determined as 0,90 from the reciprocal of the contribution to the valgus moment.

B.3.2.4 Modified IPF

Figure B.16 shows the IPF for MCL elongation of the aPLI theoretically adjusted by the two correction factors calculated in B.3.2.2.4 (0,72) and B.3.2.3 (0,90).

The adjustment needs to be applied to the IPF for human because the adjustment takes differences in walking posture and muscle tone into consideration, both of which are related to human characteristics, not those of the aPLI. However, the TFs that convert injury metrics for human to those of the aPLI are linear functions with zero intercept, the same results are obtained when injury metrics for the aPLI are adjusted. The adjusted IPF of MCL elongation for the aPLI was therefore determined by applying the two correction factors to the aPLI MCL elongation. The adjusted IPF for the aPLI is therefore expressed by Formula (B.1):

$$\boldsymbol{P_{adj} = F\left(G\left(I_{aPLI}\right)\times 0{,}72\times 0{,}90\right)} \tag{B.1}$$

where

P_{adj} is the adjusted injury probability for the MCL;

F is the function that specify the IPF of the MCL for human;

G is the transfer function that converts the MCL elongation of the aPLI to the knee valgus angle of human;

I_{aPLI} is the injury metric of the MCL (MCL elongation) measured by the aPLI.

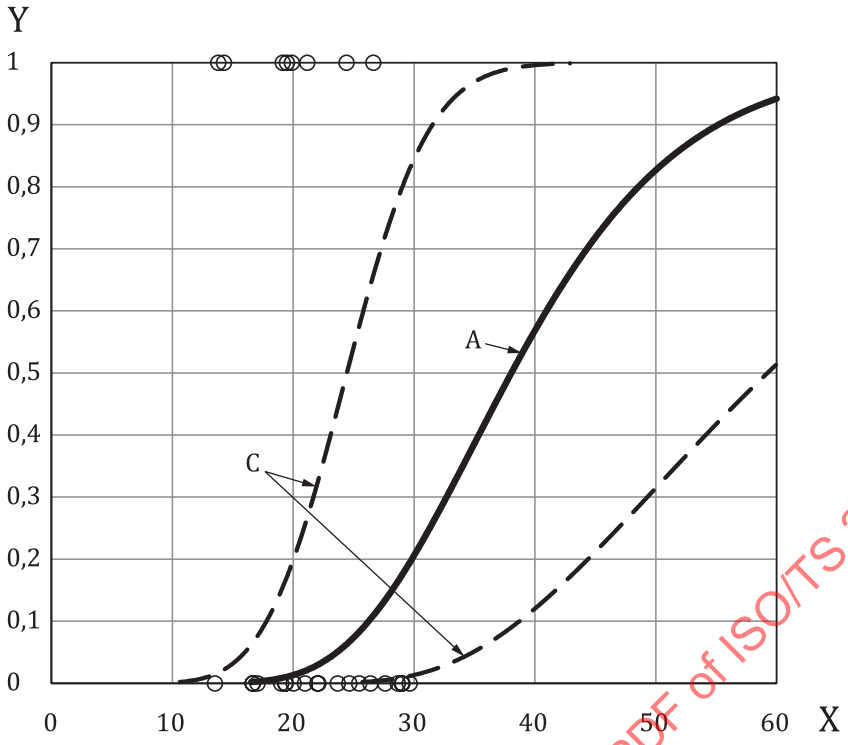

Key

X	aPLI MCL elongation [mm]
Y	injury probability for the MCL
A	theoretically adjusted aPLI IPF for MCL complete rupture
C	95 % confidence interval
◯	observed data

Figure B.16 — Theoretically adjusted aPLI IPF for the MCL

B.3.2.5 Validation of modified IPF

The theoretically adjusted aPLI IPF for the knee determined in B.3.2.4 was validated in accordance with A.2.6.2.1. As a result, as shown in Figure B.17, the morbidity estimated using the modified IPF is much closer to the accident data compared to that before the adjustment. In addition, the estimated number of injuries for the knee was significantly reduced from 39 to 2, becoming closer to the accident data of 11. Based on the results, it was decided to conclude the adjustment of the aPLI IPF for the knee.

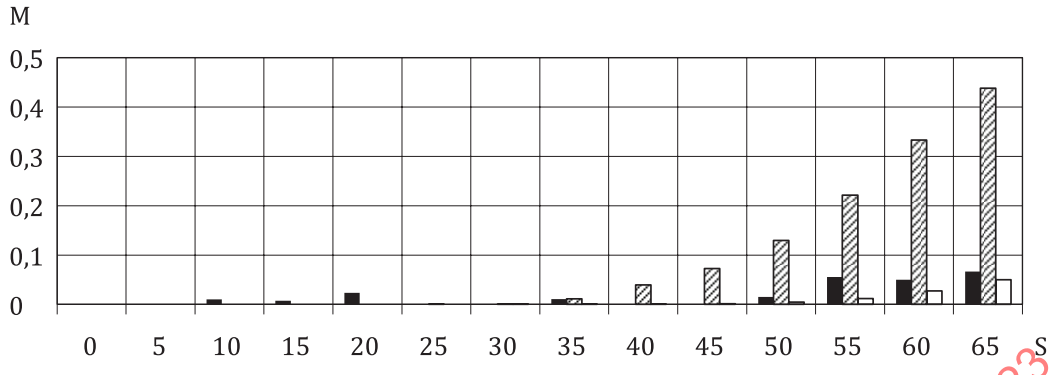

Key

■	accident data
▨	predicted by aPLI IPF in the load case of STP
□	predicted by theoretically adjusted aPLI IPF
M	morbidity (-)
S	impact speed [km/h]

Figure B.17 — Comparison of morbidity for the knee between the aPLI IPF-STP, theoretically-adjusted aPLI IPF and accident data

B.3.3 Analysis (Group B)

B.3.3.1 Effect of the lower limb muscles

The biomechanical data used in the study was adapted from peer-reviewed published literature. The pedestrian human body model HBM-C (see A.2.4.2.2) was adjusted by adding all important muscles (1D elements) from the pelvis to the toes as described in previous studies[42][43] and was positioned in the posture described in A.2.4.3.2. To check whether the addition of muscles causes any anomalies while they are in a passive state, an HBM with zero activation (passive muscles) was simulated and compared with the published experimental results for three types of representative vehicles[44]. For the HBM kinematics and contact force data, a good agreement between the simulation results and experimental data[44] was observed. Later, muscle activation levels were identified from the literature corresponding to the equivalent phase of the gait cycle[45][46]. The muscles were individually activated to a fixed level and the activation remained constant throughout the simulation. For some muscles, activation levels were not available. Such muscles were activated to a very low level (0,05 level). The contact between both legs was activated to simulate real-world conditions.

To investigate the effect of active muscles, all simulations were performed using one HBM without muscles and one active model. Four types of generic vehicle (GV) models[35] were chosen. These models represent a family car (FCR), a multi-purpose vehicle (MPV), a roadster (RDS) and a sports utility vehicle (SUV). Revision 2.1 from 07th August 2019 of the GV models was used. The GVs impacted the standing HBM laterally with a speed of 40 km/h. For all simulations, the MCL elongation and the knee valgus angle of the struck-side leg were measured.

A comparison of the MCL elongation as well as the knee valgus angle of both simulated HBMs for all four vehicle categories are shown in Figure B.18 and Figure B.19, respectively. In every case, the MCL elongation as well as the knee valgus angle were reduced in the active model compared to the model without muscles. The MCL elongation as well as the knee valgus angle were reduced around 10 % on average (MCL: 9 %, Knee valgus angle: 11 %).

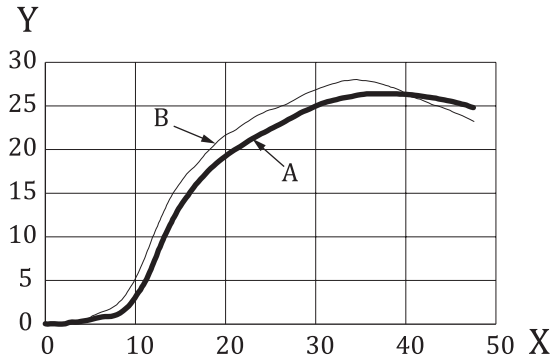

a) FCR

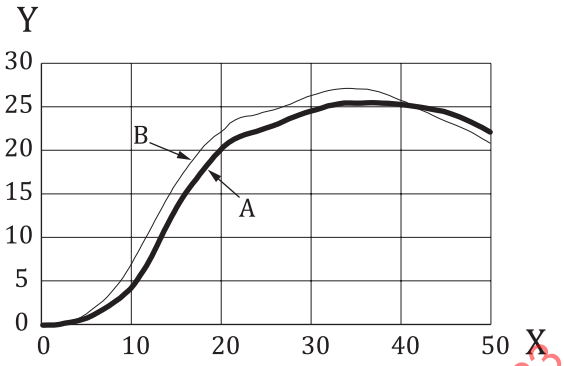

b) MPV

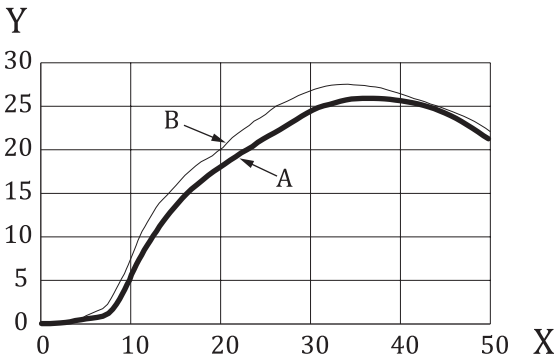

c) RDS

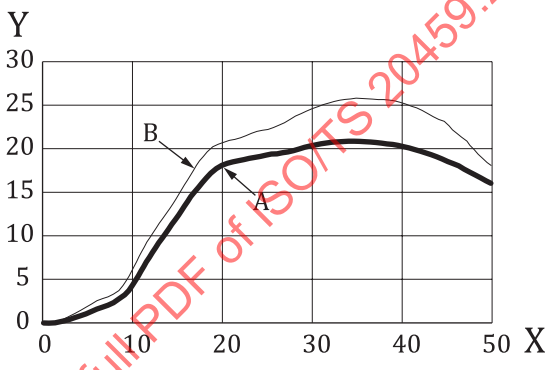

d) SUV

Key

X time [ms]
Y MCL elongation [mm]
A muscle: activated
B muscle: non-activated

Figure B.18 — MCL elongations for different GVs

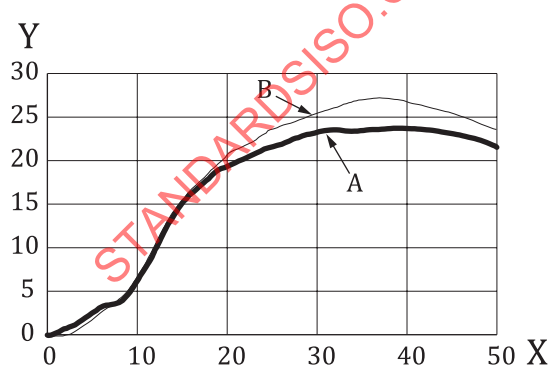

a) FCR

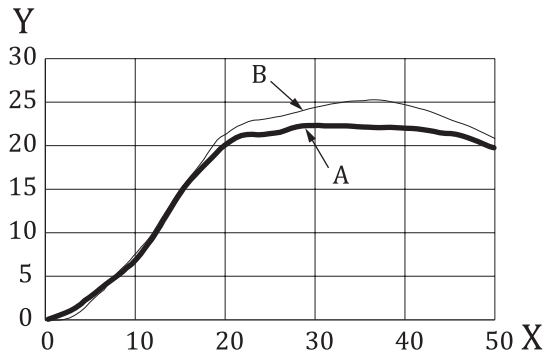

b) MPV

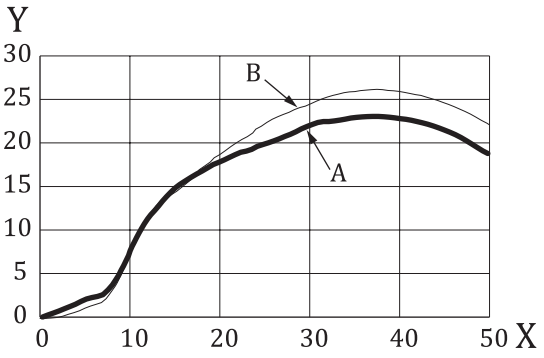

c) RDS

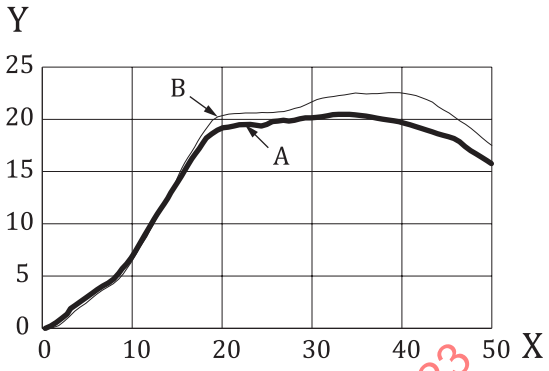

d) SUV

Key

X time [ms]

Y knee valgus angle [°]

A muscle: activated

B muscle: non-activated

Figure B.19 — Knee valgus angles for different GVs

B.3.3.2 Influence of pedestrian impact direction

Furthermore, Group B investigated whether the orientation of the pedestrian at the time of vehicle impact influences the knee valgus angle and MCL elongation. First and foremost, an analysis of GIDAS data was performed to clarify the orientation of the pedestrian that occurred the most at the time of impact with a vehicle. The dataset is from December 2020. Only reconstructed cases and accident years from 2000 and later were analysed including the following criteria:

— forward-moving passenger cars in their first collision with a pedestrian;

— only passenger cars with a frontal collision;

— pedestrian impact to vehicle was the first impact for the pedestrian;

— no lying/sitting or overrun pedestrians;

— no impacts of pedestrians to the side of the passenger cars;

— only pedestrians without sporting equipment (e.g. skateboard);

— only passenger cars included with known information on vehicle width and lateral coordinate for first contact point of the pedestrian.

The final dataset contains 1 655 passenger cars in collisions with a pedestrian. A passenger car impacts the pedestrian with the highest shares being lateral (65,4 %) as shown in Table B.7.

Table B.7 — Pedestrian's impact location distribution in frontal collisions with passenger cars (GIDAS)

Impact angle	Frequency
-90° ± 15°	1,8 %
-60° ± 15°	1,3 %
-30° ± 15°	6,1 %
0° ± 15°	65,4 %

Table B.7 *(continued)*

Impact angle	Frequency
30° ± 15°	13,1 %
60° ± 15°	5,6 %
90° ± 15°	6,6 %

After analysing the GIDAS database, the HBM simulations were performed with the same GV models used in the study of active muscles. The pedestrian human body model HBM-C as described in A.2.4.2.2 was positioned as described above in A.2.4.3.2. Location of the pedestrian knee centre with respect to the vehicle centre line remained constant while the orientation of the HBM was changed in the range of -90° to +90° with a step size of 15° (see Figure B.20). The straight left leg was defined as the struck-side leg. The GVs impacted the standing HBM with a speed of 40 km/h. The validity of the HBM for anterior impact directions (around 90°) is not certain due to a lack of literature data. However, the results are very plausible.

To receive one correction factor for the MCL elongation representing the average field situation, the average MCL elongation for each GIDAS impact direction (GIDAS angle 0°, 30°, 60°, …) including a tolerance of ±15° impact angle was calculated using Formula (B.2):

$$M_{\text{ave. GIDAS direction}} = \frac{M_{\text{GIDAS angle,}-15^\circ} + M_{\text{GIDAS angle}} + M_{\text{GIDAS angle,}+15^\circ}}{3} \quad \text{(B.2)}$$

where

$M_{\text{ave. GIDAS direction}}$ is the average MCL elongation for each GIDAS impact direction;

$M_{\text{GIDAS angle}}$ is the MCL elongation for a GIDAS impact direction of the specified angle;

$M_{\text{GIDAS angle, -15°}}$ is the MCL elongation for a GIDAS impact direction with a -15° angle;

$M_{\text{GIDAS angle, 15°}}$ is the MCL elongation for a GIDAS impact direction with a 15° angle.

Remark: Taking into account the symmetry, the average MCL elongation at -90° was calculated from the average of the simulation results at -90° and 2 × (-75°) (every value weighted by one third). The same procedure was applied to the average of the simulation result at 90° (90° + 2 × 75°).

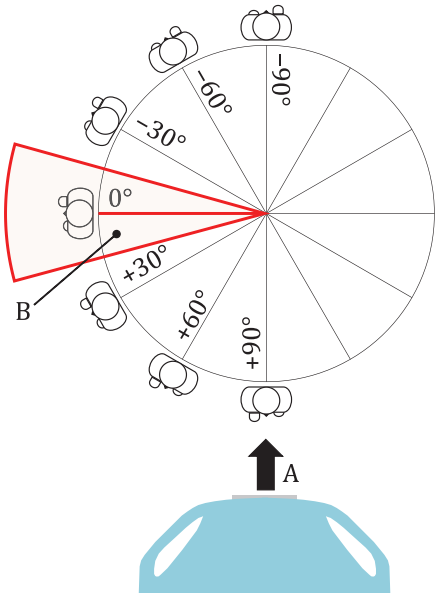

Key

A vehicle impact direction

B 15° step

Figure B.20 — HBM impact location constellation for vehicle – pedestrian impact

Next, a weighted average MCL elongation of all GIDAS impact directions was calculated. The weighting was performed according to the determined GIDAS distribution as shown in Table B.7.

A comparison of the MCL elongation as well as the knee valgus angle of all simulations in the various impact directions are shown in Figure B.21 and Figure B.22, respectively. It can be observed that for all types of vehicles, the MCL elongation and knee valgus angle were maximum for the impact angle range between 0° to 15°. Furthermore, the impact direction shows a high influence on the MCL elongation and knee valgus angle. Related to the impact orientation of 0°, the MCL elongation is reduced by an average of around 16 %, whereas the knee valgus angle reaches a reduction of 23 % on average. For the average value, all four vehicles were weighted equally.

Even though there was a low frequency of accidents with an impact angle of less than -30° or more than 30°, these impact angles have a significant influence on the average reduction of MCL elongation and knee valgus angle of the knee, because of very low values for these cases. It therefore makes sense to take these impact angles into account when adjusting the IPFs for real-world relevance.